LUND UNIVERSITY

Aerosol Metal Nanoparticles and their Role in Particle-Assisted Growth of III–V Nanowires

Hallberg, Robert

2018

Document Version:
Publisher's PDF, also known as Version of record

Link to publication

Citation for published version (APA):
Hallberg, R. (2018). *Aerosol Metal Nanoparticles and their Role in Particle-Assisted Growth of III–V Nanowires.*
[Doctoral Thesis (compilation), Faculty of Engineering, LTH]. Department of Physics, Lund University.

Total number of authors:
1

Aerosol Metal Nanoparticles and their Role in Particle-Assisted Growth of III–V Nanowires

ROBERT HALLBERG

DIVISION OF SOLID STATE PHYSICS | FACULTY OF ENGINEERING | LUND UNIVERSITY

Aerosol Metal Nanoparticles and their Role in Particle-Assisted Growth of III–V Nanowires

Aerosol Metal Nanoparticles and their Role in Particle-Assisted Growth of III–V Nanowires

Robert Hallberg

LUND
UNIVERSITY

DOCTORAL DISSERTATION
by due permission of the Faculty of Engineering, Lund University, Sweden.
To be defended at Rydbergssalen Sölvegatan 14, Lund,
on 19th October 2018 at 13:15.

Faculty opponent
Professor Sonia Conesa-Boj
Department Quantum Nanoscience, TU-Delft

Organization LUND UNIVERSITY	Document name Doctoral Dissertation
	Date of issue
Author Robert Hallberg	Sponsoring organization

Title: Aerosol Metal Nanoparticles and their Role in Particle-Assisted Growth of III–V Nanowires

Semiconductor nanowires have properties that make them potentially useful for applications in future electronic, photovoltaic, and optoelectronic devices. A powerful nanowire fabrication technique is the use of a nanoparticle as a preferential nucleation site, from which a nanowire grows. There has been significant progress in nanowire growth assisted by Au nanoparticles over the past 20 years. However, the high cost of gold and its incompatibility with silicon are obstacles to the industrial production of III–V nanowires. Therefore, significant efforts have been devoted to developing alternatives to Au-seeded nanowire growth. Although numerous metals and alloys are available, the development of alternatives to Au has been slow. The metal nanoparticles must have a high material quality and narrow size distribution, and their concentration must be controlled to enable precise experiments, and, in the future, high yields of identical devices.

In the work described in this thesis, a spark discharge generator was used to synthesize and characterize a wide range of metal nanoparticles: Ag, Au, Bi, Co, Pb, Pd, Pt, Rh, and Sn, as well as three alloys: $Ag_{25}Au_{75}$, AgAu, and $Ag_{75}Au_{25}$. The nanoparticles were formed as an aerosol in an inert carrier gas of N_2, and H_2 was added to prevent the oxidation of base metals such as Bi, Co, and Sn. The nanoparticles were then either deposited on III–V substrates for nanowire growth using metal organic chemical vapor deposition, or used directly for gas-phase nanowire growth in an Aerotaxy reactor. The nanoparticle melting temperature is governed by its composition, primarily controlled by the choice of initial metal and the concentration of the group III material during nanowire growth. The nanoparticle composition was investigated after growth using transmission electron microscopy. For Pd-seeded GaAs or InAs a high group III content was found to be correlated with straight vertical nanowires, in contrast to kinked curly nanowires. Nearly identical InAs nanowires could be grown from In-rich Au and Pd nanoparticles, and the transition to curly nanowires could be triggered by reducing the In concentration. Initiating growth in a stable In-rich regime might provide a means of using other seed metals, which could reduce the cost, may be compatible with Si, and potentially add new benefits of the added seed metal. For example, the growth of GaAs nanowires by Aerotaxy from Au and AgAu nanoparticles is simple, but when pure Ag nanoparticles were used the nanowires developed kinks at an early stage of growth, possibly due to the higher melting point.

Key words: aerosol, III–V semiconductor, nanowire, MOCVD, Aerotaxy, TEM

Classification system and/or index terms (if any)

| Supplementary bibliographical information | Language English |
| ISSN and key title | ISBN 978-91-7753-842-4 |

| Recipient's notes | Number of pages: 118 | Price |
| | Security classification | |

Signature _(signature)_   Date _423: /2; /32_

Aerosol Metal Nanoparticles and their Role in Particle-Assisted Growth of III–V Nanowires

Robert Hallberg

LUND
UNIVERSITY

Abstract

Semiconductor nanowires have properties that make them potentially useful for applications in future electronic, photovoltaic, and optoelectronic devices. A powerful nanowire fabrication technique is the use of a nanoparticle as a preferential nucleation site, from which a nanowire grows. There has been significant progress in nanowire growth assisted by Au nanoparticles over the past 20 years. However, the high cost of gold and its incompatibility with silicon are obstacles to the industrial production of III–V nanowires. Therefore, significant efforts have been devoted to developing alternatives to Au-seeded nanowire growth. Although numerous metals and alloys are available, the development of alternatives to Au has been slow. The metal nanoparticles must have a high material quality and narrow size distribution, and their concentration must be controlled to enable precise experiments, and, in the future, high yields of identical devices.

In the work described in this thesis, a spark discharge generator was used to synthesize and characterize a wide range of metal nanoparticles: Ag, Au, Bi, Co, Pb, Pd, Pt, Rh, and Sn, as well as three alloys: $Ag_{25}Au_{75}$, AgAu, and $Ag_{75}Au_{25}$. The nanoparticles were formed as an aerosol in an inert carrier gas of N_2, and H_2 was added to prevent the oxidation of base metals such as Bi, Co, and Sn. The nanoparticles were then either deposited on III–V substrates for nanowire growth using metal organic chemical vapor deposition, or used directly for gas-phase nanowire growth in an Aerotaxy reactor. The nanoparticle melting temperature is governed by its composition, primarily controlled by the choice of initial metal and the concentration of the group III material during nanowire growth. The nanoparticle composition was investigated after growth using transmission electron microscopy. For Pd-seeded GaAs or InAs a high group III content was found to be correlated with straight vertical nanowires, in contrast to kinked curly nanowires. Nearly identical InAs nanowires could be grown from In-rich Au and Pd nanoparticles, and the transition to curly nanowires could be triggered by reducing the In concentration. Initiating growth in a stable In-rich regime might provide a means of using other seed metals, which could reduce the cost, enable Si compatibility, and potentially add new benefits of the added seed metal. For example, the growth of GaAs nanowires by Aerotaxy from Au and AgAu nanoparticles is simple, but when pure Ag nanoparticles were used the nanowires developed kinks at an early stage of growth, possibly due to the higher melting point.

Populärvetenskaplig sammanfattning

Nanotrådar är små strukturer med stor potential, som man hoppas kan revolutionera komponenter som finns i våra datorer, lysdioder och solceller. Till exempel, arbetar ett spin-off företag från Lunds Universitet "Sol Voltaics" på kostnadseffektiva solceller baserade på nanotrådar som gentemot konventionella solceller kan öka effektiviteten med 50 %. Det vanligaste sättet att tillverka nanotrådar är genom att växa dem från guldnanopartiklar. Guld är dock ett särskilt olämpligt material när det integreras med kiselbaserad elektronik då det förstör de elektriska egenskaperna hos kislet. För att underlätta en kommersiell uppskalning av nanotrådsbaserade komponenter är det därför starkt motiverat att ta fram alternativ till guld. För att uppnå detta, har jag, vilket beskrivs i den här avhandlingen, utvecklat framställningen av nanopartiklar, speciellt för oädla metaller som lätt oxiderar. Nanopartiklarna har sedan använts för att studera hur nanopartikelns komposition påverkar faktorer som växthastighet, växtriktning och form hos nanotråden.

Nanopartiklar

Nanopartiklar finns överallt i vår omgivning men de är för små att se med blotta ögat. Oftast då man pratar om nanopartiklar syftar man till olika strukturer med en diameter från en nanometer (10^{-9} meter) upp till tusen nanometer. Nanopartiklar kan ha olika form, och inkluderar även avlånga fibrer likt de nanotrådar som skapas i denna avhandling. På grund av dess låg vikt kan nanopartiklar sväva i luften och blir enkelt luftburna. En gas med luftburna partiklar kallas för en aerosol och produceras dagligen i naturen från exempelvis skogar, öken, hav och vulkaner. Aerosoler reflekterar tillbaka en del av solens ljus, vilket bidrar till att kyla ner jorden. Dessutom är aerosoler nödvändiga för att skapa moln och regn, som bildas då vattenånga kondenserar på partiklarna. Utöver naturliga aerosoler finns det även människoskapade aerosoler som skapas oavsiktligt då vi exempelvis lagar mat, tänder ljus, kör bil eller bara genom att röra oss.

Utöver oavsiktligt genererade aerosoler finns det även avsiktligt genererade aerosoler, så kallade designade nanopartiklar. Designade nanopartiklar har skräddarsydda egenskaper för olika applikationer eller produkter. Vilka egenskaper de har bestäms till stor del utav dess storlek, kemiska sammansättning och kristallstruktur. Många typer av material är kristallina, vilket betyder att de består av atomer som är positionerade i ett väldefinierat mönster.

I Figur 1a) visas en 3D modell av en guldpartikel som består av cirka 30 000 atomer. Kristaller formar vanligtvis facetter, som är kristallografiska plan av atomer ordnade i ett specifikt mönster. Tre olika typer av facetter visas i Figur 1a) som färgade ytor, och kan ses ha olika mönster av atomer. Är kristallen inte orienterad gentemot ett plan överlappar atomerna varandra, och det är svårt att urskilja hur atomerna är positionerade, (Figur 1b).
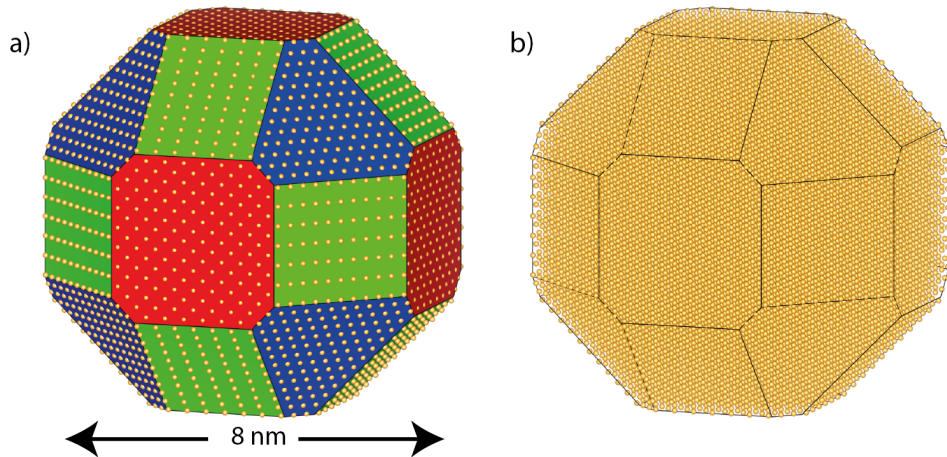
Figur 1. a) 3D modell av kristallin nanopartikel av guld med tre olika ytor (facetter). Ytorna markerade i rött, grönt och blått och har olika mönster av atomer. b) Kristallen består av cirka 30 000 atomer i ett regelbundet mönster.

Genom att rotera partikeln så att den avbildas vinkelrätt mot exempelvis, en röd yta (Figur 2a) hamnar atomerna i led och ett periodiskt mönster av atomer syns, (Figur 2b). Ordningen i mönstret kan användas för att bestämma materialets kristallstruktur, som skiljer sig mellan material.
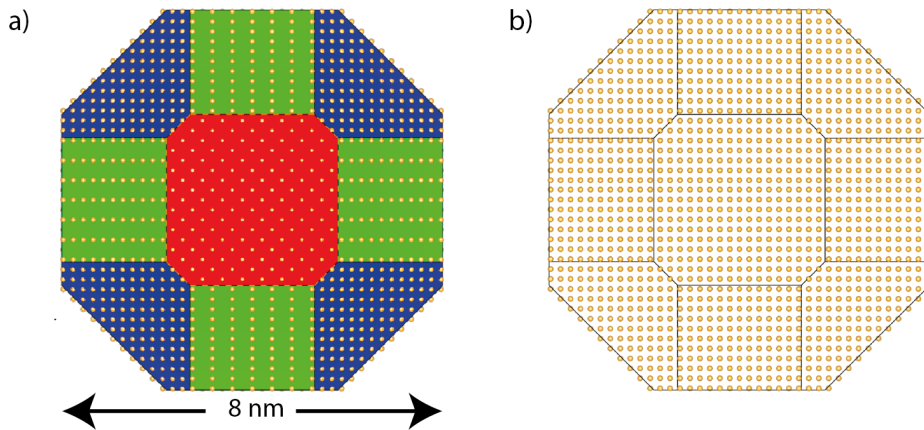
Figur 2. Kristallen är nu orienterad vinkelrätt mot en röd facett, och de tre färgade facetter ses ha olika mönster av atomerna. b) Atomerna är positionerade i led och därmed syns mellanrum i kristallen och ett 2D mönster som kan användas för att bestämma periodiciteten i 3D (kristallstrukturen).

Nanopartiklar är för små för att urskiljas i ett konventionellt ljusmikroskop och istället används olika typer av elektronmikroskop. I ett elektronmikroskop accelereras elektroner till höga hastigheter och färdas genom vakuum mot provet. Elektronerna styrs med hjälp av elektromagnetiska linser som böjer av elektronerna och påverkar deras väg för att skapa en elektronstråle som belyser provet. Beroende på vilken typ av elektronmikroskopi som används, kan exempelvis provets ytor eller inre struktur undersökas. I denna avhandling har två olika typer av elektronmikroskopi använts, svepelektronmikroskopi (SEM) och transmissionselektronmikroskopi (TEM).

Med SEM, fokuseras elektronstrålen till en liten punkt som tränger djupt in i provet. De inkommande elektronerna har hög energi och interagerar med provet på olika vis, vilket resulterar i att bland annat röntgenstrålning och svagt bundna elektroner bryter sig loss. Elektroner som bryter sig loss nära provets yta samlas in av en elektrondetektor med hjälp av ett elektriskt fält som likt en dammsugare samlar in elektronerna. Antalet detekterade elektroner per belyst punkt motsvarar ljusstyrkan hos en pixel i en bild. Elektronstrålen sveper sedan hastigt över provet och bygger upp en bild av provet pixel efter pixel. SEM används för att undersöka formen och storleken hos de producerade nanopartiklarna och nanotrådarna. I Figur 3, visas exempelbilder tagna med SEM av a) nanopartiklar och b–d) nanotrådar. Nanopartiklarna är cirka 40–50 nm i diameter, och nanotrådarna är cirka 1000–2000 nm långa.
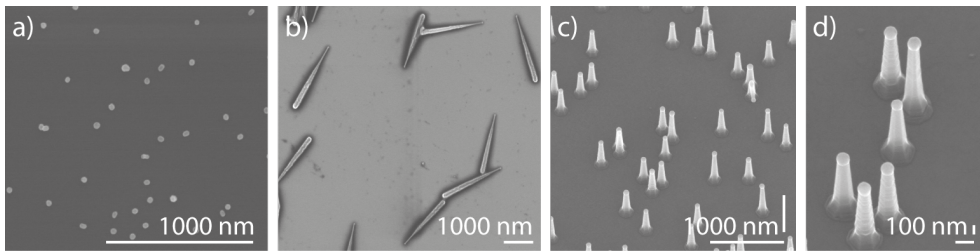
Figur 3. SEM bilder av olika typer av nanostrukturer på ett substrat. a) nanopartiklar av Pd med en diameter på 40 nm. Nanotrådar som b) ligger ned och c–d) står upp på ett substrat.

Även för TEM, skapas det röntgenstrålning i provet efter att elektronstrålen interagerar med provet. Energin på röntgenstrålningen är ämnesspecifik, och används för att bestämma vilka grundämnen provet består av. TEM används därför ofta för att undersöka den kemiska sammansättningen och kristallina strukturen hos de producerade nanopartiklarna och nanotrådarna. Nanopartiklar eller nanotrådar överförs till en speciell provhållare som kallas en TEM grid.

För TEM är det viktigt att provet är väldigt tunt (gärna mindre än 50 nm) för att elektronerna ska ta sig igenom provet och bidra till en högupplöst TEM bild. Då elektronerna tar sig igenom provet går det att skapa en bild, genom att fokusera de transmitterade elektronerna med elektronlinser. Ett modernt TEM har en upplösning bättre än 0,2 nm och kan urskilja det periodiska mönstret hos atomer i en kristall. I Figur 4a), visas en SEM bild av en TEM grid som består av en koppardisk med ett fint rutnät. Varje ruta är cirka 0,15 mm i diameter, och är delvis täckt av en tunn kolfilm, (Figur 4b). Kolfilmen är typiskt transparent för elektronstrålen och proverna sitter fast på kolfilmen, (Figur 4c).
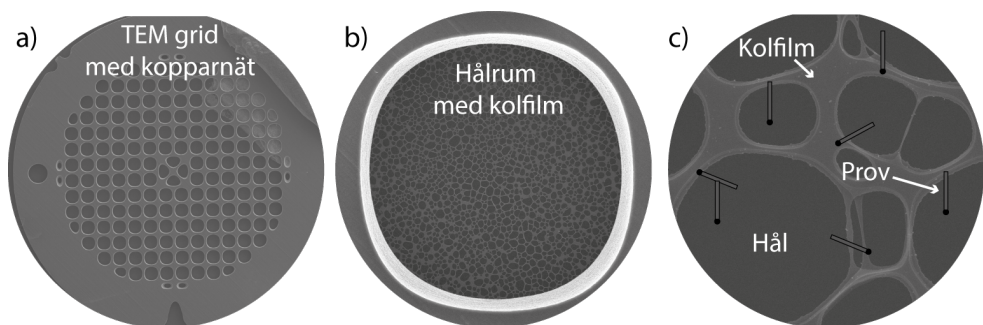
Figur 4. SEM bild av en a) TEM grid, vars kopparnät har hålrum med en diameter på cirka 0,150 mm. b) I ett hålrum finns det en transparant c) nanometertjock kolfilm som håller upp provet, t.ex. nanotrådar (schematiskt illustrerade).

I mitt arbete har jag skapat olika typer av enkristallina nanopartiklar med en diameter på 5–50 nm. Nanopartiklarna har producerats som en aerosol med en gnistgenerator, (Figur 5a). I gnistgenerator sker en högfrekvent elektrisk urladdning mellan två elektroder, som förångar elektroderna för att skapa nanopartiklar. Nanopartiklarna fortsätter att växa genom att kollidera med varandra och fortsatt kondensering. Då nanopartiklarna blir större än cirka 5 nm i diameter är de inte längre sfäriska utan skapar istället kluster av nanopartiklar som kallas aggregat, (Figur 5b). Aggregaten kompakteras till rundare nanopartiklar genom uppvärmning av aerosolen, (Figur 5c), och skapar enkristallina nanopartiklar, (Figur 5d).
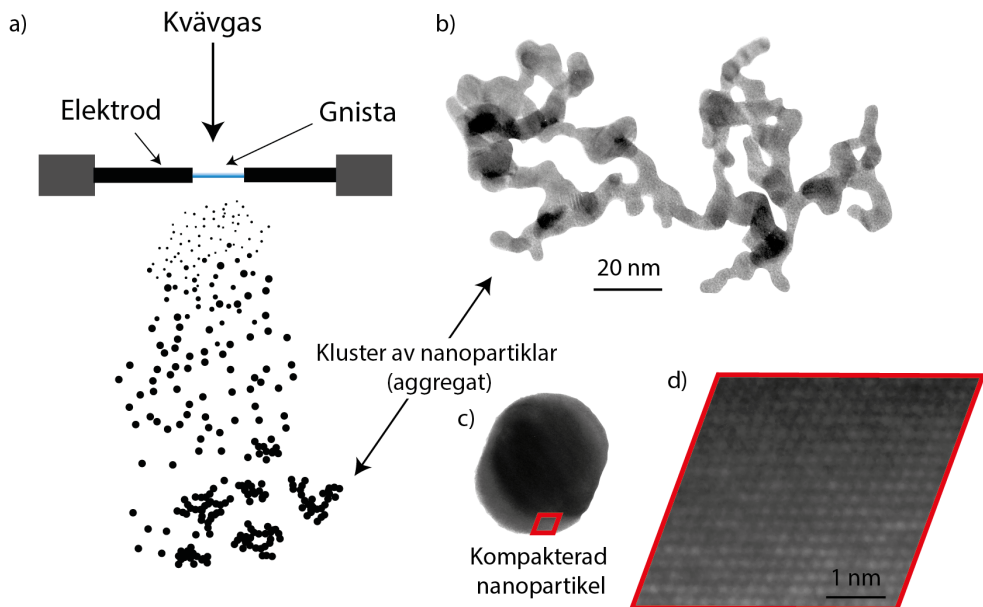
Figur 5.a) När en gnista slås mellan två elektroder förångas elektroderna och skapar nanopartiklar. Då det är många nanopartiklar kolliderar de och bildar b) kluster av nanopartiklar (aggregat) som vid uppvärmning kan kompaktera till c) mer runda och väldefinierade nanopartiklar. d) Periodiskt mönster av atomer i nanopartikeln.

Beroende på hur fria nanopartiklarna är från föroreningar, vad de har för smälttemperatur och vid vilken temperatur de värms så kompakterar de olika mycket. Jag har visat att en låg koncentration av vätgas utspädd i kvävgas är tillräckligt för att förhindra att material som vismut, tenn och kobolt oxiderar. Tidigare, har man försökt ta bort oxiden i efterhand men det har visat sig vara både mer komplicerat och mindre effektivt.
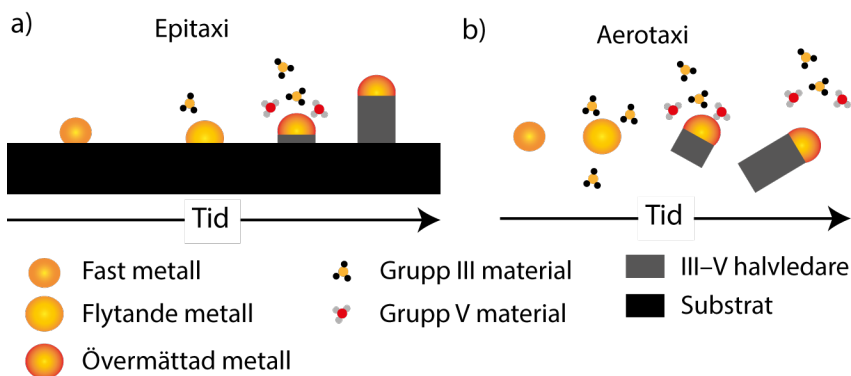
III–V nanotrådar

Vissa grundämnen från grupp III och V i periodiska systemet skapar tillsammans III–V halvledare. En halvledare är ett material som med extern påverkan kan byta mellan att vara en ledare eller isolator. Med III–V halvledare kan betydligt snabbare och effektivare lysdioder, solceller och elektronik skapas än vad som är möjligt med kisel som utgör grunden för dagens elektronik. Till skillnad från kisel, är det dock både svårt och dyrt att skapa stora enkristallina III–V kristaller vilket är en nödvändighet för många applikationer. Med en nanotrådsgeometri kan mängden III–V material i många fall minskas. Till exempel, för solcellapplikationer har det visat sig räcka att cirka en tiondel av ytan är täckt med nanotrådar, då nanotrådarna likt antenner effektivt fångar in solljuset. Solljus består av ett brett spektrum av våglängder, och en konventionell solcell består bara av ett halvledarmaterial som absorberar en viss del av solens spektrum. Genom att använda kombinationer av olika halvledare kan komplementära delar av solens spektrum absorberas, för att på så vis öka solcellens effektivitet. Dessvärre är sådana solceller i dagsläget så pass dyra att de bara används i nischade solceller för exempelvis rymdapplikationer.

En vanlig metod att skapa halvledarkristaller är med epitaxi, som kommer från grekiska orden *epi* och *taxis* som betyder ovan och ordning. Epitaxiell växt syftar till att ett nytt atomlager placeras med hänsyn till det underliggande atomlagret. Halvledare med samma kristallstruktur kan dock ha olika avstånd mellan atomerna, vilket orsakar problem vid epitaxiell växt då kristallerna behöver expanderas och komprimeras för att skapa en gemensam gränsyta. Detta orsakar inre spänningar i de två kristallerna som eventuellt skapar oönskade avvikelser i kristallstrukturen. Nanotrådar hanterar inre spänningar bättre än traditionell 2D epitaxiell växt och möjliggör därmed fler kombinationer av III–V material.

I denna avhandling, har nanotrådar av indiumarsenid och galliumarsenid växts med hjälp av olika metallpartiklar. Indium och gallium är exempel på grupp III ämnen och arsenik ett grupp V ämne. De två växtmetoderna som använts är epitaxi och aerotaxi.

Vid epitaxiell växt, placeras nanopartiklar på ett substrat som vid uppvärmning och ett tillflöde av grupp III material legerar tillsammans, (Figur 6a). Därefter tillförs även grupp V material och partikeln bygger upp nanotråden ett atomlager åt gången. Genom att ändra på tillförseln av de olika materialen kan den kemiska sammansättningen på nanopartikeln och nanotråden förändras.

Figur 6. Nanotrådar av III–V halvledarmaterial kan skapas från metallnanopartiklar. a) Epitaxiell växt innebär att nanotrådarna har växt från ett substrat med liknande kristallstruktur som nanotråden. Nanopartikeln absorberar III–V material från en tillförd gas, blir övermättad och kristalliserar III–V material. b) I aerotaxi används inget substrat utan nanotrådar växer direkt från aerosolnanopartiklar.

När man växer nanotrådar med aerotaxi behövs inget substrat, (Figur 6b). Istället används aerosolnanopartiklar som direkt i ett gasflöde värms upp och där även grupp III och V material tillsätts. Då detta inte kräver något substrat, kan nya nanotrådar skapas kontinuerligt i ett gasflöde där nya nanopartiklar och III–V material tillförs. Typiska nanotrådsväxthastigheter är 0,1–10 nm per sekund för epitaxi, och 100–10 000 nm per sekund för aerotaxi. I dagsläget producerar en aerotaxi-forskningsreaktor cirka 1 miljard nanotrådar i minuten, medan en pilotreaktor producerar cirka 100 miljarder nanotrådar i minuten. En fortsatt ökad produktionshastighet är nödvändig då det för en optimal solcell behövs cirka 5 000 miljarder nanotrådar per m^2.

När nanopartikeln legerar med grupp III ämnen som gallium eller indium, sänks dess smälttemperatur avsevärt och nanopartikeln kan bli flytande under nanotrådsväxt. I Figur 7a), visas smälttemperaturen för guld legerat med indium, vars smälttemperatur drastiskt sjunker från 1064 till 156 °C beroende på koncentrationen indium. Andra metaller, som palladium, visar inte en lika drastisk sänkning, utan kräver högre temperaturer eller högre grupp III koncentration för att bli flytande vid nanotrådsväxt, (Figur 7b). Nanotrådsväxt från fasta partiklar har visat sig vara svårare att hantera och därför är det av intresse att styra huruvida partikeln är flytande eller fast.
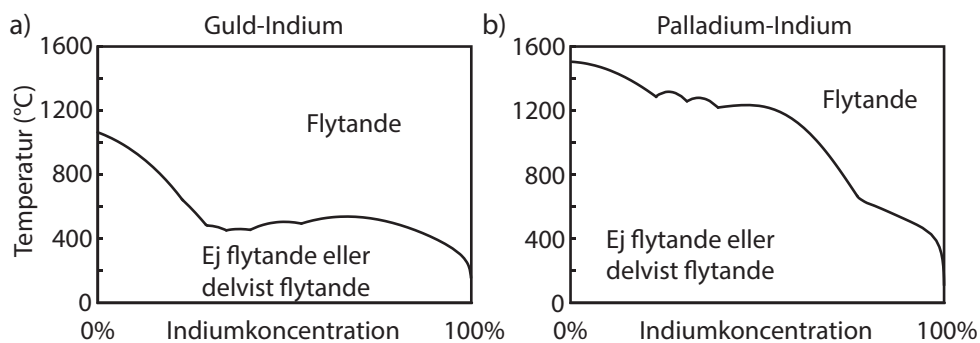
Figur 7. Smälttemperatur för a) guld-indiumlegering och b) palladium-indiumlegering. Temperaturer ovanför linjen motsvarar en flytande legering och temperaturer under består av en eller flera fasta faser.

Genom att kontrollera grupp III koncentrationen, går det därmed att styra huruvida partikeln ska vara flytande eller fast vid en viss temperatur. Nanopartiklar med för låg indiumkoncentration förväntas vara fasta under nanotrådsväxten och ger ofta okontrollerad nanotrådsväxt, som i Figur 8a). Nanopartiklar med en hög indiumkoncentration är mer benägna att vara flytande under nanotrådsväxten, och skapar oftast raka mer kontrollerade nanotrådar, som exemplet i Figur 8b).
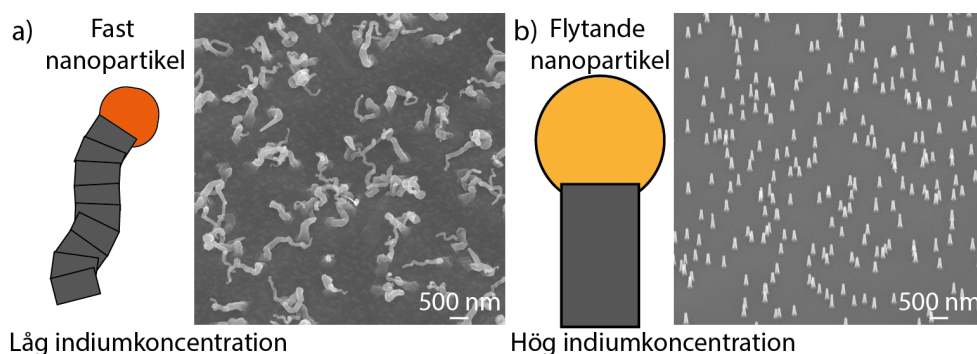
Figur 8. Schematisk ritning av a) okontrollerad nanotrådsväxt från en fast nanopartikel, p.g.a. låg indiumkoncentration, och kontrollerad nanotrådsväxt från en flytande nanopartikel, p.g.a. hög indiumkoncentration. Exempel på de två typerna av nanotrådar visas i SEM bilderna bredvid.

I min forskning visar det sig att palladium och guldpartiklar med en hög indiumkoncentration ger närmast identiska välkontrollerade nanotrådar. Genom att gradvis ändra indiumkoncentrationen förändras nanopartikelns smälttemperatur och när indiumkoncentration sänks under ett kritiskt värde, blir nanotrådsväxten ostabil. Genom att undersöka kompositionen med TEM, påvisade vi att detta sannolikt är på grund av att nanopartikeln övergår från flytande till fast fas.

Som legering med indium, tenderar andra metaller att ha en smälttemperatur mellan det hos palladium och guldlegeringen. Därmed förväntas det att indiumrika nanopartiklar kan vara av stor nytta även för andra metaller och möjliggöra fler val av material hos nanopartikeln. Då fler materialkombinationer blir tillgängliga minskar beroendet av guld, och billigare alternativ som är förenliga med kiselteknologin blir tillgängliga. I framtiden hoppas jag att valet av nanopartikelmaterial blir lika självklart som valet av halvledare i nanotråden, det vill säga, att det bestäms efter den tänkta applikationen.

List of Papers

This thesis is based on the following papers, which will be referred to in the text by their roman numerals.

I. Hydrogen-assisted spark discharge generated metal nanoparticles to prevent oxide formation

   Robert T. Hallberg, Linus Ludvigsson, Calle Preger, Bengt O. Meuller, Kimberly A. Dick, Maria E. Messing, *Aerosol Science and Technology*, 52, 347–358. (2017)

   I defined the project and played a leading role in the development and execution of the experiment and the analysis. I did most of the production and characterization of nanoparticles, including SEM, TEM, sintering scans and data analysis, except for the XRD measurements and analysis. I wrote the paper.

II. Palladium-seeded GaAs nanowires

   Robert T. Hallberg, Sebastian Lehmann, Maria E. Messing, Kimberly A. Dick, *Journal of Materials Research*, 31(2), 175–185. (2016)

   I pursued a project defined by my supervisors and was supported in the planning of the initial experiments, as well as in the interpretation and presentation of the results. I performed the experimental work for nanoparticle preparation and nanowire growth, and all the SEM analysis. I performed some independent TEM studies, but was mainly assisted in both the TEM data acquisition and analysis. I wrote the paper.

III. Group III-rich particle assisted growth to enable VLS from high melting point seed metals.

   Robert T. Hallberg, Maria E. Messing, Kimberly A. Dick, *Manuscript* (2018)

   I planned and executed the project independently, and wrote the paper.

Acknowledgements

I am most grateful for having had three excellent supervisors, who have both supported and challenged me throughout my PhD studies.

At a workshop I attended, I learnt that happiness as a PhD student depends on the relationship between the supervisor and student. As I have had an overall enjoyable experience, there is strong evidence that Kimberly Dick is an excellent supervisor. This is not surprising, considering her many great qualities. I greatly appreciate the time she took to listen and discuss with me when I was confused, and the indirect approach to supervision, which allowed me to grow and evolve in my own way. This may not always be the fastest way, but it was valuable to me.

Before I met Maria Messing, I was convinced that pursuing a PhD was not for me, but encountering her during my undergraduate studies made me question this. Now, as I approach the end of my PhD studies, I am glad that she gave me this opportunity. Among her many strengths are her positive attitude and frank personality.

I am also very glad to have had Martin Magnusson as a supervisor since the early stages of my PhD. Martin can brighten any discussion, and is an unending source of interesting ideas, facts and trivia.

I have always regarded Sebastian Lehmann as an unofficial supervisor. As a senior researcher he has been of great help discussing science, and in experiments, and writing. I also appreciate that he told me not to worry too much over disheartening results in the initial stages, as it was better to meet hardships early on so that one has time to learn from them.

I have been blessed with being able to work in not one, but two, research groups: the Nanowire Growth Group and the Aerosol Group. I wish to thank all the members of both groups for the open and interesting discussions we have had over the years. Thanks to everyone in the Nanowire Growth Group: Carina, Daniel, Erik, Hanna, Heidi, Karl W., Luna, Markus, Martin, Reza Z., Rong and Sepideh, and in the Aerosol Group: Bengt, Calle, Knut, Namsson, Linus, Sara T., Sudhakar, Sara B., Sara T., and Timothy. I wish you continued great discussions and an endless supply of cake.

To my current and former PhD colleagues: Alexander, Ali, Amin, Artis, Bekmurat, Chunlin, Damiano, David T., Egor, Fangfang, Florinda, Fredrik, Frida, Gaute,

Abbreviations

AsH$_3$	Arsine
CCS	Close-coupled showerhead
CVD	Chemical vapor deposition
DMA	Differential mobility analyzer
ESP	Electrostatic precipitator
fcc	Face-centered cubic
FFT	Fast Fourier transform
FWHM	Full width at half maximum
LED	Light emitting diode
MBE	Molecular beam epitaxy
MO	Metal organic
MOCVD	Metal organic chemical vapor phase deposition
MOVPE	Metal organic vapor phase epitaxy
PAG	Particle-assisted growth
SADP	Selective-area diffraction pattern
SDG	Spark discharge generator
SEM	Scanning electron microscopy
STEM	Scanning electron transmission electron microscopy
TEM	Transmission electron microscopy
TMIn	Trimethylindium
TMGa	Trimethylgallium
VLS	Vapor-liquid-solid
VS	Vapor-solid
VSS	Vapor-solid-solid
XEDS	Energy-dispersive X-ray spectroscopy
ZB	Zincblende

Contents

1. Introduction

Most of today's electronic and photovoltaic devices are based on the semiconductor material Si. Compound semiconductors of group III and V elements constitute the III–V family of semiconductors, which provide superior material properties to Si. However, III–V semiconductors are more difficult and expensive than Si to fabricate with conventional methods. To reduce the production cost and increase the crystal quality of III–V semiconductors, they can be grown as small nanocrystals or nanowires. Nanowires can be grown from a nanoparticle (seed) using a method called particle-assisted growth (PAG), which selectively increases the growth rate between the nanoparticle and the substrate to form high-aspect-ratio nanowires. Au is by far the most commonly used metal seed since it has been shown to seed nanowires of various III–V semiconductors. However, Au is not only a very expensive metal, but it is unsuitable for Si-based devices, as it easily diffuses and causes deterioration of the electronic properties of the device[1]. Therefore, if PAG is to be used to produce III–V semiconductors that is directly integrated with conventional Si technology, alternative metal nanoparticles must be found.

Extensive research has been carried out on III–V nanowire growth using different seed metals[2] including: Ag[3–9], Bi[10], Cu[11–13], Fe[14], Mn[15,16], Ni[17,18], Pd[19–23], and Sn[24–27]. However, nanowire growth using these metals as seeds appears to be significantly more challenging than nanowire growth from Au seeds. The reason for the apparent superiority of Au is not entirely clear, but its low melting point when alloyed with group III elements is a probable explanation. In addition, other metals are more easily contaminated during nanoparticle fabrication, processing and transport, as they are not as inert as Au. To develop alternative metals, it is therefore important to study their ability to form alloys with group III metals and to take precautions to prevent contamination and oxidation.

In the work described in this thesis, a spark discharge generator (SDG) was used to generate nanoparticles of various metals: Ag, Au, Bi, Co, Pb, Pd, Pt, Rh, and Sn. These nanoparticles were then used to study the effect of the seed particle composition on nanowire growth. Unfortunately, non-noble metals may partially oxidize, even at very low oxygen concentrations, and a study was therefore carried out into ways of preventing nanoparticle oxidation to improve the nanoparticle quality (Paper I). In the studies presented in Papers II and III, GaAs and InAs nanowires

(two III–V semiconductors) were grown from Au and Pd metal nanoparticles. Pd has a much higher melting point than Au, and is probably a solid during nanowire growth, unless alloyed with considerably group III concentrations. A method of lowering the melting point of an arbitrary seed metal was developed to improve nanowire morphology and obtain a well-defined nanowire growth direction.

An often-neglected alternative is to use alloy nanoparticles to provide even greater freedom in the nanoparticle melting temperature[28]. The SDG was used to generate size-selected Ag and Au seed particles, and three alloys: $Ag_{75}Au_{25}$, AgAu, and $Ag_{25}Au_{75}$, and nanowire growth from the Ag, Au and AgAu alloy nanoparticles was compared. The nanowires were grown in a gas phase in an Aerotaxy reactor, which allows the high-volume production of low-cost III–V nanowires.

Nanotechnology

Nanotechnology refers to the manipulation of matter on the nanometer scale, where the material properties become size-dependent. Exactly when the material properties change depends on the materials and their properties, but dimensions of 1 to 100 nm are often referred to as the nano-scale. Nanotechnology is an interdisciplinary field in physics, chemistry, biology, medicine, and engineering. Nanotechnology can be used in many applications including, among others: disease diagnostics[29], drug delivery[30–34], water purification[35,36], batteries[37–39], photovoltaics[40], electronics[41], self-cleaning hydrophobic surfaces[42,43], catalysis[44,45], and antibacterial agents[46].

Technology acceptance

For a technology to be accepted by the public, the perceived benefits must outweigh the perceived risks. Genetic modification, pesticides, and human genetic engineering promise great benefits, but the risks are regarded by many as unacceptable, which may limit their further development[47]. In contrast, other technologies, such as solar power, vaccination and light-emitting diodes (LEDs) are widely accepted. It is therefore important to bear the risks in mind, otherwise the future of nanotechnology may be jeopardized. Studies should therefore be carried out on the toxicity of nanomaterials[48], exposure pathways [49] and life-cycle analysis[50].

Top-down or bottom-up

Nanoscale devices can be fabricated using either a top-down or bottom-up approach. Top-down techniques selectively remove parts of a bulk material to create nanostructures. This process can be highly controlled, but the composition of the nanostructure is ultimately limited by the bulk material. In the bottom-up approach, used in the present work, nanostructures are instead grown by the self-assembly of atoms, molecules or nanoparticles into specific structures. Once the process has been understood and optimized, this enables atomic-layer precision in the shape and composition of the nanostructure, and the production of high numbers of complex structures not available in bulk materials.

Nanoparticles

Nanoparticles constitute an important subgroup of nanomaterials, and the production of nanoparticles was one of the first nanotechnologies. Nanoparticles of Ag and Au have long been used to produce stained glass to decorate churches and glassware. The absorption spectrum of a nanoparticle is size-dependent due to surface plasmons, resulting in red colored glass for 3 to 30 nm Au nanoparticles[51].

Traditional methods of producing metal nanoparticles are chemical processing, mechanical milling or physical processing. A widely used chemical method is to reduce metal salts in aqueous or oil solutions to form colloidal nanoparticles[52], and provides excellent size control and high production rates[53]. However, costly and time-consuming post-synthesis steps are usually required to remove by-products and other contaminants[52]. Mechanical milling is a simple method of dividing a bulk sample into smaller particles, down to the scale of nanocrystals and/or nanoparticles. However, agglomeration and contamination pose serious problems because of the long milling times associated with nanoparticle production[54].

In the present work, nanoparticles were produced using physical processes, which are usually cleaner, but more expensive, than the above-mentioned methods. Common physical methods are thermal evaporation[55], and ablation by a laser[56] or spark discharge[57] in an inert gas, followed by condensation of the nanoparticles. No chemicals are involved, and if the nanoparticles are produced at moderate concentrations in an inert carrier gas, both contamination and agglomeration are avoided.

III–V Semiconductor nanowires

Bandgap

Electrons in a material can only occupy certain energy levels, which, in bulk materials, form bands of continuous energy levels. The highest band occupied by electrons (at absolute zero) is known as the valence band, and is separated from the conduction band by a bandgap. For a material to conduct, electrons must escape the valence band and reach the conduction band.

Materials are divided into three different categories according to their bandgap: metals, semiconductors, and insulators. Metals have a zero or negligible bandgap and conduct electricity well, whereas insulators have a large bandgap and conduct electricity poorly. A semiconductor has a conductivity between that of a metal and an insulator but, more importantly, its conductivity can be altered dramatically by the introduction of impurities and electrostatic fields. Devices can be designed for specific technological applications by controlling the impurity concentration and coupling the semiconductor to metals and insulators.

III–V Semiconductors

A III–V semiconductor consists of equal parts of group III elements (Al, Ga, In) and group V elements (N, As, P, Sb). Although expensive, III–V semiconductor are used in many applications such as smart phones, base stations for cellular telephony, fiberoptics, wireless networks, satellite communications, radar, radio astronomy, and defense systems[58]. In addition, III–V semiconductors can be used to fabricate much faster and more power-efficient transistors than traditional Si-based metal-oxide semiconductor transistors[59,60]. Since III–V semiconductors are much more expensive than Si, III–V-based devices are unlikely to completely replace Si, but will likely be used to complement existing Si technology. This can be done by growing a III–V semiconductor on top of Si. Unfortunately, Si and III–V crystals do not match perfectly, and the interface between a Si substrate and a III–V layer is therefore strained laterally. If the mismatch is too great, or the III–V layer is too thick, the layer will relax, and dislocations will form, which are detrimental to the performance of the device[61].

Nanowires

Nanowires are high-aspect-ratio nanostructures, typically with a diameter in the range 10 to 200 nm, that are constrained in two dimensions. Due to their small diameter, the lateral strain in a nanowire can be relaxed elastically without the formation of undesired defects[62,63]. Therefore, it is possible to grow defect-free III–V nanowires on lattice-mismatched substrates[64,65], and to form additional axial heterostructures along the direction of nanowire growth[66].

A nanowire can be grown by either suppression or enhancement of the crystal growth rate in selected directions at selected interfaces. In the present work, PAG was used to increase the growth rate at the crystal-particle interface compared to the growth rate at the substrate or nanowire sidewalls (Figure 1.1a and b). Growth in the radial direction can be prevented or reversed by using an etchant such as HBr[67] or HCl[68–70]. An alternative to PAG, is selective-area epitaxy, which uses a patterned oxide mask to define the initial growth-interface[71–73] (Figure 1.1c and d). An ideal mask prevents crystal growth everywhere except in the holes, and with optimized growth conditions radial growth above the mask is limited (but not fully). Temple-assisted selective area epitaxy[74,75], uses a very thick mask to confine the nanowires inside hollow tubes, and fully prevents radial growth, Figure 1.1e).
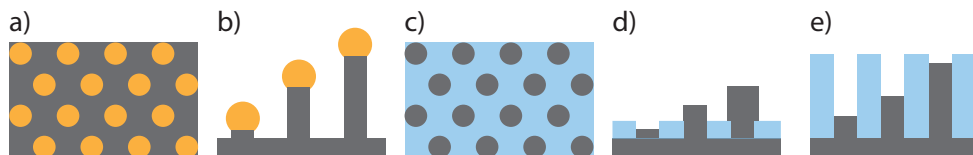
Figure 1.1. Schematics illustrating patterned PAG: a) top view and b) side view; selective-area epitaxy: c) top view and d) side view. e) Side view of template-assisted selective-area epitaxy.

Nanowire-based solar cells

The solar cells with the best efficiency are III–V multi-junction solar cells, which consist of several semiconductors with complementary bandgaps. The bandgap is directly related to the wavelength of the light that a semiconductor absorbs, and solar cell efficiency is increased by absorbing a larger proportion of the solar spectrum. The current efficiency record for a multi-junction solar cell under one sun illumination is 38.8%, but an efficiency of 46% has been demonstrated by condensing the light to an intensity of 508 suns[76]. This is almost twice the efficiency of the best Si-based solar cell, which has an efficiency of 24.4% at 1 sun, or 26.7% at 92 suns. This should be compared with the efficiency of a commercial Si-based solar cell of 17% under illumination of 1 sun. However, due to their high cost, III–V-based solar cells are currently limited to price-insensitive applications such as aerospace applications.

The cost of III–V multi-junction solar cells could be significantly reduced by using nanowire-based solar cells. Nanowires can act as waveguides to efficiently trap the incoming light[77]. Therefore, the nanowires can be sparsely spaced, reducing the amount of material required[78]. Nanowires can also be grown directly in the gas phase with Aerotaxy[79], eliminating the need for expensive substrates. The reported efficiency of a single-junction nanowire-based solar cell is still low: 13.8% for GaP[78], 15.3% for GaAs[80] and 11.4% for a tandem cell with GaAs nanowires on Si[65], but the efficiency is expected to improve with better device processing.

Disposition of this thesis

The next chapter, Chapter 2, provides some background information on how crystalline phases consist of ordered atoms and how their crystal structure can be characterized. The focus is on cubic crystals since they occurred most often in the present work. The crystal structures were identified using high-resolution transmission electron microscopy and the basic theory and method are explained. Finally, compositional analysis with energy dispersive X-ray spectroscopy is briefly explained.

Chapter 3 provides a background information on how thermodynamics governs the stability of phases, and how metastable phases strive to become stable. Capillary effects that modify the thermodynamic equilibrium of small systems are explained. In the present work, nanoparticles and nanowires were both grown by the condensation of a vapor and nucleation of a solid phase. The barrier for nucleation and an expression for the nucleation rate are given for the simple cases of nucleation in a gas phase and on pre-existing surfaces.

The aerosol system used in the present work is described in Chapter 4 as a sequence of three steps: generation, processing, and collection. Some unpublished results on the production rate of nanoparticles, electrode erosion, the size resolution of the equipment, compaction behavior of metal nanoparticles and unintentional evaporation of nanoparticles during compaction are also given. This chapter also highlights some of the results given in Paper I, namely that the generation of unoxidized and partially oxidized Bi nanoparticles depends on the H_2 concentration used when the nanoparticles are generated. Finally, a brief description of the production of AgAu alloy nanoparticles is also given.

The mechanism behind PAG is described in Chapter 5. The aim here is to provide a rudimentary understanding of the steps involved, from precursor to the completed nanowire.

Chapter 6 presents the experimental setup and some history concerning the two nanowire growth methods, metal organic vapor phase epitaxy (MOVPE) and Aerotaxy. Examples from the studies described in Papers II and III are highlighted to show how the nanoparticles and nanowires are developed.

The particle phase during nanowire growth is not as simple to determine as one might first believe. Chapter 7 discusses some of the reasons why this is the case, such as the uncertainty in the composition and temperature, combined with the fact that a typical phase diagram does not apply to nano-scale systems, nor systems that are not in thermodynamic equilibrium. Nanowires with different morphologies are presented, and some of the difficulties encountered in PAG when using alternative seed metals are illustrated. Three nanowire morphologies resulting from the study described in Paper II, defined as curly, inclined, and vertical, are presented, and it is argued that the curly nanowires were the result of uncontrolled growth from solid nanoparticles. A new growth method, called group III-rich PAG, was developed and demonstrated, allowing even high-melting-point metals such as Pd to be liquid at low growth temperatures. This is described in Paper III, and some of the results are highlighted in this chapter. Finally, the chapter ends with a discussion on how the cost of the seed metal in Aerotaxy can be reduced. Unpublished results show that AgAu-seeded GaAs nanowires work almost as well as Au-seeded GaAs.

In the final chapter, the main conclusions are presented together with suggestions for future research on PAG using alternative metals

2. Crystals and their characterization

The metal nanoparticles and III–V semiconductor nanowires fabricated in the present work were formed through the condensation of a vapor and nucleation of a solid crystal. A crystal consists of atoms or ions that are arranged in a regular repetitive pattern in three dimensions. Crystalline materials are often polycrystalline and consist of many crystallites (tiny crystals) oriented in different directions. However, with a controlled synthesis method it is possible to grow single crystals that are very useful in many electronic and optical applications. In order to be able to control the material properties, it is important to characterize the crystal structure and composition. In this chapter, the fundamentals of cubic crystals and the use of transmission electron microscopy for characterization are introduced.

Crystal lattice

A crystal lattice consists of a collection of lattice points arranged in a periodic pattern such that the surroundings of each lattice point are identical. In materials science, lattice points describe the arrangement of atoms or ions in a crystalline solid. In a Bravais lattice, any lattice point at a position r can be described by the combination of the three lattice vectors a_1, a_2, and a_3, and a set of integers h, k, and l, known as Miller indices.

$$r = ha_1 + ka_2 + la_3$$

Each lattice point is associated with one or more atoms that form the basis of the lattice. In this work, two cubic crystals are common, the face-centered-cubic (fcc) and zincblende (ZB) crystal structures. Both crystal structures share the fcc lattice, but ZB consists of two different atoms, and has a basis of two instead of one. Crystals with the same crystal structure can have different lattice constants, which means that the interatomic distances differ.

The unit cell of fcc-Au has 8 atoms, one on each corner, and 6 atoms centered on each face (Figure 2.1a). Since the unit cell crosses the center of each atom, only a fraction of each atom is within the unit cell, four complete atoms being in each unit cell. The width of the cube is defined as the lattice constant (a_0), and with an atom placed at the origin, the cube edges define the lattice vectors a_1, a_2, and a_3. For a cubic system, the lattice vectors are orthogonal and of equal length. For non-cubic systems, the lattice vectors can have different lengths and oblique angles.

The Miller indices can be used to describe points hkl, specific crystallographic planes (hkl) and specific directions $[hkl]$ according to the lattice vectors. The Miller indices of a plane are defined as the inverse intercepts along the lattice vectors, or equivalently (hkl) denotes a plane that intercepts the three points $\frac{a_1}{h}, \frac{a_2}{k}$, and $\frac{a_3}{l}$ at some point. By convention, hkl is rescaled to the smallest integer, and negative numbers are written as bars above the number, hence a plane that intercepts the two axes at: $0.5a_1, -1a_2$, but never intercepts a_3 is denoted $(2\bar{1}0)$.
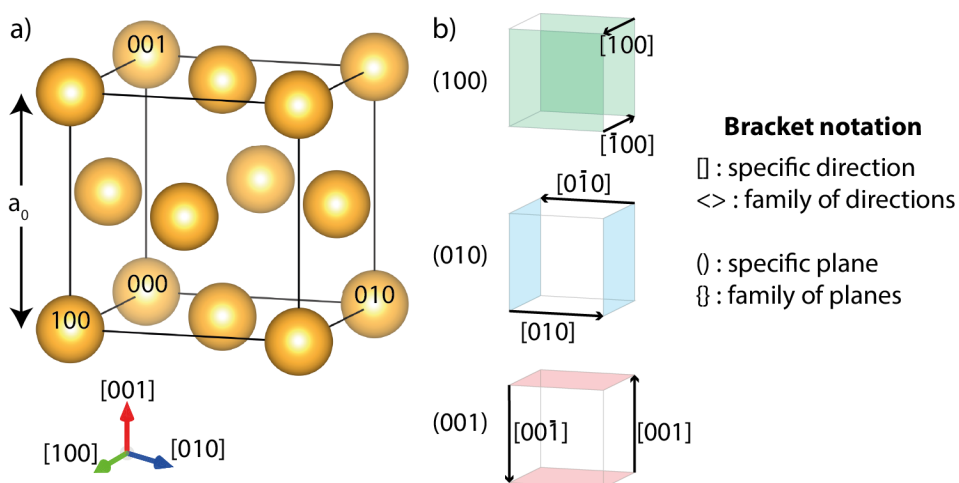
Figure 2.1. a) Unit cell of fcc-Au with lattice constant a_0. The bracket notation used to describe specific planes and directions, and their families, corresponding to all equivalent permutations is summarized. 3D visualization of crystal structures was performed with the software Visualization for Electronic and Structural Analysis.

The notation (100) describes an infinite number of equivalent planes (not to be confused with a family of planes) displaced along the normal of the plane (Figure 2.1b). In cubic systems, the normal to the plane (hkl) is described by the direction $[hkl]$. Crystals are highly symmetric, therefore other bracket notations are used to describe a family of directions $< hkl >$ or a family of planes $\{hkl\}$. For

example, $\{100\}$ refers to any or all of the six faces of the unit cell in Figure 2.1: $(100), (010), (001), (\bar{1}00), (0\bar{1}0), (00\bar{1})$ and have the normals $< 100 >$.

D-spacing

The spacing between (hkl) planes is known as its d-spacing (d_{hkl}), which, for a cubic system, is given by the following expression.

$$d_{hkl} = \frac{a_0}{\sqrt{h^2 + k^2 + l^2}}$$

It is directly apparent from the expression above that the highest values of d_{hkl} are found for the low-index planes, and that the difference in d_{hkl} is very small for high-index planes. Therefore, for crystal structure identification it is necessary to compare measured d-spacings with low-index d_{hkl} values of probable crystals. If higher order indices are used the values of d_{hkl} are indistinguishable. A summary of the geometrical relationship and d-spacings for common fcc and ZB structures is given in Table I.

Table I. The largest d-spacings of crystallographic planes for: ZB-InAs, ZB-GaAs, fcc-Ag, fcc-Au, and fcc-Pd. Not all planes are visible with diffraction-based techniques (as explained in the next section).

$\{hkl\}$	$\dfrac{a_0}{d_{hkl}}$	d_{hkl} (Å)					Visible reflection
		InAs	GaAs	Ag	Au	Pd	
$\{100\}$	1	6.04	5.65	4.09	4.07	3.99	No
$\{110\}$	$\sqrt{2}$	4.28	4.00	2.89	2.88	2.82	No
$\{111\}$	$\sqrt{3}$	3.48	3.26	2.36	2.35	2.30	Yes
$\{200\}$	2	3.02	2.83	2.04	2.04	2.00	Yes
$\{112\}$	$\sqrt{6}$	2.47	2.31	1.67	1.66	1.63	No
$\{220\}$	$2\sqrt{2}$	2.13	2.00	1.44	1.44	1.41	Yes

Zone axes

Transmission electron microscopy (TEM) can be used to resolve the periodic arrangement of lattice planes in a crystal. To achieve this, the incident electron beam is aligned with a zone axis $< uvw >$ of the crystal, by rotating the crystal. Figure 2.2a) shows a 3D model of an fcc-Au crystal along the $[011]$ zone axis. Each atom in the image consists of a stack of atoms perpendicular to the zone axis (viewing direction), and different crystallographic planes can be visualized by connecting atoms with a line.
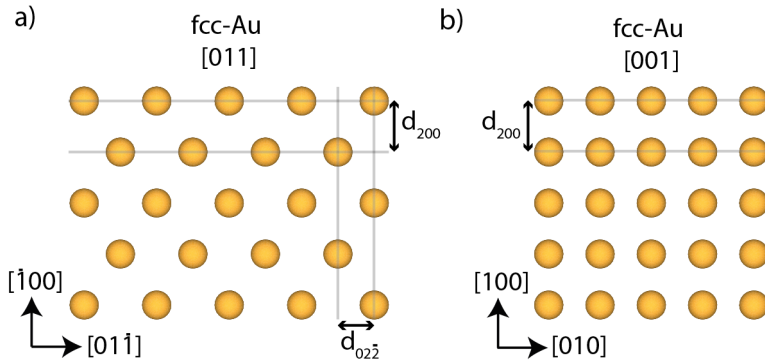
Figure 2.2. 3D model of fcc-Au viewed from: a) [011] and b) [001].

For example, in Figure 2.2a), horizontal lines centered on a row of atoms yield (100) or (200) planes, and the spacing between them corresponds to d_{100} or d_{200}. Similarly, vertical lines centered on a row of atoms correspond to the $(02\bar{2})$ planes separated by $d_{02\bar{2}}$. By rotating the crystal to a different zone axis, such as $[001]$, other planes become apparent, while others disappear (Figure 2.2b). An infinite number of planes can be constructed from an infinite number of hkl combinations. However, not all the planes contain atoms or are resolvable with TEM.

Zincblende

The stable crystal structure of bulk III–V semiconductors is cubic ZB, except for GaN, which instead forms hexagonal wurtzite[81]. ZB is also known as sphalerite, and is described by an fcc lattice with the basis of two different atoms (Figure 2.3a). By convention, the positive group III atom (cation) is referred to as an A atom, and is placed on the corners of the unit cell. The negative group V atom (anion) is referred to as a B atom, and is displaced from the A atom by ¼ < 111 >. For each A atom there are four nearest neighbors of B atoms in a tetrahedral arrangement (Figure 2.3b).
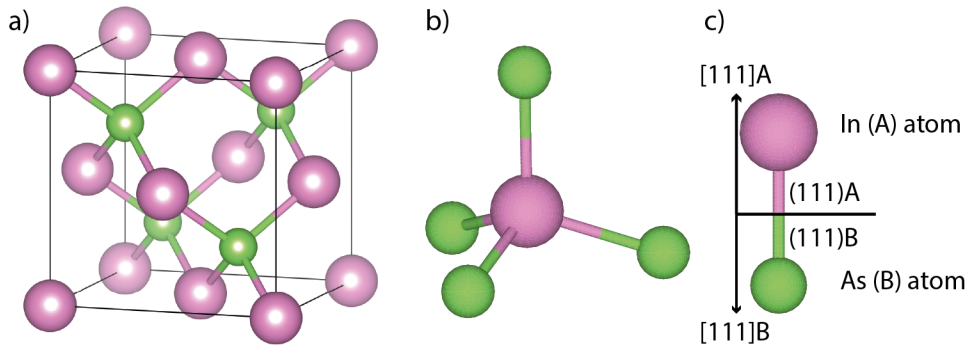
Figure 2.3. a) Unit cell of ZB-InAs, which consists of In and As atoms in a tetrahedral arrangement, b). c) Shows a schematic of the In-As dumbbell, with polarity relations summarized.

Since ZB consists of two types of atoms, directions and planes that are equivalent in fcc crystals, are not necessarily equivalent in ZB. From the unit cell definition with A atoms at the origin, the B atoms are displaced along a [111] direction, referred to as the [111]B direction. Note, that if instead the B atoms are at the origin, the [111]B direction refers instead to $[\bar{1}\bar{1}\bar{1}]$. A summary of the polarity of surfaces and directions for [111] and (111) is shown in Figure 2.3c).

Crystal structure identification

An alternative way of viewing a lattice is to use its reciprocal lattice, which is the Fourier transform of the real lattice. In TEM, a reciprocal space image can be constructed by performing a fast Fourier transform (FFT) of an image of the atomic arrangement, or by imaging the diffraction pattern. In reciprocal space, each spot corresponds to a reflection from a set of lattice planes (hkl) of the real lattice, and its distance from the origin is proportional to $\frac{1}{d_{hkl}}$. Planes that fulfill the Weiss zone law:

$$0 = hu + kv + lw$$

are normal to the zone axis and may appear as spots in the reciprocal space image.

For a single crystal, the spots are symmetrically arranged around the zone axis, and their relative positions can be used to identify a crystal structure[82]. The relative position is described by $\frac{1}{d_{hkl}}$, and the angular separation (θ) of two reflection spots $(h_1 k_1 l_1)$ and $(h_2 k_2 l_2)$, which is given by:

$$\cos(\theta) = \frac{h_1 k_1 l_1 \cdot h_2 k_2 l_2}{|h_1 k_1 l_1||h_2 k_2 l_2|}$$

To index an unknown crystal structure, it is necessary to view the crystal from multiple zone axes. However, for an engineered nanostructure, there are only a limited number of feasible crystal structures, and the crystal structure can therefore, often be identified by comparing the θ and d_{hkl} relationships to that of reference crystal structures. For instance, reciprocal space images of the two atomic arrangements in Figure 2.2 are depicted in Figure 2.4a and c.
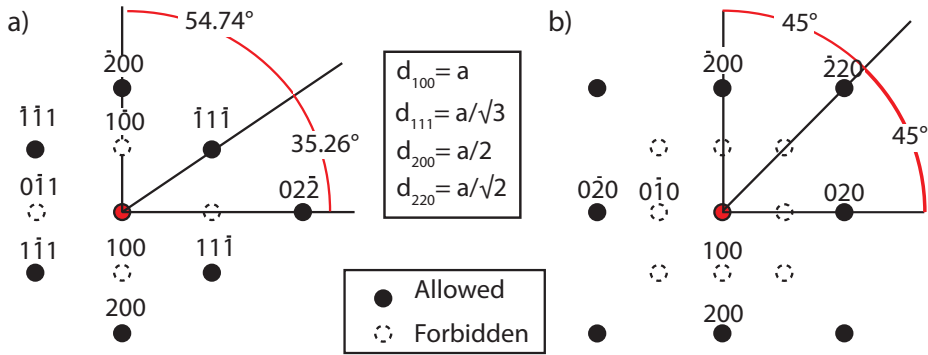
Figure 2.4. Reciprocal space schematic of fcc viewed from: a) [011] and b) [001].

Selection rules

The structure factor (F) describes the amplitude of a diffracted electron beam after interaction with a crystal lattice. From the symmetry of the unit cell, F for an fcc structure is:

$$F = f\{1 + \exp(\pi i(h + k)) + \exp(\pi i(h + l)) + \exp(\pi i(k + l))\}$$

where f relates the amplitude of a scattered wave from a single atom. Here, F can take only two values:

$$F = 0, \qquad hkl, \text{mixed odd and even}$$

$$F = 4f, \qquad hkl, \text{all odd or even}$$

For (hkl) where $F = 0$, there is a zero intensity, its reflection is said to be forbidden and it will, thus, not show in reciprocal space (Figure 2.4a and b).

For ZB structures such as GaAs or InAs, f differs between group III and group V atoms, and there are several non-zero values of F which modify the relative intensity of the diffraction spots. However, a mixture of odd and even reflections is still forbidden, and will thus have zero intensity, as summarized below.

$$F = 0, hkl, \text{mixed odd and even}$$

$$F \neq 0, hkl, \text{all odd or all even}$$

Therefore, lower-index planes such as $\{100\}$, $\{110\}$, and $\{112\}$ of fcc and ZB structures are not visible with diffraction-based techniques, as was mentioned in Table I [82].

Close-packed directions and planes

A close-packed plane is the plane with the highest areal density of atoms, and consists of a monolayer of atoms for fcc-Au, but a bilayer of III–V atoms for ZB-InAs (Figure 2.5). For an fcc lattice, $\{111\}$ are close-packed planes, and $< 111 >$ are the corresponding close-packed directions.
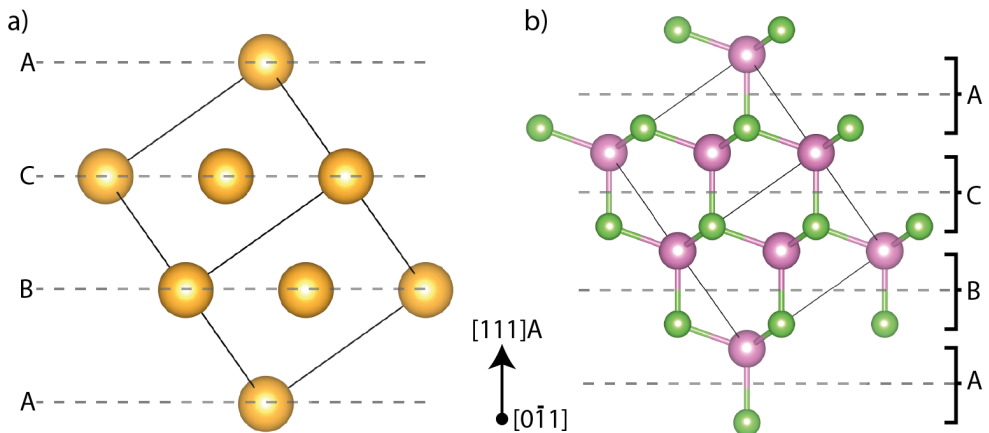
Figure 2.5. Schematics of: a) fcc-Au and b) ZB-InAs viewed along the $[0\bar{1}1]$ zone axis with a $[111]$A directed upwards. The close-packed layers are referred to as A, B, or C, depending on their relative positions.

The periodicity of the close-packed layers is known as the stacking sequence and differs between polytypes of a crystal. The first layer is denoted A and the second B, but depending on whether the third layer is translated with respect to the first layer, it is either an A or a C layer (Figure 2.5a and b). The lower-order polytypes include 2H (AB), 3C (ABC), 4H (ABCB), and 6H (ABCACB), but become increasingly rare at higher orders. A perfect wurtzite crystal follows the 2H stacking (2 units and hexagonal) and a perfect ZB crystal follows the 3C stacking (3 units and cubic) as in the case of the two crystals illustrated in Figure 2.5.

III–V nanowires can be grown as perfect crystals[83–85], but if they are not optimized they are either twinned ZB or a mixture of ZB and wurtzite[86,87]. No wurtzite structures were identified in the present work, but they would be distinguishable from ZB when viewed along a $< 011 >$ zone axis due to 2H stacking.

Crystallographic twins

Deviations in the stacking sequence can result in the formation of a twin, and the **ABC**ABC stacking becomes **ABC**BA (Figure 2.6a). A twinned crystal is a crystal with the same symmetry but mirrored in a plane. Typically, in nanowire growth twinning occurs at the (111) growth interface between the particle and nanowire and, therefore, a twin plane transforms the structure between "twin 1" and "twin 2". The reciprocal space image of the twinned structure consists of two sets of spots, one for each twin (Figure 2.6b). The spots along the mirror axis are shared, but others are unique to each twin.
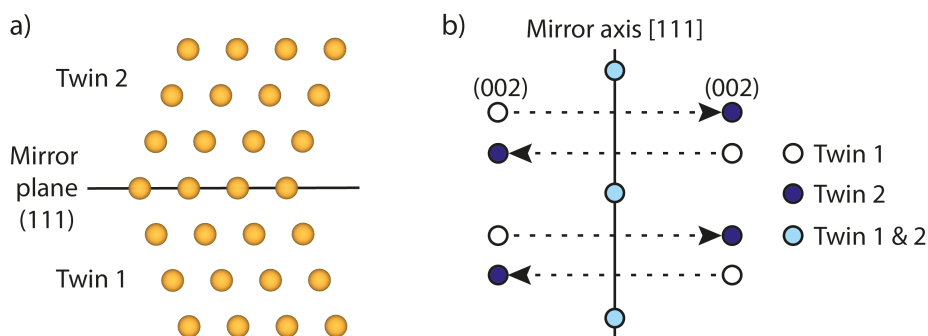
Figure 2.6. a) Schematic of a mirror plane (111) that separates two twinned fcc structures, twin 1 and twin 2. b) The reciprocal space image of the two structures, which shares some spots.

Compositional analysis

Energy-dispersive X-ray spectroscopy (XEDS) is a technique used in connection with TEM for compositional analysis. The electrons in the incident beam of a transmission electron microscope have a very high energy (typically 200 to 300 keV), which is enough to eject an electron from an inner electron shell, resulting in the creation of an electron hole. When an electron from an outer electron shell fills the hole, an X-ray may be emitted with an energy that corresponds to the difference in energy between the outer and inner electron shells. Since atoms have different electronic structures, the X-ray spectrum emitted is specific to each element and can be used for elemental identification.

In the setup used in the present work, a silicon-drift detector was used together with commercial analysis software for relative quantification of the elements. The Cliff–Lorimer relation was used for quantification, as it is valid for thin samples in TEM where self-absorption is negligible. Self-absorption refers to the X-rays emitted from within the sample that are absorbed by the sample before escaping from the sample, which complicates the analysis of thick samples.

$$\frac{C_A}{C_B} = k_{AB}\frac{I_A}{I_B}$$

Here, I_A and I_B are the relative peak intensities of elements A and B, and C_A and C_B are the relative concentration in weight percent (wt%). An individual k-factor (k_{AB}) must be used for each pair of elements, and in the present setup commercially calibrated k-factors were used.

Scanning electron microscopy (SEM) and scanning transmission electron microscopy (STEM) are techniques in which the electron beam is focused into a small probe. The probe is scanned across the sample in a grid pattern to illuminate a small area of the sample at a time, and the resulting spectrum is attributed to each pixel in the image. Note, that typically, the electron beam penetrates far (microscale) into SEM samples, and penetrates through STEM samples. In SEM, mainly secondary electrons are detected, which are low-energy electrons (<50 eV) originating from the top few nanometers of the sample surface. Therefore, SEM is a suitable technique for studying the morphology of nanostructures. High-angle annular dark field imaging is a common STEM technique in which the image is generated from highly scattered electrons (typically >3° for a 300 keV instrument)[82]. Large-angle scattering depends primarily on the sample thickness and atomic number (Z), therefore, the contrast is sometimes referred to as Z contrast or mass-thickness contrast[88].

3. Thermodynamics and nucleation

It is common knowledge that at a pressure of 1 atm ice melts at 0 °C, water boils at 100 °C, and that both the melting point and boiling point of water can be affected by the addition of salt or by a change in the surrounding pressure. When a system is subjected to a change in its surroundings, the relative stability of the phases changes, resulting in a phase transition. In this chapter, fundamental thermodynamics are introduced to explain phase transitions of bulk and nano scale systems.

The formation of a condensed (liquid or solid) phase is associated with an energy cost due to the formation of new surfaces or interfaces. This energy is known as an activation energy or a nucleation barrier, and can effectively prevent the precipitation of condensed phases. For instance, pure water vapor at 20 °C does not spontaneously form rain droplets unless the relative humidity is above 350% due to the high nucleation barrier[89]. However, in the presence of impurities such as aerosol nanoparticles, a relative humidity of only 100.36% is sufficient for droplets to form[89]. The properties that govern the height of the nucleation barrier and its relation to the nucleation rate are described in this chapter. The concepts are general, and are important in describing how and why a seed particle can increase the growth rate of semiconductor crystals, as well as how aerosol nanoparticles are formed. More specific theory is introduced in Chapters 4 to 7.

Chemical potential and supersaturation

Figure 3.1 shows the one-component (unary) phase diagram of water, where the equilibrium vapor pressure at which the liquid phase separates from the vapor phase can be seen. At thermodynamic equilibrium, the chemical potentials (μ) of the two phases are equal, and both phases are stable. The chemical potential at a set pressure (P) and absolute temperature (T) of phase α is described by:

$$\mu_\alpha = \frac{\delta G}{\delta N_{T,P}}$$

where G is the Gibbs free energy and N the number of moles of the α-phase. A phase with a higher chemical potential tends to react with a phase with a lower chemical potential such that atoms are redistributed between the phases to equilibrate the chemical potentials, until until thermodynamic equilibrium is reached.
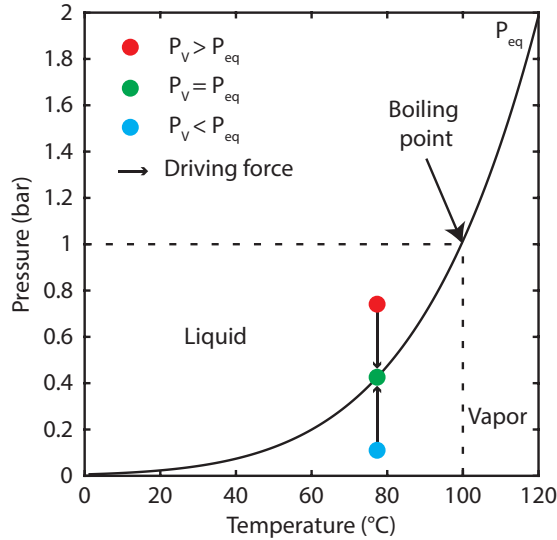
Figure 3.1. Vapor pressure of water. Red indicates supersaturated vapor, green saturated vapor, and blue unsaturated vapor. Upward and downward arrows indicate the thermodynamic driving force defined by the difference in chemical potential between the two phases.

The difference in chemical potential ($\Delta\mu$) of two phases (α) and (β) can be defined as:

$$\Delta\mu_{\alpha\to\beta} \equiv \mu_\beta - \mu_\alpha$$

and for an ideal unary system of a vapor (v) and liquid (l) can be expressed as:

$$\Delta\mu_{v\to l} \cong -RT \ln\frac{P_v}{P_{eq}}$$

where R is the universal gas constant, T the absolute temperature, P_v the partial pressure of the vapor and P_{eq} the equilibrium vapor pressure of the liquid phase. One of the simplest methods of supersaturating a vapor is cooling it rapidly (quenching) until P_{eq} falls below P_v. In contrast, if a vapor is heated until P_{eq} exceeds P_v, the

vapor becomes unsaturated. It is common to simply use the magnitude of $\Delta\mu$ to describe a supersaturated phase, hence, $\Delta\mu$ increases with supersaturation.

When the phase transition does not involve a vapor, it is more convenient to describe the difference in chemical potential as:

$$\Delta\mu_{l\to s} \cong -RT \ln\frac{c}{c_0}$$

where c is the solute concentration, and c_0 is the equilibrium concentration, also known as the solubility.

Capillary effects

Capillary effects are the effects of curved surfaces or interfaces on thermodynamic properties. In general, thermodynamic systems consist of more than one phase, for instance, a solid in connection with a vapor. The material properties of the interface or surfaces differ from those of the bulk, therefore, the material properties of nano-scale systems also differ from those of the bulk. A nano-scale system has a very high surface-to-volume ratio, and some material properties are highly size-dependent.

Two capillary effects that are relevant for nanowire growth and aerosol nanoparticle generation are highlighted and explained briefly below: increased vapor pressure and decreased melting point. The vapor pressure at the surface of a nanoparticle (p_s) is a function of the curvature $\left(H = \frac{2}{d}\right)$ of the liquid–gas interface. For a spherical nanoparticle with the diameter (d) this can be described by the Kelvin equation:

$$p_s = p_{eq} \exp\left(\frac{4\gamma V_M}{RT} \cdot \frac{1}{d}\right)$$

where V_M is the volume per mole of the condensed phase, and γ is the surface energy. The value of γ for a stable condensed phase must be positive, otherwise it would be energetically favorable for the condensed phase to disintegrate and form more surfaces. In PAG of nanowires, the higher vapor pressure of a small nanoparticle reduces the supersaturation in the nanoparticle and retards growth. This is often referred to as the Gibbs–Thomson effect[90–93], and results in a decrease in growth rate at small diameters. Furthermore, a reduction in supersaturation also increases the height of the nucleation barrier, as is described in the next section.

Another consequence of the extra energy associated with surfaces is a reduction in the melting temperature of nanoparticles compared to that of the bulk material[94]. The

following relationship describes the size-dependent melting temperature (T_M), in Kelvin:

$$T_M^{particle} = T_M^{bulk} - \left(\frac{4\gamma V_M}{\Delta S} \cdot \frac{1}{d}\right)$$

where ΔS is the difference in entropy of the liquid and solid phase, and since solids are more ordered than liquids, ΔS is a positive quantity. Again, since γ is positive, the melting point decreases with the inverse of the nanoparticle diameter. Significant effects have been observed and explained for small nanoparticles (< 5 nm)[94], but for larger nanoparticles, >20 nm, the melting point depression is often only a few Kelvin.

Nucleation

Nucleation is the initial step in forming a condensed (liquid or solid) phase. The nucleation rate (k) can be described according to classical nucleation theory by a simple Arrhenius expression[95]:

$$k \propto \exp -\frac{\Delta G^*}{k_b T}$$

where ΔG^* is the nucleation barrier, k_b the Boltzmann constant and T the absolute temperature. It is apparent that the rate of nucleation increases with increasing temperature and decreases with the height of the nucleation barrier. In this section, the properties that govern the height of the nucleation barrier for three-dimensional homo- and hetero-nucleation of a liquid phase are discussed. Similar mechanisms are valid for solid phases, but anisotropic surfaces must then be considered.

Cleaving a bulk crystal to form two new surfaces results in the formation of a new surface, associated with a surface energy. To a first approximation, the surface energy of a free surface is proportional to the density of dangling bonds, but neighboring atoms and the bond strength also influence[96]. When two different phases (α, β) form an interface, the excess energy of the two surfaces is known as the interfacial energy $(\gamma_{\alpha\beta})$. During nucleation, a small nucleus of a condensed phase forms, and interfaces with different surfaces energies and areas form between the nucleus and the surrounding phases.

3D nucleation

The Gibbs free energy of condensation (ΔG) describes the energy difference between the vapor and the condensed phase. Condensation from a supersaturated vapor corresponds to a decrease in chemical potential, which is reflected in the negative supersaturation-related volume term (ΔG_V). However, the new interfaces and surfaces that form are associated with a γ-related area term (ΔG_A). For a spherical nucleus the following expression can be constructed:

$$\Delta G = \Delta G_V + \Delta G_A = 4\pi r^2 \left(\frac{\Delta \mu}{3V_M} r + \gamma_{vn} \right)$$

where V_M is the mole volume of the nucleus, and γ_{vn} the interfacial energy between the vapor (v) and the nucleus (n). Note, that here $\Delta \mu$ is used as a negative quantity. Since ΔG increases with area but decreases with volume, ΔG can be maximized as a function of the nucleus radius (r).

At a critical radius (r^*), ΔG is maximized, and $\Delta G^* = \Delta G(r^*)$. Nuclei with $r < r^*$ are unstable and decompose, whereas nuclei with $r > r^*$ have overcome the nucleation barrier and continue to grow. Figure 3.3 shows a plot of ΔG and its constituents for the homonucleation of a 3D nucleus as a function of the nucleus volume, V.
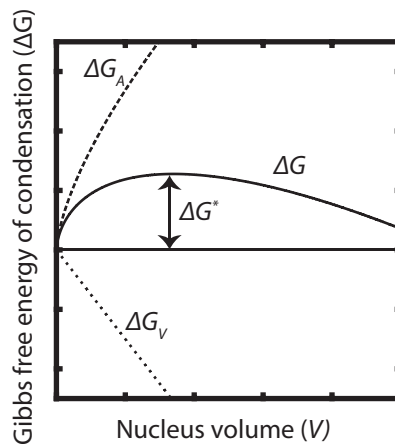
Figure 3.3. Schematic showing ΔG and its constituents for condensation to a spherical nucleus with the volume V.

For a simple spherical system, $\Delta G^*_{homonucleation}$ is given by the following expression.

$$\Delta G^*_{homonucleation} = \frac{16\pi V_M^2}{3} \frac{\gamma_{nv}^3}{(\Delta\mu)^2}$$

Nucleation on a surface

The origin of the nucleation barrier is the energy cost associated with forming surfaces (ΔG_A). Therefore, if the surface energies or the area can be reduced, the nucleation barrier will decrease. Nucleation on pre-existing surfaces is known as heteronucleation, which reduces the interface area to the supersaturated phase. Figure 3.4a shows a nucleus (n) on a pre-existing surface (s) surrounded by a vapor (v). If the interfacial energy of the nucleus and the pre-existing surface is lower than that between the nucleus and the supersaturated phase ($\gamma_{ns} < \gamma_{nv}$) this further reduces ΔG^* compared to homonucleation (Figure 3.4b).
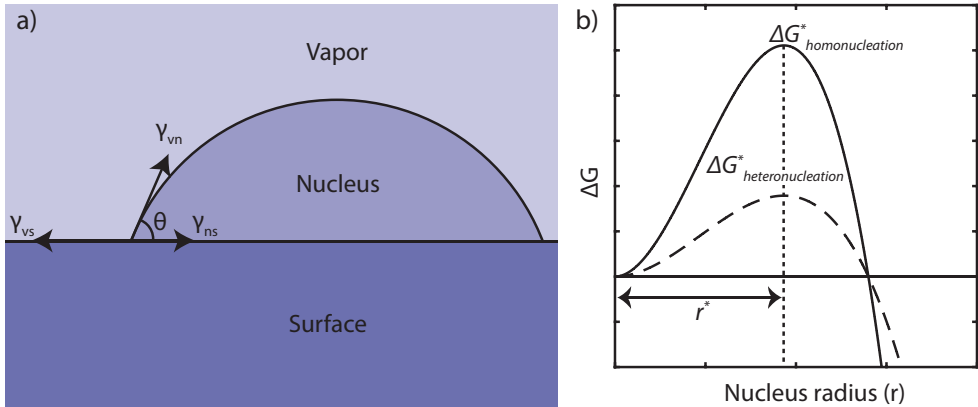
Figure 3.4. a) A nucleus on a surface surrounded by a vapor, balanced by the interfacial energies, which governs the wetting angle (θ). b) ΔG for homonucleation and heteronucleation with $\theta = 60°$.

The balance of the absolute interfacial energy between the three phases ($\gamma_{vs}, \gamma_{vn}, \gamma_{ns}$) determines the stable contact angle (θ) of the nucleus according to Young's relation:

$$\cos\theta = \frac{\gamma_{vs} - \gamma_{ns}}{\gamma_{vn}}$$

The shape of the spherical cap (droplet/nucleus) is controlled by θ, and defines the geometrical shape factor (f_{sphere}), which describes the fraction of the volume of a complete sphere.

$$f_{\text{sphere}} = \frac{2 - 3\cos\theta + \cos^3\theta}{4}$$

Finally, an expression for the heterogeneous nucleation barrier is obtained:

$$\Delta G^*_{heteronucleation} = \frac{16\pi V_M^2}{3} \cdot \frac{\gamma_{nv}^3}{(\Delta\mu)^2} f_{sphere}$$

where $\Delta G^*_{hetero} \leq \Delta G^*_{homo}$, since $f_{sphere} \leq 1$, especially when θ is close to zero or 180° and f_{sphere} approaches zero. Depending on the balance between interfacial energies, nucleation can thus be very beneficial on other surfaces.

4. Aerosol nanoparticles

An aerosol is a suspension of very small liquid or solid particles in a gas that can remain airborne from a few seconds to several years. This is due to the very low settling velocity of small particles, such as nanoparticles. For example, the settling velocity of 10 to 100 nm Au nanoparticles is 1 to 20 micrometer (µm) per second. The reason for this low settling velocity is the weak gravitational force compared to the drag force on light nanoparticles. The settling velocity of nanoparticles is reached almost instantaneously due to their low inertia.

Examples of aerosol nanoparticles include metal fumes, sea salt nuclei, oil smoke, diesel smoke and viruses in the atmosphere. However, they are usually short-lived since they collide and adhere to larger aerosol nanoparticles present in the ambient atmosphere. When transported in a high-purity carrier gas, there are much fewer collisions, and nanoparticles can follow the streamlines of the gas almost perfectly[89,97].

There are several methods of producing aerosol nanoparticles, in which the nano-particles are either created beforehand and then aerosolized, or are formed directly in the gas phase. In the present work, nanoparticles were produced directly in the gas phase by the condensation of evaporated metal species. The aerosol nanoparticles were generated with a SDG, which is part of a mobile aerosol production system available at our lab. The system can be used independently, or connected to other equipment such as an Aerotaxy reactor. In this chapter, the experimental setup, its capabilities, and the physics of the aerosol system are discussed.

Aerosol system

A schematic of the aerosol production system is shown in Figure 4.1. The default carrier gas is N_2, specified and confirmed to be $\geq$99.9999% pure, but other gases such as H_2 or pre-mixed gases can also be used. The carrier gas is controlled by mass-flow controllers, and transports the aerosol nanoparticles produced in the SDG (Figure 4.1a) through the system. The nanoparticles produced are charged with a known charge distribution using a radioactive ^{63}Ni source, and are then size-selected with two differential mobility analyzers (DMAs) and compacted in a tube furnace (Figure 4.1b). Finally, the nanoparticles are either collected in an electrometer for

nanoparticle concentration measurements, or in an electrostatic precipitator (ESP) for aerosol deposition (Figure 4.1c).
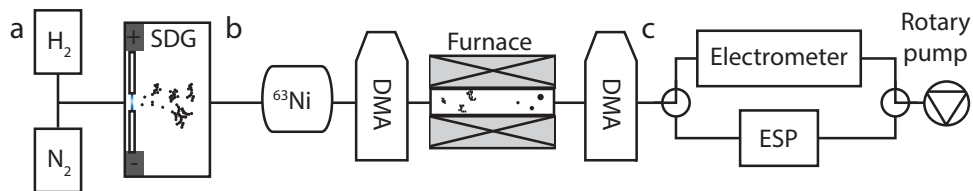
Figure 4.1. Illustration of the aerosol system. a) A carrier gas transports the aerosol generated by the SDG. b) Nanoparticles are bipolarly charged and size-selected with DMAs and compacted in a furnace. c) The nanoparticles are collected in an electrostatic precipitator (ESP) or electrometer, and the remaining flow exits through a rotary pump. The system has two-way and three-way valves (not all are shown) for bypassing parts of the system.

The system has a typical (size-selected) production rate of 10^4 to 10^6 cm^{-3} which, for the default flow rate of 1.7 standard liters per minute, corresponds to 10^5 to 10^8 nanoparticles per second. The number of nanoparticles produced by the SDG itself is orders of magnitudes higher, but there are significant losses in the aerosol generation system. Losses occur in the SDG chamber[98], ducts, and in the DMAs where only a fraction of the nanoparticles is selected to achieve a narrow size distribution. The system is mobile and highly versatile. The default configuration is shown here, but many of the parts can be bypassed, removed or added to suit the requirements

Generation of nanoparticles

The SDG was originally used to produce aerosols of monodisperse Au and C nano-particles[99,100]. However, the technology has since matured, and is now used to produce other materials[101–104] and is used in several scientific fields, for example, medicine and health[105], catalysis[106], and materials science[107]. Recent progress in increasing the production rate of SDG-generated nanoparticles includes the use of parallel sources[108], kHz spark frequencies[109,110], and more power-efficient continuous glow discharges[111,112]. In the future, the SDG may find its way into industrial applications, such as the textile industry[108] or photovoltaics through Aerotaxy[113]. A method related to spark discharge is the continuous arc-discharge method, which operates at much higher direct currents and lower voltages. A higher current is associated with a higher electrical power and production rate, but also with considerable heating of the electrodes and chamber[114].

Nanoparticle formation in spark discharges

During a spark discharge between two electrodes, material is ablated from the electrodes and a plasma channel forms, as shown in Figure 4.2. The plasma reaches temperatures of tens of thousands of Kelvin and the vapor is quenched to room temperature in < 100 μs[115]. With quenching rates on the order of 10^8 to 10^9 K/s[115] the supersaturation of the vapor increases rapidly, resulting in the nucleation and condensation of nanoparticles. The initial particle size is governed by the homogeneous nucleation barrier[116], but the nanoparticles grow due to continued condensation[117]. The nanoparticle size distribution can be tuned, for example, by the carrier flow rate, spark discharge frequency, or energy per spark[118,119]. Heat is released when nanoparticles collide and coalesce to form larger nanoparticles which, for high concentrations of nanoparticles, increases the average particle size and delays the onset of cluster formation[120].

Clusters of strongly bound, partially merged nanoparticles are referred to as aggregates[121], whereas weakly bound clusters (by van der Waals forces or surface tension) are referred to as agglomerates. Primary particles generated in a SDG are usually partially merged with each other, presumably due to the pure surfaces, which enable room temperature sintering[122], but the extent to which they are merged varies with the material system and system conditions. The terms aggregate, and agglomerate are often used interchangeably, and in this thesis the term aggregate will be used, whereas in Paper I, the same nanoparticle may be referred to as an agglomerate.
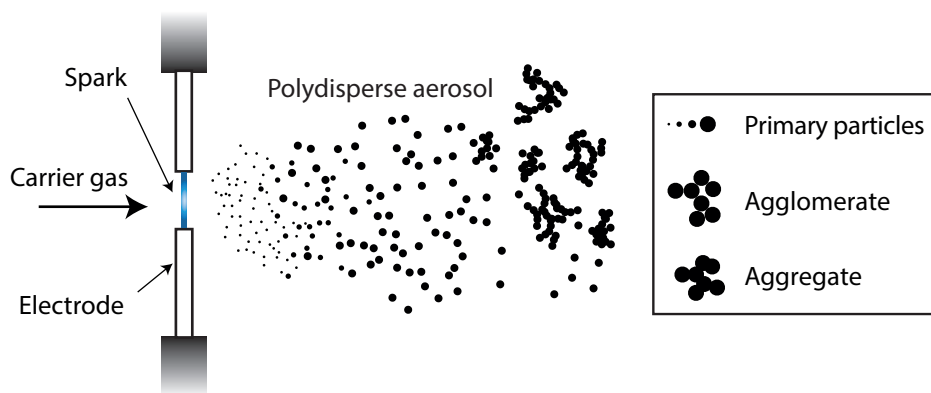
Figure 4.2. Schematic of particle formation in a SDG. The discharge evaporates material from the electrode surface to form a vapor. The vapor supersaturates when quenched in the carrier gas, and nanoparticles form and grow into spherical primary particles that form aggregates or agglomerates depending on bond strength.

Electrical discharge

The electrical system of the SDG consists of a high-voltage generator, a capacitor and two electrodes that constitute a simple high-voltage switch (Figure 4.3). A power supply charges the capacitor with a current (I) which gradually builds up a potential difference between the electrodes. Eventually, the difference in potential exceeds the breakdown voltage (U_b) of the gap between the electrodes and an electrical discharge occurs. According to Paschen's law, U_b is proportional to the gap distance and the gas pressure[123], but it is also affected by the electrode geometry and electrical properties of the carrier gas[98,124]. Under typical operation the capacitance is charged fast enough to slightly exceed U_b, and the observed discharge voltage (U_d) varies slightly between each discharge. The time taken to charge the capacitor to U_d defines the spark frequency (f_s):

$$f_s = \frac{I}{U_d C}$$

where C is the capacitance of the capacitor. The energy (E) stored in a capacitor is expressed as:

$$E = \frac{1}{2} C U_d^2$$

from which a fraction is used to form a spark and evaporate material.
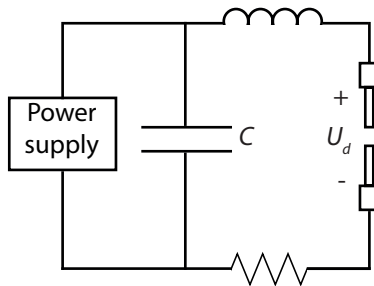
Figure 4.3. Electric circuit for a simple SDG. Adapted from (Meuller et al. 2012) [107]

Nanoparticle production rate

For evaporation to occur, it is necessary for the energy stored in the capacitor to be transformed into thermal energy capable of heating the electrodes and evaporating a volume of material. Therefore, nanoparticle formation is influenced by the material properties of the electrodes, namely: their heat capacity, boiling point, and evaporation enthalpy[125]. In addition, heat losses from conduction, convection, and radiation play an important role[125]. In general, the mass of evaporated material decreases with the heat capacity, evaporation enthalpy, and thermal conductivity of the electrode material. Therefore, metals such as Ag and W are much more spark resistant than metals such as Bi and Sb. Furthermore, the mass of material evaporated normally increases with the spark energy and frequency, since more energy is supplied[98].

Figure 4.4a) shows the nanoparticle concentration after size selection of Ag nanoparticles produced with currents of 4 and 32 mA. The measurements were performed with a DMA and an electrometer, from the electrical mobility diameter of the nanoparticles, as is explained later in this chapter. The nanoparticle distribution widens with increasing current, and shifts to more and larger nanoparticles, which is a clear sign of an increase in the mass of evaporated material. In Figure 4.4b, the Ag electrodes have been replaced with AgAu electrodes, which results in significantly more and larger nanoparticles at the same current and electrode distance. This is also interpreted as an increase in the mass of evaporated material.
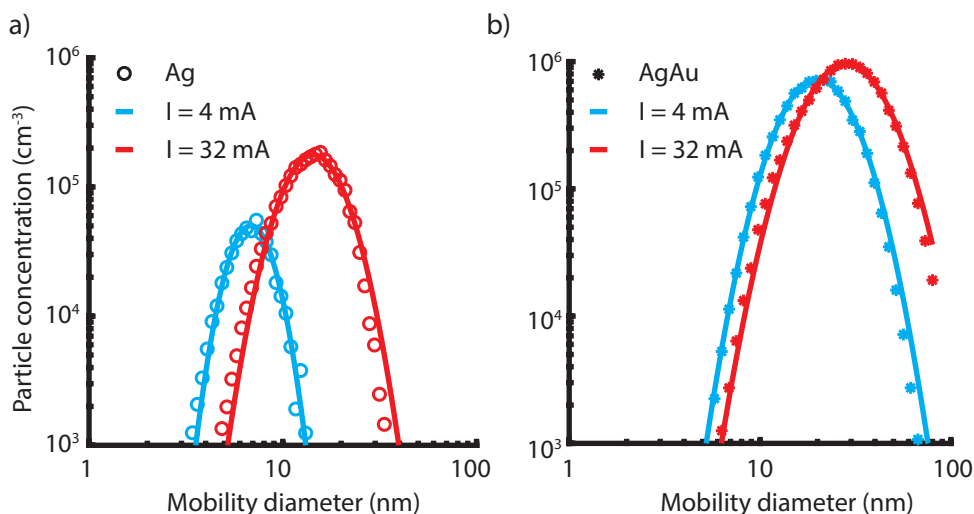
Figure 4.4. Nanoparticle concentration of size-selected a) Ag and b) AgAu nanoparticles sintered at 500 °C with a charging current of 4 and 32 mA. Data sets fitted to log-normal distributions.

With electron microscopy[126] or confocal laser scanning[104] micro-scale craters have been reported on the electrodes after a spark discharge. These craters are formed by individual spark events, due to the melting and re-solidification of small volumes of electrode material. It was also reported that most of the spark energy was spent in forming the craters, while only a small fraction was used to evaporate material. It is possible that the energy used in forming this pattern could explain the discrepancies observed between experiment and the Jones model[125].

Ag and Au have similar material properties and, according to the model developed by Jones[125], the mass of evaporated material from Ag and Au should be almost identical. However, discrepancies have been reported between the modelled electrode loss[125,127] and the measured electrode loss[98,112] for some material systems, especially for Au, which evaporates faster than expected. The model does not take liquid droplet ejection[128,129] or chemical reactions into consideration, and it has been speculated that this could affect the electrode loss by orders of magnitude[98,130]. Despite that the same capacitance and currents were used for the Ag and AgAu electrodes, the discharge voltage differs. This most definitely affects the spark energy, and may also explain the difference in production rate between the Ag and AgAu electrodes.

Processing of nanoparticles

After nanoparticle generation, all but the smallest nanoparticles form aggregates or agglomerates, and the particle size distribution is wide. The final nanoparticles should have a well-defined shape and narrow size distribution. The particle size is controlled in the aerosol system by electrically manipulating charged nanoparticles in an electric field with a DMA. The nanoparticles are sintered at elevated temperatures in a tube furnace to reshape them into compact nanoparticles.

Electrical mobility diameter

The nanoparticles are non-uniformly charged during generation, and a ^{63}Ni radioactive foil is used to generate bipolar ions that redistribute the electrical charges of the aerosol according to a Boltzmann distribution[131]. For nanoparticles with diameters in the range of 10 to 50 nm, more than 98% of the nanoparticles are either singly charged or uncharged, and multiple charges are rare (< 2%)[132,133].

A particle with n elementary charges (e) in an electric field (E) is subject to an electrostatic force (F_e).

$$F_e = neE$$

The particle terminal velocity (v_t) is limited by the aerodynamic drag force (F_d), which, for a spherical nanoparticle with diameter (d) is given by:

$$F_d = \frac{3\pi\mu v_t d}{C_C}$$

where μ is the dynamic gas viscosity and C_C the Cunningham slip correction factor. For nanoparticles it is important to correct for the discrete gas–particle interactions with C_C, which is unity for large particles but increases rapidly for particles on the nanometer scale. When v_t is reached (almost instantaneously for nanoparticles), the drag force and electrostatic forces are in balance and the electrical mobility of a particle (Z_p) is defined as:

$$Z_p = \frac{v_t}{E} = \frac{neC_C}{3\pi\mu} \cdot \frac{1}{d}$$

For singly charged spherical nanoparticles, d is equal to the aerodynamic diameter. However, for non-spherical nanoparticles the two differ, and the mobility diameter of two aggregates of the same volume will differ depending on their shape and orientation in the electric field. Note, that there is no dependence on mass.

Differential mobility analyzer

A DMA is commonly used in aerosol science for size selection of aerosol particles according to their electrical mobility. Nanoparticles of a specific size can be selected from a polydisperse flow of nanoparticles to provide a monodisperse flow, as shown in Figure 4.5a. A radial DMA consists of a grounded outer electrode and a central electrode, separated by a sheath gas (Q_{sheath}) flowing parallel to the electrodes. The central electrode is biased with respect to the outer electrode, forming a radial electric field perpendicular to the sheath flow. The nanoparticles enter the DMA with the carrier gas $(Q_{carrier})$, and follow the sheath gas, but drift due to the electric field. Depending on their Z_p, the nanoparticles will be collected by the central or outer electrode, or exit with the sheath gas or through the slit as size-selected nanoparticles (Figure 4.5b). The mean electrical mobility (Z_p^*) of the transferred nanoparticles is given by:

$$Z_p^* = \frac{Q_{sheath} \ln\left(\frac{r_{outer}}{r_{inner}}\right)}{2\pi L} \cdot \frac{1}{U}$$

and is inversely proportional to the applied voltage (U)[131]. Here, L is the distance traveled by the nanoparticles in the DMA, and r the outer and inner radius of the outer and inner electrodes. Increasing the applied voltage shifts the selection to larger nanoparticles, and reversing the applied bias between the central electrode and the outer electrode changes the selected nanoparticle polarity.
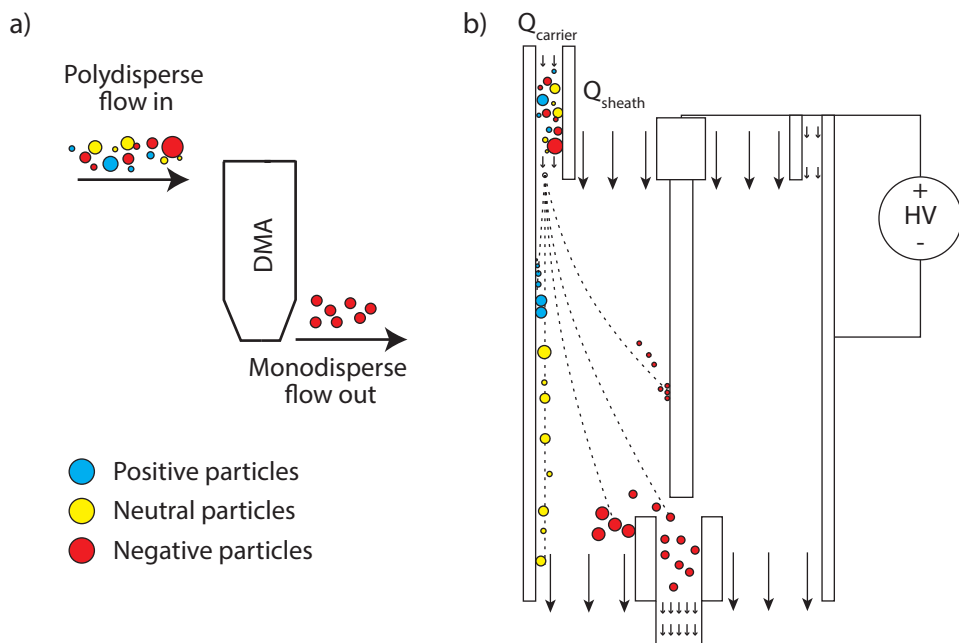
Figure 4.5. a) A DMA filters out a monodisperse flow of particles based on their size and charge. b) A positive high-voltage (HV) central electrode attracts negatively charged nanoparticles which drift in the sheath flow providing selection of nanoparticles with a specific Z_p.

The size-dependent nanoparticle concentration is measured in step mode, where the applied voltage is increased in small steps, and the nanoparticle concentration is measured for half a second 10 seconds after each step. The nanoparticle concentration is measured before the outlet of the system using an electrometer. An electrometer collects the charged nanoparticles and measures the dissipated current. The sensitivity of the aerosol electrometer used in this work (TSI 3068B) is 1 fA, and assuming the nanoparticles are singly charged this is equivalent to about 6250 nanoparticles per second. This electrometer thus provides an excellent means of measuring the nanoparticle concentration when using the SDG, which produces 10^5 to 10^8 size-selected nanoparticles per second.

The measurements can be carried out more quickly by ramping the voltage continuously, and deducing the size and concentration from the transient changes[134]. This was not done in the present work, but is common in commercial scanning mobility particle sizers, which consist of a particle charger, a DMA, and an electrometer.

The shape of the electrical mobility curve for nanoparticles transmitted by a DMA at a fixed voltage is triangular, and its full width at half maximum (FWHM) (ΔZ_p) is[134–136]

$$\Delta Z_p = Z_p^* \frac{Q_{carrier}}{Q_{sheath}}$$

A typical carrier-to-sheath flow ratio of 1.7:10 results in a ΔZ of 17% of Z^*. Due to the non-linear relationship between Z and d (from C_C), the corresponding change in Δd is narrower (for singly charged nanoparticles). For simplification, $2\Delta d$ is defined as $d(Z^* + \Delta Z) + d(Z^* - \Delta Z)$. For singly charged spherical nanoparticles, $\frac{\Delta d}{d^*}$ is approximately 8 to 9% for nanoparticles smaller than 50 nm, and 12 to 13% for doubly charged nanoparticles, as can be seen in Figure 4.6a. For larger particle diameters, C_C approaches unity, and $\frac{\Delta d}{d^*}$ approaches $\frac{\Delta Z}{Z^*}$. However, very large nanoparticles cannot be produced effectively with the SDG, and it is difficult to apply a specific electrical charge to larger nanoparticles. As the resolution is size-dependent, the absolute resolution increases with decreasing particle diameter, as shown in Figure 4.6b. However, eventually, Brownian diffusion in the DMA becomes significant (not considered here), which reduces the resolution, especially for smaller nanoparticles and longer DMA transit times.
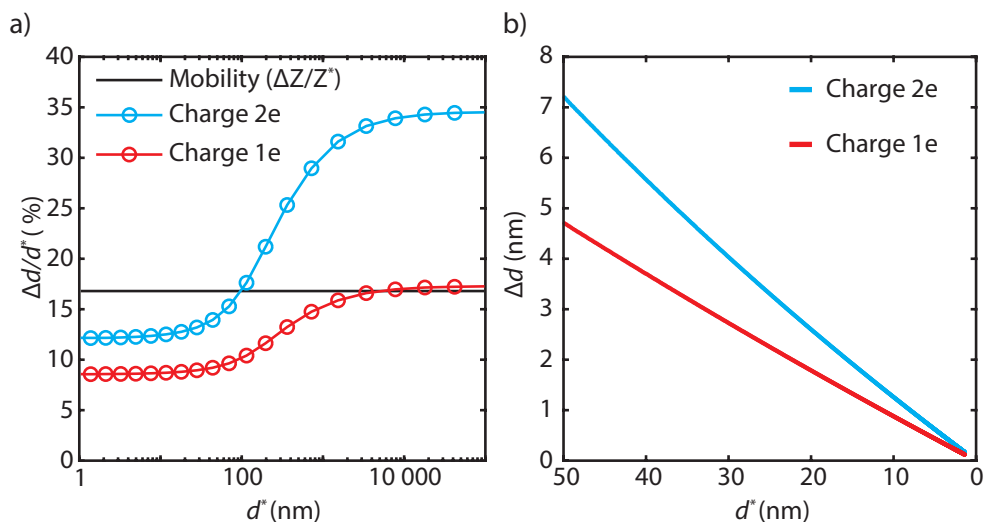
Figure 4.6. The transmitted FWHM for singly and doubly charged spherical nanoparticles, in relation to the selected diameter (d^*) shown as: a) relative resolution and b) absolute resolution.

Sintering to achieve thermal compaction

In nanoparticle applications, highly uniform and well-characterized nanoparticles are often preferred. To achieve this, it is necessary to compact the aggregates into well-defined compact nanoparticles, where the size and composition can be used to predict the particle properties.

When subjected to elevated temperatures, the solid-state diffusivity increases, and the primary particles may coalesce to form a more compact and more dense nanoparticle[137,138]. At higher diffusion rates, atoms rearrange and form more energetically favorable surfaces or phases. Diffusion can be divided into bulk, grain boundary, and surface diffusion; surface diffusion typically being the fastest[139]. Since an aggregate has a very high surface-to-volume ratio, surface effects are very important.

The compaction behavior of initially aggregated nanoparticles was studied with the tandem DMA setup shown previously in Figure 4.1. The first DMA is used to select a certain particle size, the tube furnace is set to the desired compaction temperature, and the second DMA is used to analyze the final particle diameter. When unsintered Au nanoparticles were size-selected in the first DMA and transported through the tube furnace at room temperature, they were found to be approximately 52 nm in diameter using the second DMA (the blue peak in Figure 4.7a). When the tube furnace was set to 500 °C the particle diameter was only 31 nm, indicating considerable compaction (the green peak in Figure 4.7a).
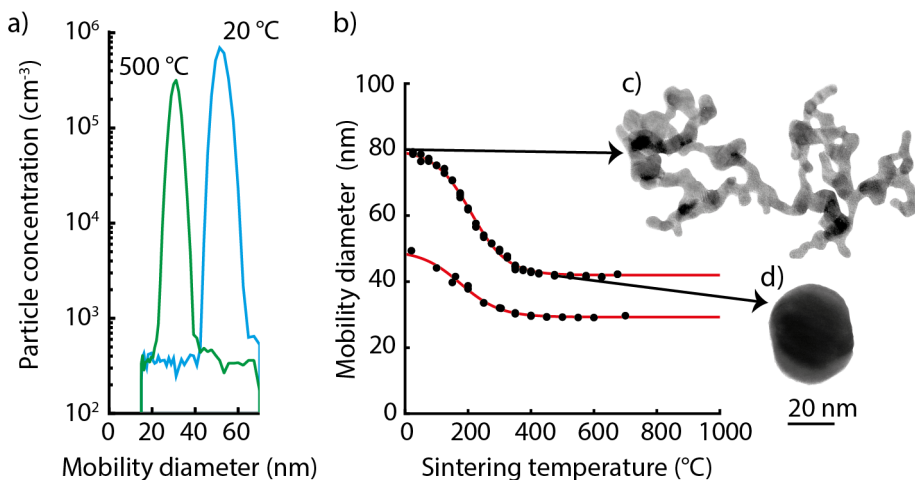
Figure 4.7. The mobility diameter of Au nanoparticles: a) unsintered (blue) and sintered at 500 °C (green). b) The nanoparticle mode as a function of furnace temperature shows gradual shrinkage. TEM of c) unsintered nanoparticle and d) nanoparticle sintered at 500 °C.

The mode of the nanoparticle distribution is the most common particle size of the distribution and corresponds to the peak positions in Figure 4.7a. A plot of the mode as a function of furnace temperature is referred to as a sintering scan, and reveals information on the degree of compaction of the nanoparticles. Sintering scans for 50 and 80 nm Au nanoparticles are shown in Figure 4.7b as an example. Complete compaction occurred at about 400 °C for 50 nm aggregates, and at about 500 °C for 80 nm aggregates. The compaction of the aggregates was confirmed using TEM (Figure 4.7b). At high temperatures (> 600 °C) thermal charging may occur leading to multiply charged nanoparticles, due to thermionic emission of electrons or positive ions[140].

Three steps can usually be identified when studying the temperature-dependent compaction of aerosol nanoparticles: compaction, internal rearrangement and evaporation[141]. At low temperatures the nanoparticles become more compact with increasing temperature. The compaction temperature (T_C) refers to the lowest temperature that results in completely compact nanoparticles, as is apparent from a plateau with a constant mobility diameter in a sintering scan. Complete compaction is usually achieved when nanoparticles are sintered at a temperature of around 30 to 60% of the bulk melting temperature (T_M) (in Kelvin)[142].

Figure 4.8 shows the compaction behavior of six elements: Co, Rh, Pd, Sn, Pb, and Bi. The metals with high melting points: Co, Rh, and Pd, show similar compaction behavior to Au, i.e., gradual compaction at low temperatures, and $T_C < T_M$. The low-melting-point metals, Sn, Pb, and Bi, on the other hand, exhibit a more complex

compaction behavior and $T_C > T_M$. This could be due to contamination, or partial oxidation of the metals during generation or in the tube furnace. To prevent oxidation, Bi, Co, and Sn nanoparticles were therefore generated in N_2 containing 5% H_2, instead of pure N_2 (as discussed in a later section).
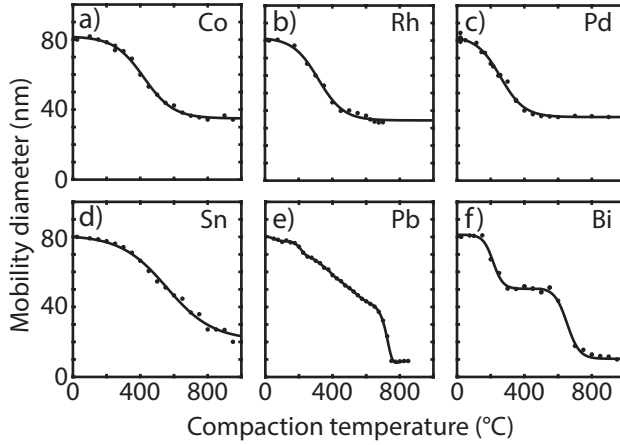
Figure 4.8. Compaction behavior of 80 nm aggregates of six different metals as a function of compaction temperature: To prevent oxidation, Co, Sn, and Bi were generated in a mixture of N_2 and H_2.

Evaporation

The lifetime of a liquid particle can be calculated from its evaporation rate[143,144]. The following differential equation describes how the particle diameter (d_p) changes over time[145].

$$\frac{d(d_p)}{dt} = \frac{4D_v M}{R\rho_p d_p}\left(\frac{p_\infty}{T_\infty} - \frac{p_s}{T_s}\right) \cdot \frac{2\lambda_{gas} + d_p}{d_p + 5.33\frac{\lambda_{gas}^2}{d_p} + 3.42\lambda_{gas}}$$

The partial pressure of the metal far from the particle in the sintering furnace (p_∞) should be much smaller than the vapor pressure at the droplet surface (p_s), and the expression can be simplified to:

$$\frac{d(d_p)}{dt} \approx -\frac{4D_v M}{R\rho_p d_p}\frac{p_s}{T_s} \cdot \frac{2\lambda_{gas} + d_p}{d_p + 5.33\frac{\lambda_{gas}^2}{d_p} + 3.42\lambda_{gas}}$$

The factor $\frac{D_v M p_s}{\rho_p}$ differs between metals, but p_s typically differs by several orders of magnitude between metals at the same temperature. The remaining factors are: the diffusion coefficient of the vapor (D_v), temperature at the particle surface (T_s), the molecular mass of the metal (M), the density of the liquid metal (ρ_p) and the mean free path of the gas (λ_{gas}) [121].

Figure 4.9a shows the vapor pressures of Bi, Pb, Sn, and Au extrapolated from reference data[146]. Figure 4.9b shows the evaporation rates of 50 nm nanoparticles of Bi, Pb, Sn, and Au estimated using the above expression. At the same temperature, the vapor pressures of Bi and Pb are orders of magnitude higher than those of Sn and Au, and they can thus be expected to evaporate at lower temperatures. The modelled evaporation rate of Bi and Pb exceeds 1 nm/s already at 400 to 600 °C, whereas Sn and Au require temperatures of 800 to 1000 °C to reach similar rates. These differences are expected from their differences in vapor pressure (Figure 4.9a).
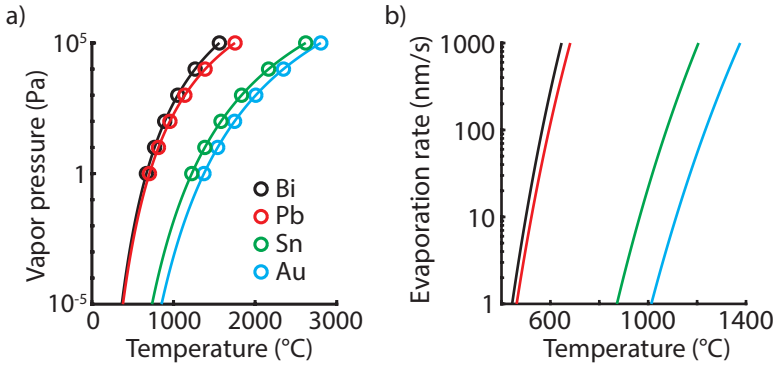
Figure 4.9. a) Extrapolated vapor pressure of liquid Bi, Pb, Sn, and Au[146] b) Theoretical evaporation rate of 50 nm nanoparticles of Bi, Pb, Sn and Au.

Numerical solution of the differential equation allows the evaporation of a Bi nanoparticle to be visualized, as is illustrated in Figure 4.10a at three temperatures: 500, 550, and 600 °C. The total time was set to one second, which resembles the time an aerosol nanoparticle spends in the compaction furnace. The particle diameter was modelled as a function of time by calculating p_d and $\frac{\Delta(d_p)}{\Delta t}$ iteratively with µs time steps (Δt). Note, that due to the Kelvin effect, p_d increases exponentially with decreasing particle diameter, resulting in a significant increase in evaporation rate for the smallest nanoparticles. This is particularly clear for < 5 nm nanoparticles, which yield an almost vertical slope in Figure 4.10a. Some evaporation can be expected during the compaction of Bi nanoparticles if they are heated to high temperatures. This was also confirmed in the present work (Paper I) (Figure 4.10b and c), where Bi

nanoparticles generated in N_2 with 5% H_2 were compacted from 80 nm aggregates to 50 nm nanoparticles, and finally shrank (due to evaporation) at temperatures around 600 °C. Even this simple model is sufficient to give an idea of the temperature range in which evaporation can become a problem. Similar measurements were made for Sn, which instead evaporated at around 900 °C.
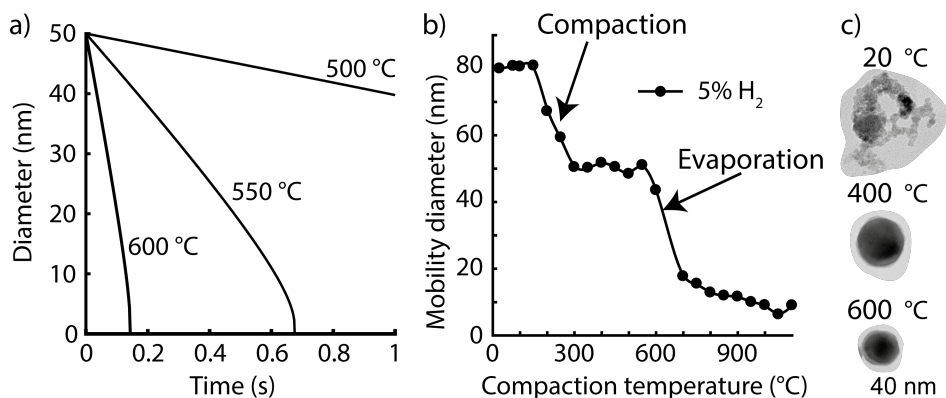
Figure 4.10. a) Modelled particle diameter time-dependent evaporation of 50 nm Bi nanoparticles at three temperatures. b) Compaction behavior of Bi nanoparticles generated in 95% N_2 and 5% H_2. c) TEM images of typical Bi nanoparticles sintered at different temperatures.

Collection of nanoparticles

Electrostatic precipitation is a convenient method for depositing nanoparticles on flat non-insulating substrates. If the substrates are not flat, the nanoparticle concentration will be inhomogeneous, and charge may build up on insulating substrates, which will complicate deposition.

Electrostatic precipitator

The aerosol enters the ESP from above, and perpendicular to the substrate. The aerosol then expands, and the flow rate decreases. Without an applied bias, the aerosol will reach the center of the ESP plate and spread out as it flows around the plate on its way to the outlet located below. When a bias is applied, the aerosol is collected in a region with an even nanoparticle density[147,148]. This region is often referred to as the deposition spot, and is elongated towards the direction of the outlet, as shown in Figure 4.11b. Note, that for nanoparticle depositions used for nanowire growth

described in in Papers II and III, the nanoparticle density is rather low (1 to 10 μm^{-2}) and the deposition spot is almost invisible for the naked eye.
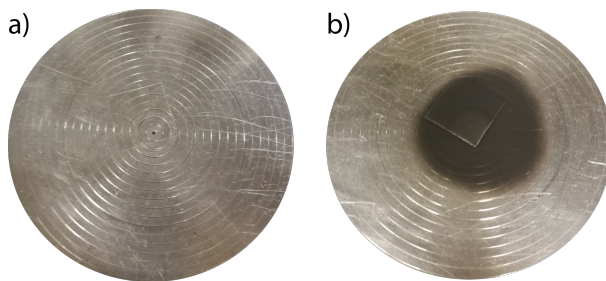
Figure 4.11. a) Photograph of the ESP plate: a) before and b) after extremely high-density nanoparticle deposition to visualize the deposition spot.

Small nanoparticles have a high electrical mobility; thus, they reach a high terminal velocity in the electric field and are collected in a smaller area than large nanoparticles. Decreasing the applied bias or increasing the distance between the metal plate and the ESP inlet increases the deposition area. The deposited nanoparticle density is estimated from the carrier gas flow, nanoparticle concentration, deposition area, and deposition time.

Nanoparticle density and diameter

The nanoparticles are accelerated by an electrostatic force and are deposited onto a substrate. Since the electric field strength is stronger at sharp curvatures, the nanoparticle density will be much higher at the edges of the substrate. For example, the nanoparticle density at the edge of the substrate is around four times higher than near the center (see Figure 4.12a and b). The average nanoparticle density at the center is 1 ± 0.1 μm^{-2} (calculated from three different measurement areas) and the average particle diameter is 34 ± 4 nm (based on 833 nanoparticles). However, the nanoparticle distribution is bi-modal, with a major peak at 33 ± 2 nm, representing singly charged nanoparticles, and a minor peak at 44 ± 6 nm, corresponding to doubly charged nanoparticles with the same mobility[149]. Note, that the resolution is well described by the DMA transfer function if the bi-modality is considered.
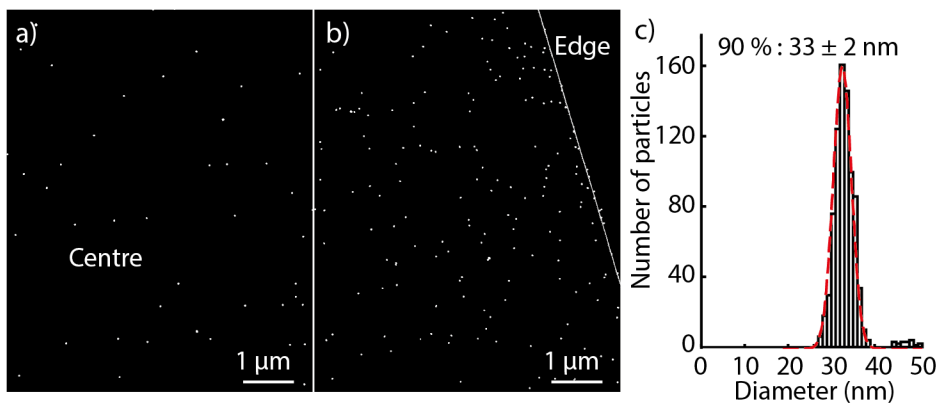
Figure 4.12. Contrast-enhanced SEM images of Au nanoparticles deposited on GaAs substrates: a) at the center and b) at the substrate edge). The nanoparticle density is uniform in the center and higher at the edges. c) Statistical analysis of the particle size distribution shows that 90% of the nanoparticles agree with a Gaussian distribution centered at 33 nm, with a FWHM of 2 nm.

The fraction of multiply charged nanoparticles is lower for the deposition of smaller nanoparticles. In addition, Δd is roughly 9% of the selected diameter, and becomes very small for small nanoparticles. For example, the standard deviation for 12 nm nanoparticles was measured with SEM and found to be ± 1 nm.

Composition of nanoparticles

A wide variety of metals[99], alloys[98,150–153], semiconductors[154], and metal oxides[155] have been produced with SDGs. In the present work, there was a need to produce pure unoxidized metal nanoparticles, and to enable the use of alloys. To produce unoxidized metal nanoparticles it is necessary that the O_2 concentration in the aerosol system is lower than the dissociation pressure of the metal oxide. However, the dissociation pressure of many metal oxides is far below ppb levels of O_2. Therefore, it is not surprising that easily oxidized metals are partially or completely oxidized during particle formation, and are further oxidized during sintering[156]. Some of the results from Paper I are highlighted in the following section, before this chapter is concluded with a discussion on the production of alloy nanoparticles.

Preventing oxidation of nanoparticles

Metal oxides typically have a higher melting point and lower solid-state diffusivity than the pure metals. Therefore, oxidized nanoparticles require higher sintering temperatures to become completely compacted. Oxidation can be prevented by decreasing the O_2 levels in the system, e.g., by prolonged nanoparticle production to scavenge the remaining O_2[154], or by adding a reducing agent such as H_2. The addition of a low concentration of H_2 prior to sintering enables the reduction of many metal oxides, since H_2 reduces the oxide to form water[157–159].

The compaction behavior and composition of Au, Bi, Sn, and Co nanoparticles were studied for nanoparticles generated in either N_2 (99.9999% pure) or a mixture of 95% N_2 and 5% H_2. The compaction behavior was also compared to that of nanoparticles generated in pure N_2, but sintered in a N_2/H_2 mixture. The compaction behavior of 80 nm Bi aggregates generated in the two atmospheres is shown in Figure 4.13a.
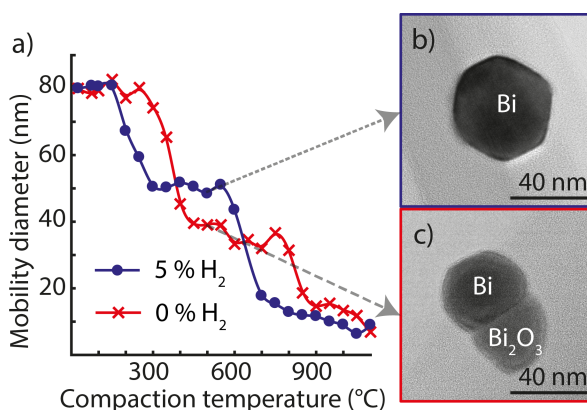
Figure 4.13. a) Compaction behavior of Bi nanoparticles generated in pure N_2 carrier gas (99.9999%), and 95% N_2 + 5% H_2. TEM images are shown of nanoparticles compacted at 500 °C generated in b) the N_2/H_2 mixture, and in c) pure N_2.

The nanoparticles generated in N_2 were initially resistant to compaction, but showed significant compaction, from 80 to 40 nm, between 300 and 450 °C. In contrast, the nanoparticles generated in the N_2/H_2 mixture compacted from 80 to 50 nm between 150 and 300 °C. These trends, together with the subsequent evaporation at higher temperatures can be seen in Figure 4.13a). The morphology of the compacted nanoparticles also clearly differs; the nanoparticles generated in the N_2/H_2 mixture being compact and faceted (Figure 4.13b), while the nanoparticles generated in N_2 consisted of both the metal and the oxide (Figure 4.13c). Similar phase separations were visible at other compaction temperatures, and at 500 °C the darker region was

identified as Bi, and the brighter region as Bi_2O_3. At 400 °C, the nanoparticles generated in the N_2/H_2 mixture exhibited only the darker Bi phase. Phase identification was based on the identification of crystal structures in a few selected nanoparticles, complemented with XEDS quantification of many nanoparticles (further details are given in Paper I). Finally, X-ray diffraction studies of high-density nanoparticle depositions confirmed that the nanoparticles generated in the N_2/H_2 mixture consisted almost entirely of Bi, whereas the nanoparticles generated in N_2 also contained Bi_2O_3. In addition, traces of Bi_2O_3 was detected in nanoparticles generated in the N_2/H_2 mixture, and was attributed to the formation of an oxide layer after deposition, which was found to grow slowly over time.

Simply adding H_2 prior to sintering was found to be less effictive than adding it at generation, as was demonstrated by repeated mobility diameter scans at a sintering temperature of 500 °C (Figure 4.14a). The mobility diameter did not change significantly when H_2 was added prior to sintering, but remained centered around 40 nm. Furthermore, the nanoparticle morphology was very similar to that of nanoparticles generated and sintered in N_2 (Figure 4.14b). Based on the identical size and morphology, the nanoparticle composition is very likely the same, consisting of Bi and Bi_2O_3. However, when H_2 was added during generation, a clear change in the mobility diameter was observed when the H_2 flow was turned on and off. The compaction of the nanoparticles showed a clear change in mobility diameter when H_2 was present during generation.
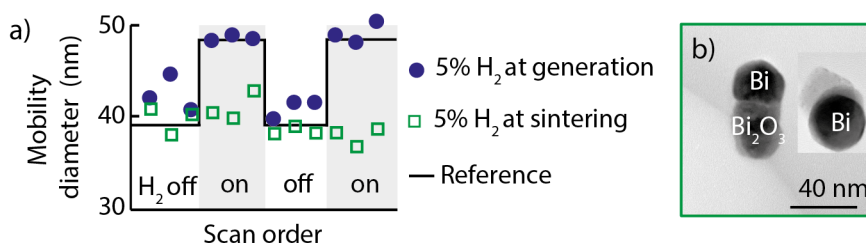
Figure 4.14. a) Mobility diameter for 12 repeated sintering scans at 500 °C when H_2 was introduced during generation (blue) or prior to sintering (green), and b) TEM images of nanoparticles sintered in the N_2/H_2 mixture.

Alloyed nanoparticles

There are three major pathways for atomic mixing in spark-discharge-generated nanoparticles[112]: the use of different electrodes, homogeneous electrodes, or heterogeneous alloy electrodes (Figure 4.15a-c). In a homogeneous alloy, atoms of different elements are distributed uniformly, whereas in a heterogeneous alloy there are phases of different composition[160]. The simplest way to produce alloy nanoparticles is to use two different electrodes, but typically results in nanoparticles with mixed compositions, (Figure 4.15a) The nanoparticle composition would have to be optimized using the process parameters[152,161]. Alloy electrodes offers a more stable means of producing a homogeneous distribution of alloy nanoparticles[98], assuming the electrode composition is homogeneous on the size scale of the ablated volumes (Figure 4.16b). This is especially true for immiscible metals associated with heterogeneous alloys, where the homogeneity is limited by the crystallite size. One method of creating fine heterogeneous alloys is to mix and sinter powders[162].
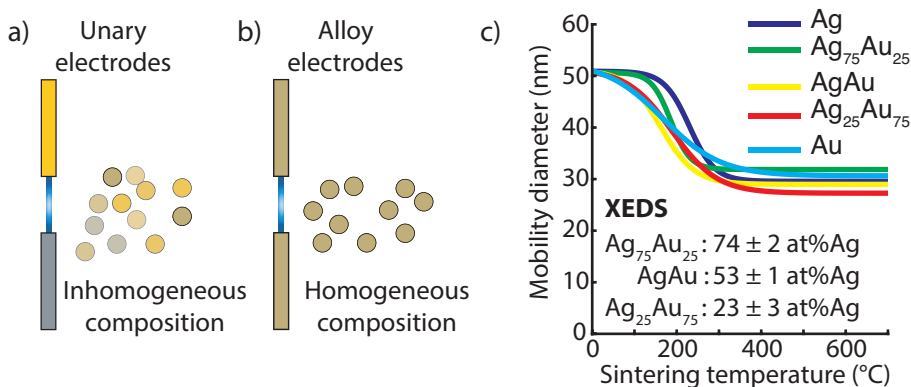
Figure 4.15. Schematic of alloy metal nanoparticles created from: a) different unary metal electrodes, or b) alloy electrodes. c) Compaction behavior and average Ag content determined with XEDS of nanoparticles generated from pure metal (Ag and Au) and alloy electrodes.

In many applications it is not sufficient to simply form alloy nanoparticles; the homo-geneity of the nanoparticle composition, and the size and shape must also be controlled. A brief study was carried out on the compaction behavior of AgAu alloy nanoparticles with different compositions (Figure 4.16c). Differences were seen in both the on-set of compaction and the compaction temperature, but the final particle diameter remained similar (30 ± 2 nm). Nanoparticles from electrodes with ≥50 atomic percent (at%) Au started to compact already at room temperature, whereas the more Ag-rich alloys did not start to compact until above 100 °C. Both room temperature sintering of Au[149] and the later on-set of compaction for Ag[137,163] have been observed previously.

To verify that the composition is indeed homogeneous between nanoparticles, and that no clear ordering or segregation occurs in the nanoparticles, the composition was analyzed using XEDS in combination with TEM. Both Ag and Au are fcc-structures with similar lattice constants, a_{Ag}= 4.09 Å and a_{Au} = 4.07 Å, therefore, crystal structure identification is not the best method to determine the composition of the nanoparticles. However, the XEDS spectrum from Ag differs significantly from that of Au and can be used for quantification. Quantification using XEDS showed close agreement between the specified electrode composition and the average nanoparticle composition (Figure 4.16d). The relatively small spread (standard deviation ≤3 at% Ag), confirms that the nanoparticles produced had a similar composition. No clear segregation was observed within the nanoparticles, but this may occur due to differences, for example, in the heat of sublimation, affinity of gases, surface energy, melting point, and strain energy[164]. These are important effects, that must be considered, and could possibly be exploited, in the engineering of alloy nanoparticles.

5. Particle-assisted growth of III–V nanowires

Overview of particle-assisted growth

A simple schematic of PAG and vapor-solid (VS) growth for GaAs and InAs nanowire growth is shown in Figure 5.1. The metal nanoparticle and the group III species form an alloy, causing the nanoparticle to grow and reshape. The solubility of group V species (such as As and P) is typically very low in the seed metal, and thus an intake of group V species incurs a negligible volumetric change. When critically supersaturated, nanowire material nucleates and a bilayer (a layer of III–V dumbbells) precipitates at the nanowire–substrate interface. III–V material is continuously supplied and spent during nanowire growth, by direct impingement of group III and V species on the nanoparticle, as well as through surface diffusion of group III species. VS growth will also take place directly on the substrate and nanowire side-facets, but is typically much slower than the particle assisted growth, resulting in structures with a high aspect ratio.
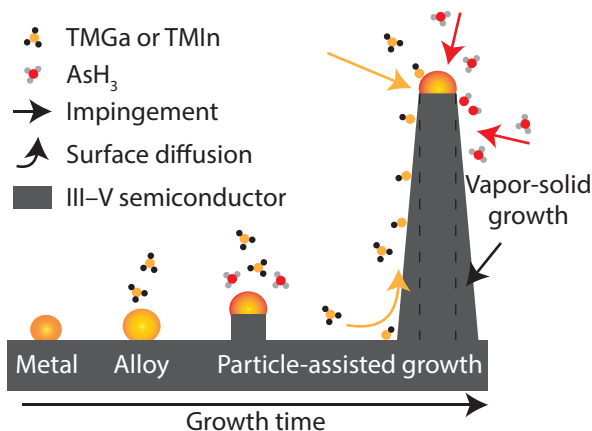
Figure 5.1. Schematic of particle-assisted growth. A metal nanoparticle alloys with the group III species, supersaturates, and precipitates the III–V material.

Thermodynamic driving force

The thermodynamic driving force for crystallization is the chemical potential difference of the vapor phase and the solid phase, as was discussed in Chapter 2. However, in MOCVD and Aerotaxy, the group III and V elements are not directly supplied as a vapor, but are formed indirectly from the decomposition of precursors. The chemical potential difference is huge, and decomposition is non-reversible,

$$u_{precursor} \gg u_{vapor}$$

In PAG, the particle acts as an intermediate phase between the vapor and crystal phase, and the following inequality can be constructed:

$$u_{precursor} \gg u_{vapor} > u_{particle} > u_{crystal}$$

This inequality states that for PAG to occur, the nanowire should be stable with respect to the particle and vapor. A broken inequality would imply a scenario where there is no thermodynamic driving force to supply the particle and nanowire with more material. In such a case, the seed particle may etch the nanowire, or the nanowire may simply decompose. This may occur, for instance, when the nanoparticles and substrate are annealed, or when the precursor supply is turned off to terminate growth.

Rate-limiting steps

Nanowire growth can be regarded as a chemical reaction in which reactants such as trimethylgallium (TMGa) and arsine (AsH$_3$) form the product GaAs through a sequence of reaction steps. Since these steps are sequential, the reaction is limited by the slowest, or rate-limiting step. To understand what governs nanowire growth, and what limits its growth rate, it is useful to consider the steps required for nanowire growth.

The early works by Givargizov[90,165] highlight four rate-limiting steps in the PAG of Si from liquid nanoparticles: 1) mass transport through the gas phase, 2) chemical reaction at the vapor–liquid interface, 3) diffusion in the liquid phase, and 4) incorporation of the material in a crystal lattice. In the present work, liquid and solid nanoparticles were used to grow III–V nanowires, and it is thus important to note the following:

- the rate of diffusion of solids is usually lower than for liquids due to their lower diffusivity, and

- Si is mainly supplied by impingement, whereas group III elements (In and Ga) can also be supplied by surface diffusion.

Bearing in mind the two points above, Givargizov's steps can be modified to five steps: 1) mass transport through the boundary layer, 2) precursor decomposition, 3) surface diffusion, 4) diffusion in the liquid or solid nanoparticle, and 5) nucleation.

In the following sections, the above steps from precursor to nanowire are described to provide the reader with an introduction to the processes that govern nanowire growth. Mainly MOVPE is described, but this method has much in common with Aerotaxy, since metal organic (MO) precursors are also used. More information can be found in excellent reviews of PAG using liquid[166–169] and solid[170] seeds, and on works describing theoretical models of nanowire growth[168,171–176].

Mass transport through the boundary layer

Precursors are transported in a carrier gas by an imposed pressure gradient between the precursor source and the reactor. The exact flow dynamics in a typical MOCVD or Aerotaxy reactor are complex, and only a few fundamentals are introduced here. Considerable hydrodynamic theory is required for a more complete description[177].

In a vertical MOCVD reactor the carrier gas arrives perpendicular to the sample, and spreads homogeneously around it, before flowing towards the outlet, as in the case of the aerosol in a turned-off ESP described in Chapter 4. The gas slows down near the sample due to viscous forces, and a stagnant boundary layer forms, through which mass transport only occurs through diffusion. The susceptor (on which the sample lies) is rotated at 30 rpm during growth, to improve the uniformity and reduce the boundary layer thickness, δ_0.

$$\delta_0 \cong 4 \left(\frac{\mu}{\rho \omega} \right)^{\frac{1}{2}}.$$

Here, ρ is the density of the gas, and ω the angular rotation rate of the susceptor. The diffusion flux (J) of a precursor such as Ga through the boundary layer is described by the equation below:

$$J = \frac{D_{Ga}(p_{Ga}^* - p_{Ga}^c)}{RT\delta_0}$$

where D_{Ga} is the diffusivity of Ga species, and p_{Ga}^* and p_{Ga}^i are the partial pressures of Ga species in the carrier gas ($*$) and at the crystal (c). When crystal growth is limited by mass transport through the boundary layer, J is also proportional to the crystal growth rate. However, nanowire growth rarely takes place at high enough temperatures for mass transport through the boundary layer to be rate-limiting.

Figure 5.2 illustrates the desorption, mass transport, and reaction-limited regimes of 2D crystal growth. In general, reactions tend to dominate the overall growth rate at low temperatures, which is where nanowire growth typically occurs, and there is a strong temperature dependence. At intermediate temperatures, the reactions are no longer kinetically hindered, and mass transport then limits the growth. At very high temperatures, the vapor pressure of the material is high enough for the net desorption of material.
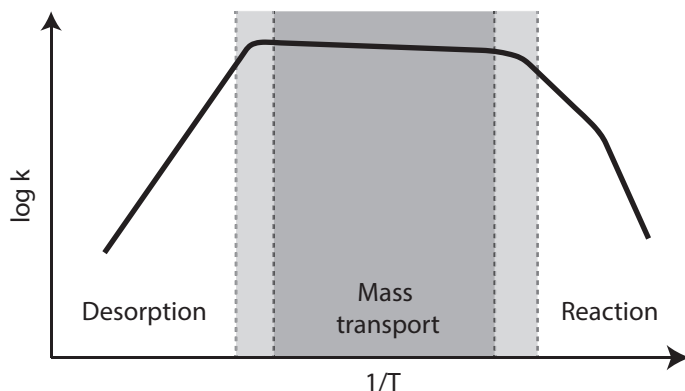
Figure 5.2. Schematic of logarithmic growth rate versus inverse temperature showing the three common regimes of 2D MOVPE growth. Nanowire growth typically takes place in the reaction-limited regime, where precursor decomposition is incomplete, and nucleation barriers are significant. Adapted from (Pohl 2013)[178].

Precursor decomposition

It is not sufficient to simply supply the precursors, but they must also decompose into free group III and group V atoms that can be incorporated into the semiconductor. Precursor decomposition due to heating is known as pyrolysis, which originates from the Greek words *pyro* meaning fire and *lysis* meaning separating. The precursors used in the present work were TMIn, TMGa, and AsH_3, which are group III and V atoms bound by ligand methyl radicals or H atoms.

Studies on GaAs growth in MOCVD have shown that TMGa and AsH_3 start to de-compose at 325 °C, and are fully decomposed at 480 °C and 525 °C, respectively[179].

However, both precursors fully decompose at temperatures below 450 °C when a gas mixture containing both TMGa and AsH₃ is supplied[180]. Precursor decomposition is therefore affected by the relative supply of the group III and V precursors, or the V/III ratio. Similarly, early Aerotaxy experiments showed that the decomposition of AsH₃ starts at around 200 °C in the presence of Ga nanoparticles[181]. TMIn decomposes at lower temperatures than TMGa, beginning at 250 °C, and is fully decomposed at about 400 °C[182].

The precursor decomposition rate is often much higher at III–V surfaces[183] and at a Au seed particle[184–186] than in the gas phase. In fact, catalyzed precursor decomposition was initially suggested to be the main reason for the high nanowire growth rates from liquid Au nanoparticles[187]. However, increased decomposition cannot be the sole reason why nanowires grow, as PAG would then not work in non-chemical vapor deposition (CVD) techniques such as molecular beam epitaxy (MBE)[188] and chemical beam epitaxy[189], which take place under high vacuum.

Surface diffusion

Surface diffusion is an important transport mechanism in the PAG of III–V nanowires[189]. A solid surface in contact with a vapor is constantly being bombarded with molecules of the vapor. A fraction of the impinging molecules will be adsorbed onto the surface either weakly (physisorption) or strongly (chemisorption). An adsorbate may be a partially or fully decomposed precursor which contributes to growth if it reaches a suitable nucleation site before it desorbs, but can also be a non-growth species, such as H₂. Surface diffusion is an activated process and follows a simple Arrhenius relation:

$$D \;=\; D_0 \exp -\frac{E_{diff}}{kT}$$

where D is the diffusion coefficient, D_0 an exponential pre-factor, and E_{diff} the activation energy for diffusion. When the thermal energy (kT) is high, an adsorbate may overcome E_{diff} and diffuse in Brownian (random) motion along the surface, which increases its diffusion length (λ). However, with increasing temperature, also the rate of desorption increases, which limits the diffusion length[190].

For example, As species desorb very rapidly and λ_{As} is often regarded as being negligible compared with λ_{Ga} and λ_{In}, which may be several μm[168]. Therefore, λ is a critical parameter that greatly affects the supply of material to the nanoparticle, and can be expressed as in the following equation:

$$\lambda = \lambda_0 \exp \frac{E_{des} - E_{diff}}{2kT}$$

Where λ_0 is the effective elementary jump distance, and E_{des} the activation energy for desorption. In general, $E_{des} \gg E_{diff}$, hence, λ increases at low temperature, until the thermal energy allows significant desorption. Similar to the 2D growth rate regimes presented previously in Figure 5.2, this results in a desorption and a burial regime for λ (Figure 5.3a).
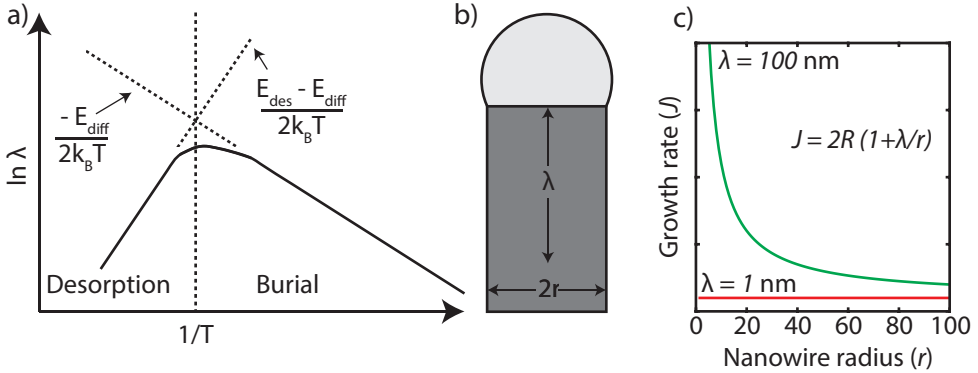
Figure 5.3. a) The diffusion length (λ) of an adsorbate is limited by desorption at high temperatures and by burial at low temperatures. Adapted from (Smith 1995)[191]. b) Schematic of a nanowire that is longer than the diffusion length.. c) If nanowire growth is limited by surface diffusion, the growth rate (J) is dependent on λ/r. Note: the Gibbs–Thomson effect and VS growth have been excluded.

In nanowire growth using MOCVD, a considerable proportion of the group III supply may originate from surface diffusion[171,189,192]. The area within a diffusion length of the seed particle is known as its collection area, and may differ between nanowires of different height or width. A wider nanowire has a smaller collection area (in comparison to the growth interface) than a thin nanowire. Therefore, when the nanowire growth rate is limited by surface diffusion, a thin nanowire will grow faster than a thick nanowire[171,192] (Figure 5.3c). The surface-diffusion-limited growth rate (J) of a nanowire that is longer than λ (Figure 5.3b and c), from a hemispherical nanoparticle with radius r is described by:

$$J = 2R \left(1 + \frac{\lambda}{r} \right)$$

where R is the arrival rate of growth species per unit area, and the equation is governed by the geometric relation between the collection area and the growth

interface[192,193]. If the collection area extends to the substrate, the collection area and growth rate also become dependent on nanowire length. In such a case, nanowires can have overlapping collection areas, and will compete for material[194].

Diffusion in the liquid or solid nanoparticle

The reactants (III–V material) can diffuse through the nanoparticle (by bulk diffusion) or along the particle–crystal interface (by interface diffusion) to contribute to nanowire growth[195] (Figure 5.4a and b). Diffusion through the seed particle has previously been modelled for nanowire growth from liquid[196] and solid[195,197,198] nanoparticles. However, the models involve the solution of Fick's law in different geometries, and the mathematical details are outside the scope of this thesis. Only a rudimentary treatment is given here to allow for a qualitative discussion.

Figure 5.4a shows a schematic of PAG of a nanowire by the nucleation and propagation of a step flow[198–202]. The concentration of the limiting growth reactant (for instance, Ga, In, or As) is highest at the particle–vapor surface, and lowest at the particle–crystal interface. Once a step has been formed, it propagates by the sequential addition of material, which leaves behind a terrace of newly nucleated material (Figure 5.4b). Interface diffusion occurs either on the top (Figure 5.4b) or the bottom terrace (Figure 5.4c). Since there is a concentration gradient within the particle, interface diffusion from the top terrace (J_{top}) will gradually decrease, whereas the interface diffusion from the bottom terrace (J_{bottom}) increases as the step propagates. Furthermore, the length of the step is not constant for a step flow, but first increases before it decreases due to the geometry of the particle-crystal interface (Figure 5.4d).
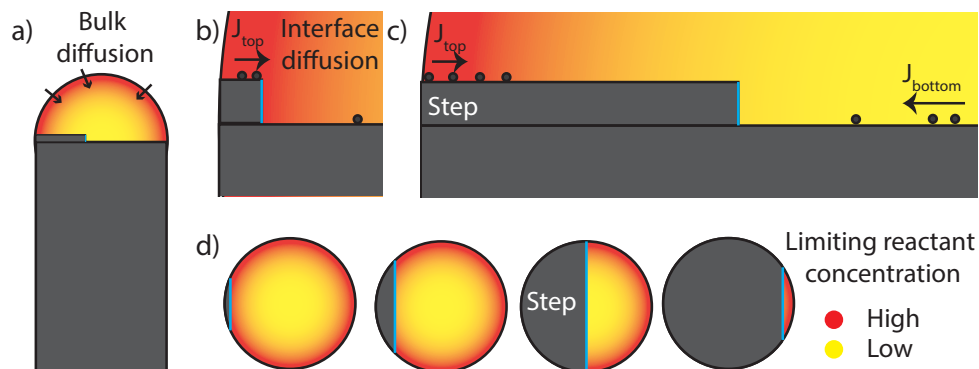
Figure 5.4. Illustration of step flow in PAG of a nanowire, color-coded with the limiting reactant concentration from a) bulk diffusion. b) Initial step formation and propagation with material supplied by interface diffusion on the top (J_{top}) and bottom (J_{bottom}) terrace. c) side view and d) top view. Black circles depict the diffusion of a limiting reactant.

There are reports of nanowires grown inside a TEM, allowing in-situ characterization of the nanowires and nanoparticles. In-situ TEM studies have not been available in this work, but reports of PAG from liquid[201,203] and solid[199–201] nanoparticles have shown different step-flow dynamics. Typically, nanowire growth from liquid nanoparticles exhibits a waiting period between rapid step flows, whereas nanowire growth from solid nanoparticles tends to proceed by continuous, but slow step flows[203]. This can be explained by the lower diffusivity or solubility in a solid than in a liquid.

Nucleation

In Chapter 2, it was shown that the nucleation rate scales with the inverse exponential of the nucleation barrier, and that the nucleation barrier can be lowered further by certain surfaces This can be applied to compare the different nucleation sites relevant in PAG. The most relevant sites are the: 1) substrate–vapor and 2) particle–crystal interfaces, and 3) the particle–crystal–vapor boundary (Figure 5.5)
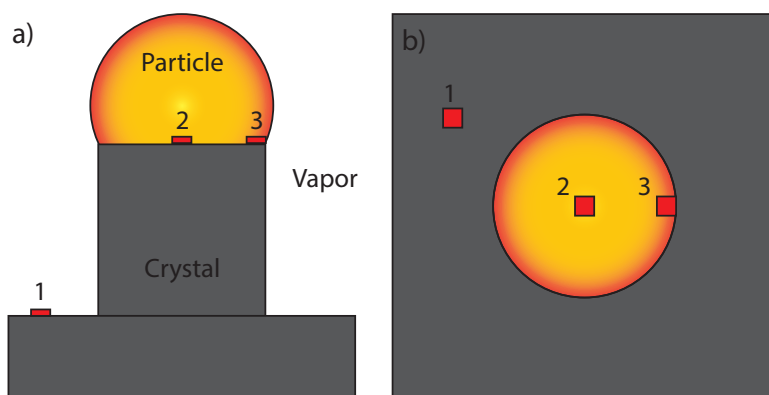
Figure 5.5. Schematic illustrating nucleus formation at various sites: 1) substrate–vapor, 2) particle–crystal, and 3) particle–crystal–vapor. a) Side view and b) top view.

According to Wacaser[172], the change in Gibbs free energy (ΔG) upon forming a nucleus on an atomically smooth facet at locations 1 to 3 can be written as:

$$\Delta G_1 = -n\Delta\mu_{vc} + Ph\gamma_{vc}$$

$$\Delta G_2 = -n\Delta\mu_{pc} + Ph\gamma_{pc}$$

$$\Delta G_3 = -n\Delta\mu_{vc} + P_{pc}h\gamma_{pc} + P_{vc}h\gamma_{vc}$$

where $\Delta\mu$ is the chemical potential difference per n atoms added to the nucleus, P the nucleus perimeter, and γ an interface energy between two of the three phases, vapor (v), particle (p) and crystal (c). A thermodynamic driving force for PAG growth requires that $\mu_{vc} > \mu_{pc}$, thus for the nucleation barrier at the nanowire growth interface to be smaller than the nucleation barrier at the substrate $(\Delta G_1 > \Delta G_2)$, it is necessary that $\gamma_{vc} > \gamma_{pc}$. In addition, since supersaturation is highest in the vapor, the simple relations indicate that the nucleation barrier is lowest at the triple-phase boundary between the particle, the crystal and the vapor, as the nucleus can adjust to minimize the contributions from γ_{pc} and γ_{vc} [172,204].

The assumption of a flat interface is a crude simplification, and studies of nanowires grown in modified transmission electron microscopes has *in situ* revealed a periodically changing morphology at the growth interface[205]. For many liquid seed metal systems, including Al-seeded α-Al$_2$O$_3$[206] and Au-seeded Ge[207], Si, GaAs and GaP[203,205], a truncated corner has been observed at the triple-phase boundary during nanowire growth. The truncated corner has also been observed in nanowire growth from solid Cu nanoparticles[205]. The volume of the truncated corner is known to oscillate with the supersaturation of the nanoparticle, being large when the supersaturation is high, and diminishing rapidly after the nucleation and step flow of a new bi-layer[203]. It has been speculated that the volume of the dissolved corner corresponds to the number of atoms of a single step flow, and that the truncation provides a pathway for low-solubility species to reach the growth interface[206]. Arguably, the presence of a truncated corner questions the validity of a flat particle–crystal interface, and additional research is thus required on interface dynamics.

6. Nanowire growth techniques

In this chapter, the nanowire growth techniques used to grow nanowires in the present work, namely MOVPE and Aerotaxy, are introduced. Both techniques use MO precursors to ensure the controlled supply of III–V species to the growth interface. Schematics of PAG using MOVPE and Aerotaxy are shown in Figure 6.1. In MOVPE, nanoparticles are deposited onto a crystalline substrate, from which nanowires grow epitaxially (crystallographically aligned). In Aerotaxy, the nanoparticles are not deposited on a substrate, but remain in the gas phase, while passing through a modified CVD reactor, or Aerotaxy reactor to form nanowires that are later deposited.
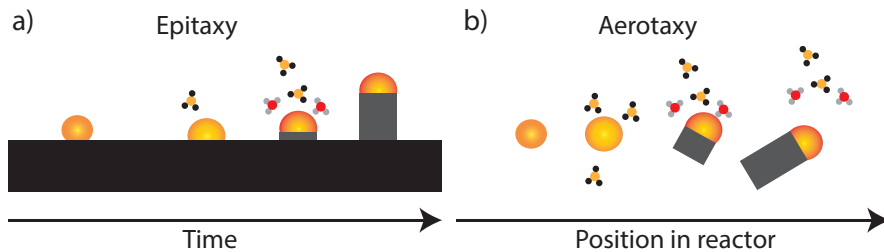
Figure 6.1. Schematics of the two nanowire growth processes used in the present work: a) Metal organic vapor phase epitaxy (MOVPE) for epitaxial growth of III–V nanowires from metal nanoparticles on substrates, and b) Aerotaxy for gas-phase synthesis of III–V nanowires from airborne metal nanoparticles.

Metal organic vapor phase epitaxy

The birth of MOVPE is often attributed to the pioneering work by Manasvit et al.[208] in the late 1960s, who grew compound semiconductors of II–VI, III–V, and IV materials as single crystals on various substrates. In the early 1980s, MOVPE competed with MBE for the production of compound semiconductor materials in commercial devices. Initially, the devices grown with MBE had superior properties to those made with MOVPE. Problems, such as compositional graded heterointerfaces were encountered in MOVPE due to recirculating gases, but with improved reactor designs atomically sharp interfaces eventually became possible. Furthermore, MOVPE

suffered from carbon contamination from the MO precursors, resulting in poor device performance. It was found that the presence of atomic H from, for example, decomposed AsH$_3$, greatly reduced the amount of carbon incorporation[209]. Nowadays, devices produced with MBE and MOVPE are of similar quality, but MOVPE remains more suited for large-scale production of, for example: LEDs, photocathodes, solar cells, transistors and integrated circuits. AIXTRON, a leading MOCVD manufacturer, delivers a MOCVD reactor, "AIX R6", capable of high-volume and cost-efficient growth of 121x2″ wafers for GaN LED fabrication[177].

Experimental setup – AIXTRON 3x2″ close-coupled showerhead

The MOCVD machine used in this work was an AIXTRON 3x2″ close-coupled showerhead (CCS) reactor (Figure 6.2a). The CCS provides a water-cooled gas inlet that allows the group III and V precursors to be introduced through separate openings near the sample, to reduce premature precursor mixing and decomposition. During growth, the III–V substrates rest on the heated, rotating susceptor. Beneath the susceptor is a resistive heater with separate heating zones.
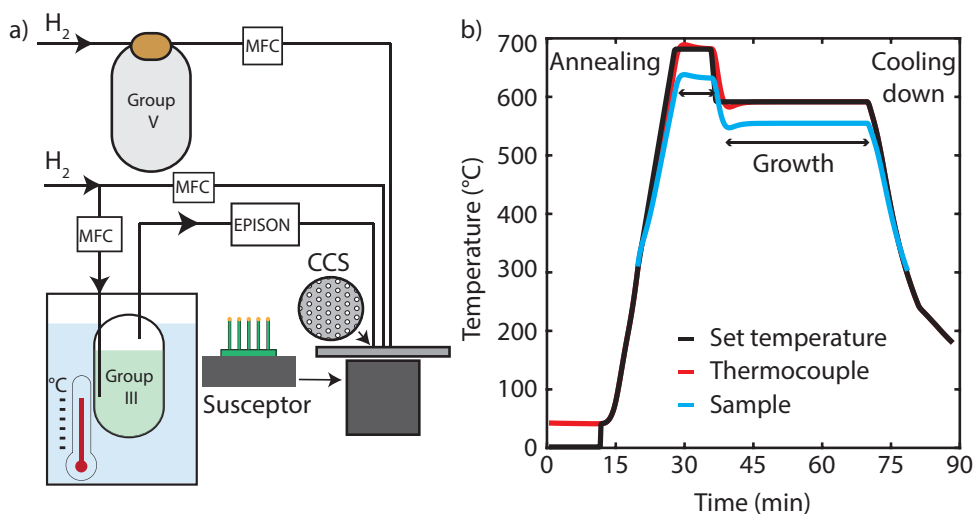
Figure 6.2. a) Schematic of the AIXTRON 3x2″ CCS MOCVD reactor, gas flow is controlled with mass flow controllers (MFCs). b) Temperature profile for the growth of GaAs nanowires (Paper II).

Before growth commences, one or several substrates with nanoparticles are inserted into the reactor. In this work, the nanoparticles were generated exclusively in the SDG, and deposited with a controlled nanoparticle density and size. Other groups tend to use other nanoparticle preparation techniques, for example, annealing of thin metal films to form clusters of nanoparticles or dispersion of colloidal

nanoparticles[210]. A disadvantage of aerosol-deposited nanoparticles is the lack of position control, which is achievable with the other two techniques if used in combination with lithography. Advantages include a great flexibility and purity of the choice of seed metal, and high control of both the particle diameter and density.

The growth parameters are set according to a user-written growth recipe that consists of three main stages: annealing, growth, and cooling. Figure 6.2b shows the temperature profile for the growth of GaAs nanowires using the AIXTRON 3x2″ CCS (Paper II). After annealing, the temperature and group V concentration are set according to the growth recipe. When the temperature has stabilized, the group III flow is supplied, and growth is assumed to have begun, and to have stopped when the group III flow is turned off. There may be a short incubation time before the nanowire nucleates, and residual group III species (in the reactor and the seed particle) can allow nanowire growth to continue after the supply has been turned off. Therefore, the set growth time may differ from the actual growth time. During incubation, the nanoparticle composition changes and the nanoparticle becomes sufficiently supersaturated for growth to commence.

Three different temperatures are presented in Figure 6.2b: the set temperature defined by the recipe, the temperature readout from the thermocouple during growth, and the sample temperature. The thermocouple is positioned beneath the susceptor located near the heater, and its temperature closely follows the set temperature. However, the sample is placed on the susceptor, further away from the heater, and the sample temperature is therefore expected to be slightly lower than the set temperature. The sample temperature is the reflectometry-calibrated temperature of a heated GaAs substrate. However, the calibrated sample temperature may differ from the actual temperature at the nanowire growth front, since the flow of precursors and chemical reactions may affect the temperature in complex ways. At higher temperatures (>600°C) there is a discrepancy of about 60 °C between the thermocouple measurement and the sample temperature. There is no consensus regarding which temperature should be reported. In Paper II, the set temperature is given, whereas in Paper III the sample temperature is given as the "real" temperature, but it is generally accepted that growth parameters are not directly transferrable between growth reactors.

Annealing nanoparticles on III–V substrates

In order to remove the native oxide of the III–V substrate, as well as potential organic residues[210], the III–V substrates decorated with metal nanoparticles are heat-treated briefly in the MOCVD chamber. This heat treatment is known as annealing. To prevent GaAs or InAs from decomposing during annealing or cooling, AsH_3 is typically supplied when the temperature exceeds 300 °C.

Annealing can have undesired effects on the nanoparticle distribution, since at elevated temperatures the nanoparticles can move[211,212], evaporate, or alloy with the substrate[213]. When the interactions between metal nanoparticles and semiconductor surfaces are unknown it is necessary to verify that the nanoparticles survive the annealing step. In the present work, it was observed that low-melting-point metals such as Pb, Bi, and Sn were sensitive to the annealing temperature, and disappeared from GaAs when annealed and exposed to AsH_3. Higher-melting-point metals, such as Au, Co, Pd, Pt, and Rh usually remained on the substrate after annealing. As the nanoparticles are randomly positioned, it was not possible to determine whether they moved or not. A low-temperature nucleation step or containment of the nanoparticles in a patterned oxide could be tried to prevent nanoparticle movement[212,213].

Figure 6.3 shows SEM images of 30 nm Pd nanoparticles on GaAs (111)B substrates before and after 7 minutes of annealing at a set temperature of 680 °C. Considerable reshaping has occurred, but the nanostructure density remains similar. This has not been studied in detail, but it is possible that the nanoparticle alloys with the substrate and moves around[214]. During cooling, the nanoparticles precipitate GaAs to form the larger nanostructures visible in Figure 6.3 b).
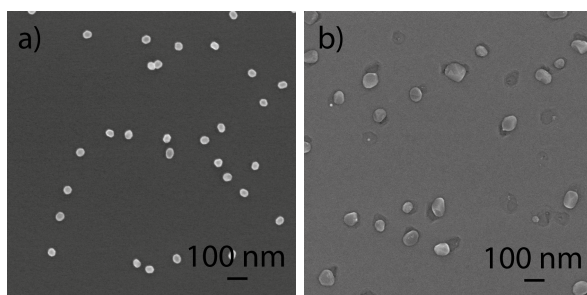
Figure 6.3. SEM images of Pd nanoparticles (top view): a) as initially deposited on GaAs(111)B substrates, and b) after 7 minutes of annealing at 680 °C in the presence of AsH_3.

Reconstructing the time-evolution of a nanowire

The development of a nanowire can be reconstructed by running a growth recipe with a series of growth times, which is referred to as a time-series. In the work described in Paper III, it was desired to grow a high yield of vertically aligned InAs nanowires and to gradually accumulate In in the nanoparticles. The average particle diameter was found to increase over time (Figure 6.4a, red line), but the nanowire density decreased (blue line). The statistical data were collected by imaging hundreds of nanostructures per data point, and SEM images of typical nanostructures illustrate the nanowire development, see Figure 6.4b). The length of the vertical nanowire

segments can be used to estimate growth rates or to study the time-dependent or radius-dependent growth rate (Figure 6.4c).
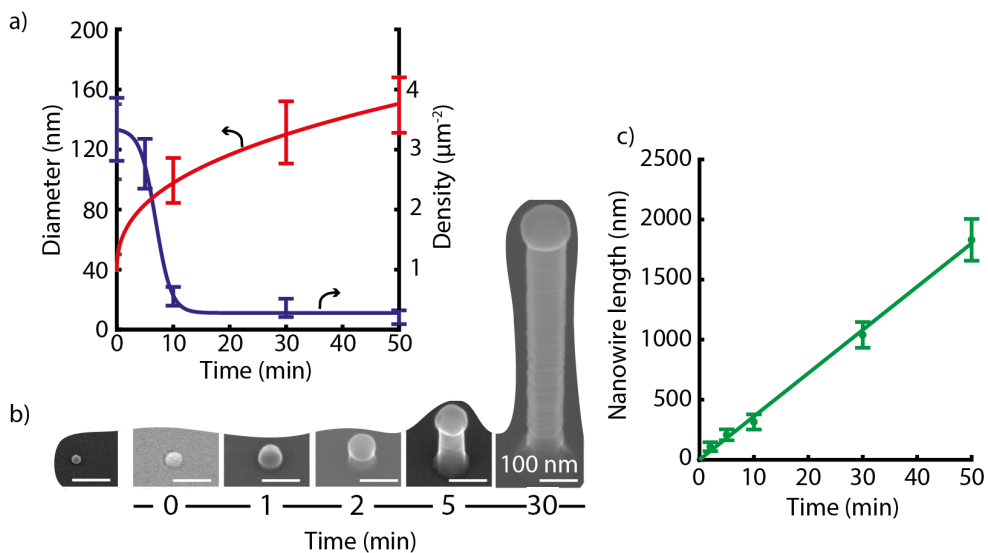
Figure 6.4. a) Statistical analysis of particle diameter (red) and vertical nanowire density (blue). (Some data points have been removed to reduce cluttering.) b) SEM images of a 30 nm Pd nanoparticle, and Pd-seeded InAs nanowires for different growth times (tilted 30 °). The first two images show a deposited nanoparticle and an annealed nanoparticle. c) Length of vertical nanowires as a function of growth time. (Adapted from Paper III.)

It is important to bear in mind that such a time series is a reconstruction of the development of a nanowire, and is not identical to an observation of a nanowire *in situ*. The nanowire length, diameter and growth rate can be determined *in situ* using optical reflectometry, but this requires well-known samples with a high degree of homogeneity[215]. If a mass spectrometer is connected to the MOCVD reactor, it would be possible to investigate the precursor decomposition, in contrast to only monitoring what is supplied[216].

Aerotaxy

Aerotaxy was first reported for the growth of GaAs nanocrystals from Ga aerosol nanoparticles, heated in the presence of AsH_3 in a modified CVD reactor[217]. Without a supply of group III material, nanoparticle growth ceases when the Ga reservoir in the nanoparticle has been spent in forming GaAs. To grow nanowires, it is beneficial to use a seed particle that is not consumed during nanowire growth, as has been done for gas-phase growth of Si nanowires from Fe, Au, and Ni nanoparticles[218]. The method used is known as laser-catalyzed growth, where a pulsed laser evaporates a slab of Si with traces of a seed metal, to form a supersaturated vapor of metal and IV material. The technique was later extended to include III–V, and II–VI semiconductors[219], and the size selection was refined by separating the catalyst formation step from the laser ablation step[220]. Today, size-selected foreign metal nanoparticles are also used in Aerotaxy for the continuous growth of III–V nanowires under the presence of group III and group V precursors[79,221–223]

Experimental setup – Aerotaxy Gen 3.5

The Aerotaxy reactor used in this work is known as the Gen 3.5, and is the latest Aerotaxy reactor at Lund University. In contrast to MOCVD, which is used worldwide for research and commercial applications, Aerotaxy is only used in Lund. In addition to the Gen 3.5 reactor, more advanced reactors, capable of generating higher volumes of nanowires for solar cell applications, have been developed. These reactors are the property of the Lund University spin-off company Sol Voltaics®, and were not available for this work.

In Aerotaxy, the aerosol nanoparticles are typically generated with an evaporation furnace or an arc source, but in the present work the SDG was used to provide greater flexibility in the choice of seed metals. The aerosol system described in Chapter 4 was used to produce compact size-selected nanoparticles (Figure 6.5a), and the nanoparticles were directly transported to the Aerotaxy reactor (Figure 6.5b).
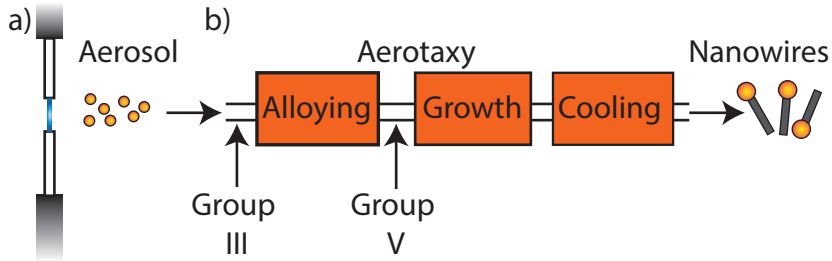
Figure 6.5. Schematic of the Aerotaxy Gen 3.5 reactor. a) Nanoparticles are generated with the aerosol system described in Chapter 4 and delivered to the Aerotaxy reactor, b), where they first alloy with group III species before nanowire growth commences.

There are three temperature-controlled zones in the Gen 3.5 Aerotaxy reactor. The first is the alloying zone where the group III precursor starts to decompose and alloy with the nanoparticles. The second is the growth zone, where the group V precursor is injected, and the growth temperature is set. The third is a cooling zone where the temperature can decrease gradually. The Aerotaxy reactor is a concentric flow reactor and consists of multiple heat zones and precursor inlets. For a simple undoped binary semiconductor such as GaAs, TMGa is supplied before the alloying stage, and AsH_3 is supplied between the alloying and growth stages. The nanoparticles are transported by an inert carrier gas, N_2, which is separated from the reactor walls by a sheath flow. This confines the aerosol and precursors to a central channel, which reduces interactions with the hot reactor walls, and allows some tuning of the diameter of the central channel. In principle, this can be also used to tune the time the aerosol remains in the reactor.

7. Particle composition and its effects on nanowire morphology

PAG proceed by either the vapor-liquid-solid (VLS) or vapor-solid-solid (VSS) growth mechanism, depending whether the particle is liquid or solid during growth. The names refer to the pathway of the semiconductor species, which adsorb from the vapor, dissolve and diffuse through the liquid or solid particle and finally precipitate as a solid at the particle–crystal interface. The PAG mechanism was discussed in Chapter 5, and some differences in the nanowire growth mechanism can be expected between VLS and VSS. In this chapter, the factors that govern the nanoparticle phase and how it may affect nanowire morphology are discussed in relation to the results presented in Papers II and III. Finally, some unpublished Aerotaxy results on Au, AgAu- and Ag-seeded GaAs are briefly presented.

Eutectic systems

Many metals that have been considered as seeds for nanowire growth have a melting point that is 100s to 1000s °C above the growth temperature; therefore, as pure elements they are solids during nanowire growth. However, the metal alloys with semiconductor species during nanowire growth, which often lowers the melting point, sometimes sufficiently for it to melt at the growth temperature.

The binary phase diagrams of Si and potential seed metals provide an idea of how the seed metal phase is governed by its composition and temperature. In the present work, the seed was alloyed with group III and V elements, which forms a more complicated ternary system, and therefore, the limitation of a binary phase diagram description are discussed later in the chapter.

Si–seed metal systems

A schematic eutectic binary phase diagram of Au and Si is shown in Figure 7.1a. The term eutectic originates from the Greek *eu* meaning easy and *teksis* meaning melting. The name is well chosen, since at the eutectic composition of 17 at% Si and 83 at% Au, the mixture melts at 370 °C, which is more than 600 °C below the melting temperature of Au, and almost 1000 °C below that of Si. Si also forms eutectic systems with other transition metals and group III metals, but the eutectic melting temperature is usually higher than with Au. The few exceptions are the low-melting-point metals with a eutectic composition below 1 at% Si, e.g., Cd, Ga, In, and Zn, where the eutectic melting point is very close to the melting point of the pure metal (Figure 7.1b and c). Other metals often form higher-melting-point eutectics with Si (e.g., Ag, Al, Co, Cu, Ir, Ni, Pd, Pt, and Rh) (Figure 7.1b, d, and e). The choice of semiconductor and precursor governs the temperature range in which nanowire growth can proceed, and only a few metals form sufficiently low temperature eutectic systems to melt under typical nanowire growth conditions.
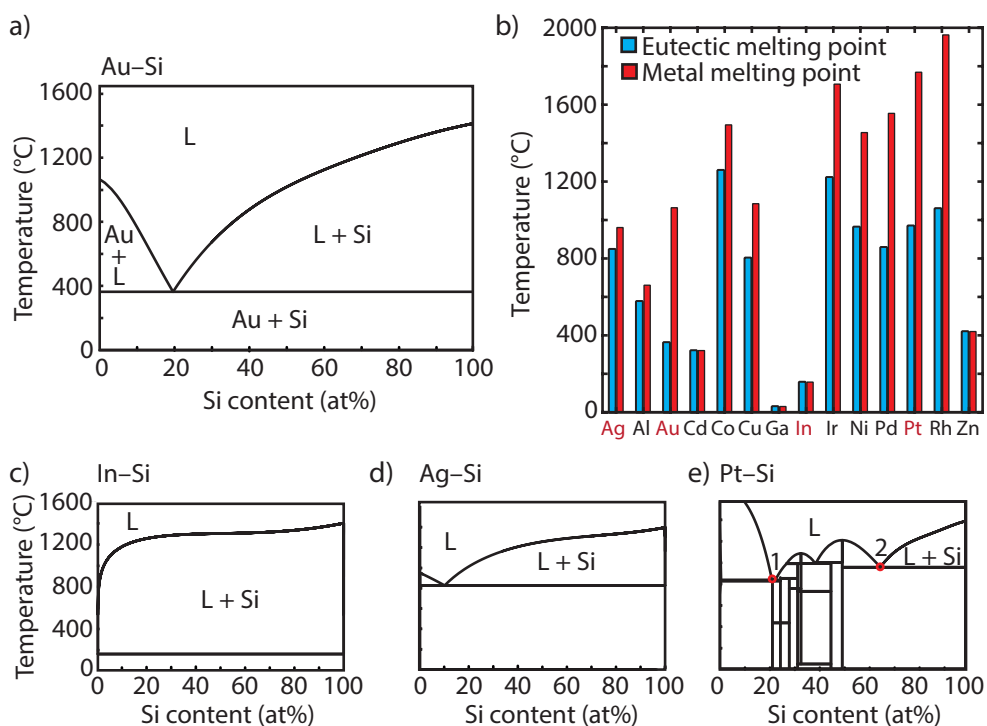

Figure 7.1. Binary phase diagrams for seed metals and Si, that highlights the liquid (L) + Si, and L regions. a) Eutectic system consisting of Au–Si. c) Low-solubility eutectic of In–Si, higher-melting-point eutectic d) without intermetallic compounds (Ag–Si) and e) with intermetallic compounds (Pt–Si). b) Melting points and eutectic melting points for metal–Si systems.

For the Au–Si system, there are no intermetallic compounds, and a binary mixture of Au and Si is limited to a combination of the three stable condensed phases: liquid (*L*), fcc-Au and diamond-Si (Figure 7.1a). Hence, when a liquid or solid Au–Si alloy is supersaturated with Si, the Si simply precipitates. However, when a system contains intermetallic compounds the description becomes more complicated. An intermetallic compound has a crystal structure that differs from those of its pure components. Therefore, for example, when a liquid or solid Pt–Si alloy is supersaturated with Si, either an intermetallic compound or Si may be precipitated, depending on its composition. For example, consider the two eutectic melts illustrated in Figure 7.1e with 20 at% Si and 66 at% Si, where only the latter eutectic neighbors the Si phase. A eutectic melt with only 20 at% Si can precipitate numerous intermetallic compounds before the Si phase becomes the only energetically favorable phase, whereas in the second case with 66 at% Si, the Si can be precipitated directly.

Limitations of a binary phase diagram

For III–V nanowire growth, the metal nanoparticle is supersaturated with group III and V elements. The phase diagrams of seed metals and group III metals are often qualitatively similar to those presented previously for Si. Typically, group V elements (such as As) have a low solubility in the seed metal, and in the present work no As phases in Au, Pd, Pb, or Co nanoparticles were identified after growth. Therefore, the seed particle in III–V nanowire growth is often described by a simple binary phase diagram for typical seed metals and group III elements (Ga or In). For low As concentrations the effect on melting point is small[224], but there are reports on seed metals that post-growth consists of an As phase when, for instance when using Ag[7] or Sn[25] seeds.

A phase diagram treats the thermodynamic equilibrium of a bulk system as a function of the actual temperature and the actual composition. During nanowire growth, the nano-scale system is not at thermodynamic equilibrium. It is also naïve to assume that the growth temperature or post-growth is identical to the temperature of the nanoparticle and composition during growth. Moreover, for III–V nanowire growth, some group V material must be dissolved in the nanoparticle, for the nanoparticle to become supersaturate, which may further change the thermodynamic equilibrium. These complications make it difficult to determine the nanoparticle phase reliably based on the phase diagram of the group III element and seed metal, growth temperature, and post-growth composition.

Tuning the nanoparticle composition

Figure 7.2 shows the binary phase diagrams of Au–In and Pd–In, at the growth temperature of 365 °C (Paper III). The convention is to refer to the components of an alloy in alphabetical order, but in Figure 7.2b) it is reversed to facilitate a direct comparison with Figure 7.2a). Both metals form intermetallic compounds with In, and there are several eutectics, but the Pd–In has a significantly higher melting point. Note, the similarity to the Si phase diagrams shown in Figure 7.1, with the drastic reduction in melting point with increasing Si or In concentration, but remember that there are no III–V phases in these binary diagrams. To treat what compositions that are possible to supersaturate with the III–V a ternary description is required.
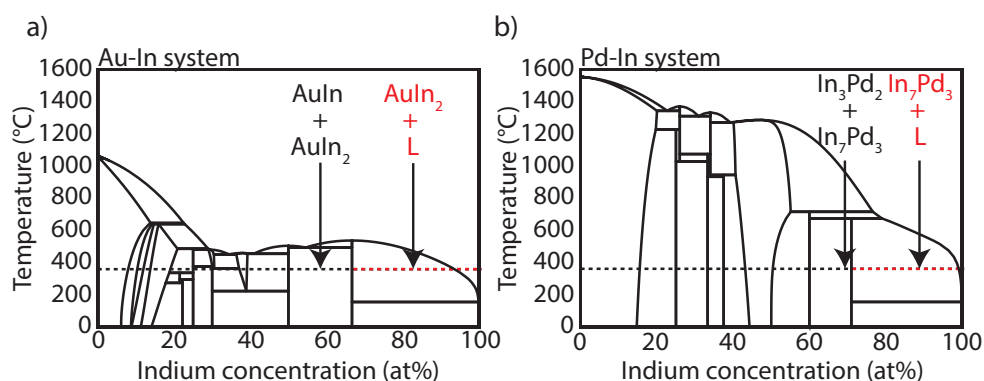
Figure 7.2. Binary phase diagrams of a) Au-In and b) Pd-In. The growth temperature of 365 °C is indicated by the dashed line, and the In-rich region is indicated in red.

The growth temperature is clearly below the eutectic melting points, except for the In-rich eutectic at >99 at% In. For Au–In or Pd–In alloys to melt completely at the growth temperature, the In concentration must exceed 94 at% with Au and 99 at% with Pd. However, for the liquid phase to be stable at the growth temperature, it is sufficient for the In concentration to be above that of the most In-rich compound at the growth temperature ($AuIn_2$ and In_7Pd_3). This composition is indicated in red in Figure 7.2 and such compositions are referred to here as In-rich.

Seed metals alloy differently with In, and the minimum In concentration in an In-rich alloy therefore varies. For example, the In-rich concentration (at 365 °C) begins at 66 at% In with Au, whereas with Ag, it starts at about 35 at% In, and at 70 at% In with Pd and Pt. Similar observations can be made for metals alloyed with Ga to form Ga-rich alloys. Therefore, based on the binary phase diagram, increasing the group III concentration of the seed metal appears to be a generally applicable strategy to bring about melting of even the most high-melting-point seed metals. Group III-rich seed

particles, can thereby offer a pathway for VLS nanowire growth from a wide variety of seed metals.

In the study presented in Paper III, InAs nanowires were grown from Au and Pd nanoparticles. The relative supply of precursors was changed to control the group III concentration in the nanoparticle (Figure 7.3a). The relative supply of precursors is referred to as the V/III ratio, or nominal V/III ratio if necessary to distinguish it from the effective V/III ratio that enters the nanoparticle. Growth at a low V/III ratio leads to the accumulation of In in the nanoparticle, causing it to grow and become more In-rich over time (black line in Figure 7.3a). This can be compared to growth at a high V/III ratio, which leads to depletion of In from the nanoparticle until the In concentration stagnates as it approaches that of an intermetallic compound (red line in Figure 7.3a). The rate of In accumulation or depletion can be reduced to almost zero by carefully controlling the V/III ratio, allowing a near-steady-state particle size to be achieved (green and turquoise lines in Figure 7.3a).
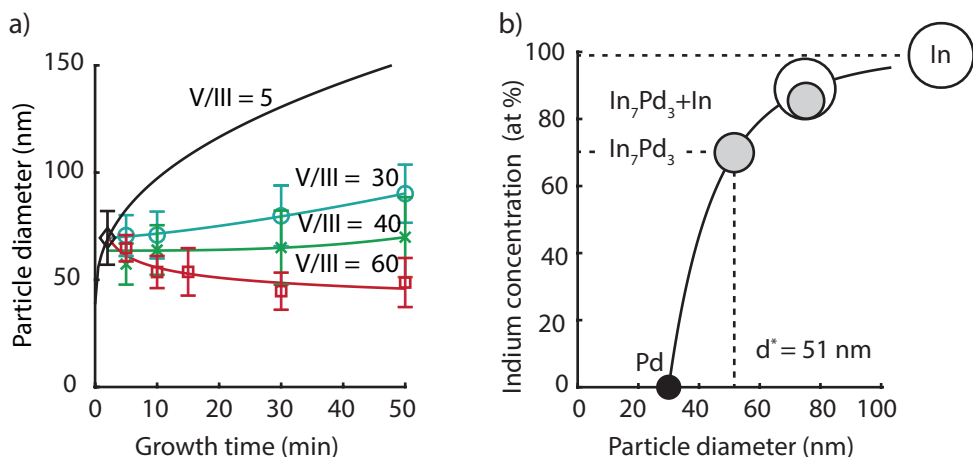
Figure 7.3. a) Particle diameter of 30 nm Pd nanoparticles after nanowire growth at different V/III ratios as a function of growth time. Note, all experiments began with 2 minutes of growth at a V/III ratio of 5. b) Relationship between nanoparticle diameter and expected In-concentration of 30 nm Pd seeds.

If the initial size of the nanoparticle is known, the In concentration in an alloy nanoparticle can be approximated from the increase in particle volume (Figure 7.3b). In the present work, the density of the alloy was approximated from linear inter-polation between the density of Pd and In. By tuning the V/III ratio, the particle size, and thus the composition, can be tuned reversibly. Phase transitions may occur when the composition changes; for example, if this takes place near the In-rich eutectic, many seed metals such as Pd, will show transitions between liquid, liquid–solid and solid (Figures 7.2 and 7.3b). Of course, the particle size is only a crude approximation

of its composition, and the nanoparticle composition must also be confirmed with other techniques such as TEM (see Paper III).

Nanowire morphology

A common difficulty encountered in studies on the effect of the seed particle lies in finding growth parameters for homogeneous and controllable nanowire growth. To illustrate this, SEM images of nanowires grown from Pd-seeded InAs at different group V flow and growth temperatures are shown in Figure 7.4. The details of the structures or the actual growth conditions are unimportant, but it important to know that a difference in morphology can be triggered by a temperature change of a few °C, or by tuning the V/III ratio by a few percent. Predictive models of which growth parameters to use are lacking, especially for III–V nanowires, and developing growth parameters for a new material system requires meticulous optimization to find appropriate growth parameters.
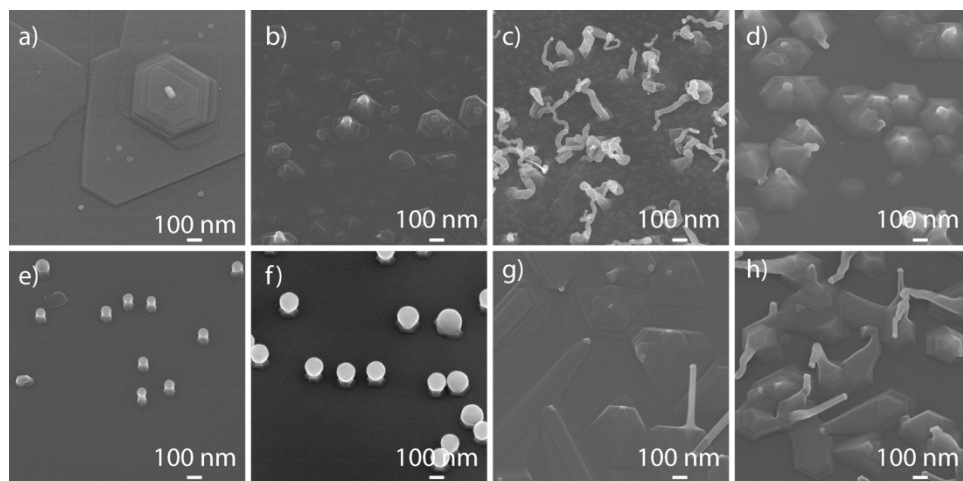
Figure 7.4. SEM images after growth from 30 nm Pd nanoparticles under various InAs growth conditions (tilted 30° seen from above).

Au and Pd nanoparticles were used as seeds for GaAs and InAs nanowires (Paper II and III). It was found that it was necessary to tune the nanoparticle composition to control the nanowire morphology and growth direction. Nanoparticles with a high group III concentration (In or Ga) were associated with vertical nanowires, whereas nanoparticles with a group III concentration near that of an intermetallic compound

($AuIn_2$, In_2Pd_3, and $GaPd_3$) were associated with uncontrolled growth directions such as those shown in Figure 7.4c).

In the present work, nanowire growth from various metals was investigated using MOCVD, including: Au, Bi, Co, Rh, Sn, Pb, Pd, and Pt. Each metal has different material properties and behaves very differently as a seed in nanowire growth. Several substrates with different seed metals, as well as blank substrates without seed metals, were employed for side-by-side growth. The nanoparticles were deposited with a similar density and diameter to ensure that any differences observed in the resulting nanowire morphology were not due to the effects of particle distribution. However, even with similar particle distributions, a shared growth regime with homogeneous nanowire growth was rare. A shared growth regime refers to growth parameters that yield similarly well-controlled nanowire growth, mainly referring to a large fraction of vertically aligned nanowires with similar dimensions. Without a shared growth regime and homogeneous nanowire distribution, it is difficult to characterize and compare nanowires from different seed metals, which hampers the development of alternative seed particles.

Curly, inclined and vertical nanowires

Nanowires grown from Pd nanoparticles have been reported to be straight if the nanoparticle is small, whereas nanowire growth direction and morphology are random for larger nanoparticles[21,22]. It has been argued that smaller nanoparticles have a lower melting point and higher solubility of group III species[21,22,225], and a recent report also confirms a higher group III concentration in smaller nanoparticles after growth[23]. However, there were no reports of any attempts to control the particle size or composition with the aim of obtaining uniform nanowire morphology.

The effect of growth parameters on nanowire morphology was studied for Pd-seeded GaAs nanowires (Paper II). Three nanowire morphologies were identified: uncontrolled curly nanowires, inclined straight nanowires and vertical straight nanowires (Figure 7.5). The relative yields of the three morphologies were found to be controllable with growth parameters; high growth temperatures and low V/III ratios promoting straight nanowire growth. It was found that under growth conditions resulting mainly in straight and vertical nanowires, the nanoparticles had a higher Ga concentration (~70 at% Ga), than nanoparticles from growth conditions resulting mainly in curly nanowires (~43 at% Ga). This suggests that a higher Ga content is beneficial for straight nanowire growth. It was proposed that the curly nanowire morphology was seeded by a solid nanoparticle, whereas the straight nanowires may have had liquid nanoparticles during growth.
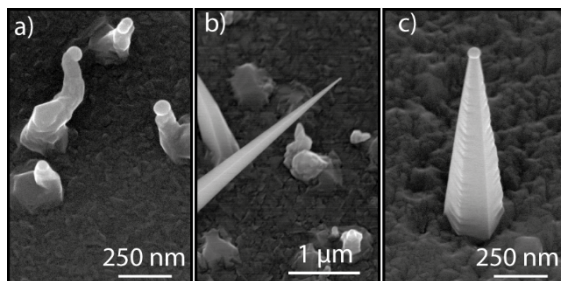
Figure 7.5. SEM images of three nanowire morphologies: a) curly, b) inclined, and c) vertical nanowires (tilted 30 °).

A large growth parameter space was investigated, and curly nanowires were by far the most common; vertical nanowires only being seen in a narrow growth window. Even when all the nanowires were vertical, the yield of nanowires was very low, indicating that a better technique is required to achieve high yields of vertically aligned Pd-seeded nanowires.

The curly nanowires were found to have an anisotropic particle–crystal interface and the nanowires were riddled with crystallographic twins (Paper II). Since a nanowire grows by a series of step flows across the particle–crystal interface it is likely that a poor interface between the particle and crystal is detrimental to a stable growth direction. A curly nanowire may eventually form a good interface with the particle, and continue in a stable growth direction for a long time. This was sometimes observed, with both SEM and TEM. Therefore, to control the nanowire growth direction with solid nanoparticles, it is necessary to increase the control of the interface that forms between the nanoparticle and the substrate.

Morphology control with In-rich Pd- and Au-seeded InAs

Figure 7.6 shows side-by-side growth of InAs nanowires from 30 nm Au and Pd nanoparticles. Almost identical nanowires could be grown from both seed particles by controlling the In concentration of the seed particles. Vertical nanowires were achieved by maintaining the In concentration above that in the In-rich compounds ($AuIn_2$ and In_7Pd_3). Large nanoparticles tended to result in a kink in the nanowires and they continued to grow in a new direction (Figure 7.6b and f). This is most undesirable, as it is not possible to control the direction of the kink. By careful balance of the V/III ratio, the size of the nanoparticle could be approximately maintained, and the vertical nanowire morphology reserved (Figure 7.6c and g). When the In concentration was reduced below a critical value, near that of the In-rich

compound concentration, the initially vertical nanowires kinked, but continued growing with a curly morphology (Figure 7.6 d and h).
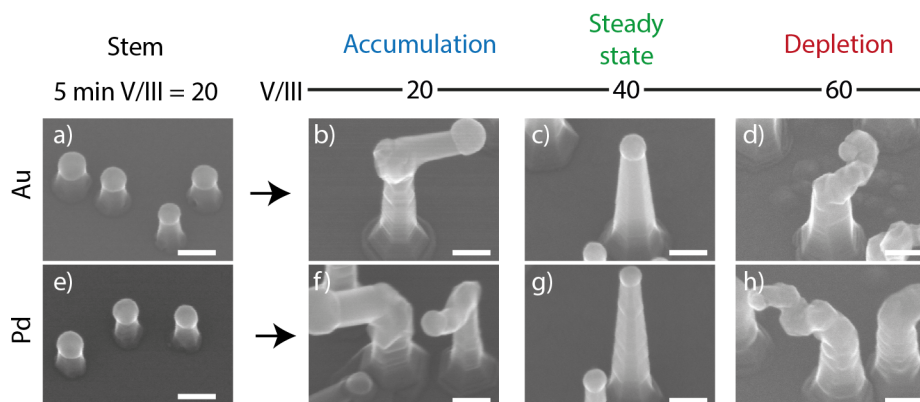
Figure 7.6. SEM images from PAG using In-rich nanoparticles with 30 nm Au (a-d) and Pd (e-h) nanoparticles grown side-by-side in the same growth chamber, on different substrates. Growth at different V/III ratios resulted in the accumulation or depletion of In in the nanoparticle, triggering changes in nanowire morphology. (Images tilted by 30°)

A high degree of similarity in nanowire morphology between the two seeding particles is strong evidence of a shared growth mechanism. This level of control of the nanowire morphology for simultaneous growth from different seed metals is, to the best of the author's knowledge, unprecedented in III–V nanowire growth.

A detailed comparison of the particle diameter and composition, and identification of the constituent phases led to the conclusion that the transition from vertical to curly nanowire morphology was due to a phase transition of the seed particle. The vertical morphology was associated with a two-phase nanoparticle, whereas the curly morphology was the result of a single solid phase. This implies that the stability of the liquid phase is important to prevent curly nanowire morphology.

AgAu seed particles to reduce the cost of Aerotaxy

In recent years, research in Aerotaxy has focused on the development of GaAs and GaP nanowires with controlled doping[222,226], and ternary compositions[223], enabling both high-throughput and low-cost production of p–n diodes[113,227], useful for industrial-scale production of nanowire-based solar cells. However, considering the high cost of Au (35 €/g), and the fact that only a fraction of the aerosol produced is size-selected, the price of the metal will be a considerable drawback in large-scale production. The cost of the seed particle could be decreased by several orders of magnitude by using cheaper metals, such as Ag (0.5 €/g), Sn (29 €/kg) Ni (19 €/kg), Cu (8 €/kg), or Fe (25 €/ton)[228]. Unfortunately, changing the seed metal usually leads to significant complications in nanowire growth. Therefore, an investigation of Au alloy nanoparticles, where the material cost depends mainly on the amount of Au in the nanoparticle, is motivated. A 50:50 at% Ag–Au alloy corresponds to a 35:65 wt% Ag–Au alloy, and the cost of such an alloy is about one-third less than that of pure Au.

Figure 7.7 shows GaAs nanowires seeded with Au, AgAu, and Ag nanoparticles, grown with Aerotaxy. Seeding with AgAu nanoparticles yields remarkably similar nanowires to those resulting from seeding with Au (Figure 7.7a-l). The striking similarity at growth temperatures between 500 and 620 °C shows that the Au concentration in the AgAu nanoparticles could be decreased with 50 at%, with little effect on nanowire growth. However, when using pure Ag seed particles, the nano-wires fail at an early stage of growth, apparent from the kink far from the seed particle (Figure 7.7m-r). This was expected from the recent work by Mårtensson et al.[229], who reported that using Au and AgAu seeds led to the growth of very similar nanowires, whereas nanowire growth using Ag nanoparticles often failed. They concluded this to the Au and AgAu seeds being liquid during growth, while the Ag seeds were solid. The difference in nanoparticle phase was explained by the difference in melting temperature, where the Ag nanoparticles required a higher growth temperature or Ga content to be liquid compared to the Ag and AgAu nanoparticles. In principle, the Ga concentration of the nanoparticle is controllable in both MOCVD and Aerotaxy. In Aerotaxy, the Ga concentration of the nanoparticle can be increased by increasing the time spent in the alloy stage, or by increasing the group III flow.
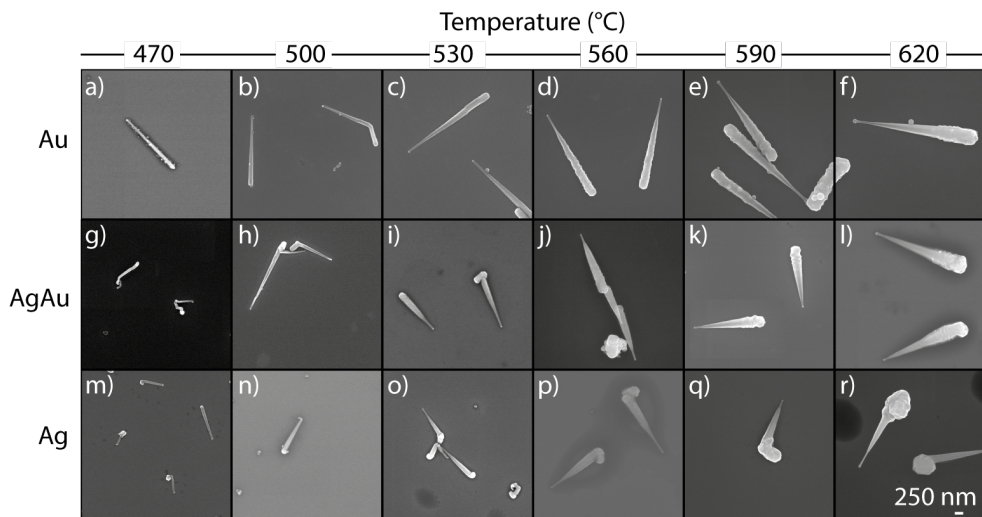
Figure 7.7. GaAs nanowires grown by Aerotaxy from 30 nm nanoparticles: (a-f) Au, (g-l) AgAu, and (m-r) Ag at different set temperatures.

The nanowires grown from Au and AgAu nanoparticles have uniform thickness at the lower growth temperatures (≤ 500 °C), but become increasingly more tapered at higher temperatures (Figure 7.7a-l). A tapered morphology can result from a gradually shrinking particle–crystal interface or radial growth of the nanowire. Performing a time series could clarify whether the particle volume changes during growth. However, it is more difficult to perform a time series in Aerotaxy than in MOCVD. Similar tapered nanowires at high temperatures have been reported in previous studies using Aerotaxy, and were explained by radial growth[79,221]. Radial growth can increase at higher temperatures, due to more precursor decomposition, a lower kinetic barrier for nucleation, and a decrease in diffusion length due to desorption (as discussed in Chapter 5). Radial growth can be suppressed by supplying etchants such as HCl[68–70] or HBr[67], but this has not yet been used in Aerotaxy. In contrast to MOCVD, there is no loss of material from competing growth on the substrate in Aerotaxy, but parasitic GaAs nucleation can still occur in the gas phase.

8. Concluding remarks and outlook

PAG of III–V semiconductor nanowires offers a powerful method of creating high-quality III–V crystals that may enable cost-efficient production of superior photovoltaic, electronic, and optoelectronic devices. In the work presented in this thesis, the production capabilities of non-noble metals for use as seed particles have been developed, and the effect of nanoparticle composition on the nanowire morphology has been studied. The results of this work show that a key to controlled nanowire growth using nanoparticles of various metals, is to reduce the melting point and allow them to melt during nanowire growth. Based on these findings, others may now design smarter experiments, using seed metals with engineered compositions. Our understanding of the nanowire growth mechanism and the versatility of PAG would benefit greatly from studying the borderline between controlled and uncontrolled nanowire growth.

The main aims of the work presented in this thesis were to extend the control of the particle composition during PAG, and to investigate how the particle phase affects nanowire morphology. There is no shortage of metals and alloys to be tested, but as was apparent from this work, additional studies are required before their benefits can be reaped. Some potential advantages of PAG with alternative metals are listed below.

1. A particle material with a low solubility of In and Ga may allow the growth of sharper heterointerfaces in Ga–V and In–V semiconductors, which is otherwise difficult as the particle acts as a reservoir, resulting in compositional graded heterointerfaces.

2. Constituents of the particle could be intentionally incorporated into the nanowire, to dope the semiconductor or tune its bandgap. However, an understanding of the mechanisms promoting or preventing incorporation would be required.

3. A particle that can be switched between an inert and active mode would be useful to prevent additional axial growth during radial shell growth.

4. A particle that is easier to remove after nanowire growth, or that could be created or removed during nanowire growth, would facilitate processing.

5. A cheaper metal would reduce the cost, and would be especially important in large-scale commercial production.

Before any of these advantages can be realized, greater familiarity with foreign non-Au seeded PAG is required. As was apparent from this work, PAG using solid nanoparticles is challenging. The formation of a flat interface between the solid nanoparticle and the nanowire is especially important. I suggest that a good first step is to form a good interface with a liquid nanoparticle, and then to trigger a solid phase transformation.

Outlook

There are many paths along which this research can be continued. The two most immediate are: 1) to use the group III-rich growth method described in Paper III to study controlled transition between liquid and solid nanoparticles, and 2) to test its generality by growing other III–V semiconductors with other seed metals. Other, more novel suggestions for future research are briefly discussed below.

Setting the initial group III concentration

When a seed particle is deposited onto a substrate and annealed it tends to react with the substrate and begin to alloy. This process is poorly understood, but the interfaces that form and the composition of the particle will naturally have a considerable effect on the initial stages of nanowire growth. If the nanoparticles were alloyed with group III material before annealing, the nanoparticle could be made more saturated with group III material, and may therefore become less prone to react with the substrate.

To obtain nanoparticles that are alloyed before annealing, alloy nanoparticles could be fabricated directly from alloy electrodes in a SDG. In the case of MOCVD, the alloy nanoparticles would probably oxidize, unless they were protected by a passivating shell. However, it must also be possible to remove the shell, for instance, by thermal decomposition in the MOCVD reactor. There would be no need for a passivating shell in Aerotaxy since the nanoparticles remain in an inert gas flow, from generation until the nanowire has been grown.

Finding low-solubility and low-melting-point alloys

One of the primary advantages of PAG using group III-rich nanoparticles is also its greatest disadvantage. Since the melting point is controlled by the relative supply of group III species, the growth parameters must be optimized to keep the particle size constant. Instead of diluting the metal nanoparticle with a group III element, elements that have a low solubility in the III–V material, such as Zn, Bi, Pb, and Sn,

could be investigated. This would also decrease the melting point of the seed metal, but if it has a low incorporation rate into the nanowire, the nanoparticle and nanowire diameter would be more stable than in group III-rich PAG. For metals with a high vapor presusre it might be possible to remove it by a simple heat treatment.

I have briefly studied nanowire growth from pure Bi, Sn, and Pb nanoparticles, and found it possible to grow GaAs nanowires (not included in thesis). Unfortunately, the growth rate was very low, probably due to the low temperature and AsH_3 flows that were required to sustain the nanoparticle. As an alloy with a high-melting-point metal, the metals may survive higher growth temperatures, which may also boost the the nanowire growth rate since the precursors pyrolysis would be more complete. The alloy melting temperature could be controlled by the concentration of the dilutant, as mentioned previously, and the particle size would be much more stable than for group III-rich PAG.

There is no need to limit the choice of particle composition to one or two constituents, making ternary (or quaternary) systems available. For instance, an alloy of Pb and Sn has historically been used as solder, but has now been replaced by the less toxic Sn–Ag–Cu alloy. Solder is an alloy with a low-melting-point eutectic, and common solders would be an interesting starting point to look for low-melting-point eutectics. For example, low-melting-point eutectics may be found in systems such as Ga–Ag–Cu or Ag–Ga–Sn, which would enable the use of more cost-efficient seed particles with variable melting temperatures.

Developing core–shell nanoparticles

A nanoparticle that consists of one material in the core, surrounded by another shell material is known as a core–shell nanoparticle. There might exist material combinations that would allow only the shell to be active in PAG, and the purpose of the core would be to define the particle size and nanowire diameter. The cost of large Au nanoparticles could perhaps be drastically reduced with this approach, since the volume of a Au shell is only a small fraction of the total volume.

Alloy or core–shell nanoparticles can be manufactured by condensation of secondary metals onto a pre-existing nanoparticle (in the gas phase). In this method, the difference in size between the initial and final particles could be used as a first approximation of the particle composition. The first step would be to study the generation of core–shell nanoparticles and to design a few core–shell constellations before attempting nanowire growth.

Future implications

In this work, I have improved the capabilities of both unary and binary metal nanoparticles for nanowire growth. A method was also developed to facilitate nanowire growth from non-Au foreign metal nanoparticles. This has led to an easy method of initiating controlled nanowire growth from different seed metals, which previously involved meticulous growth parameter sweeps. The method also allows studies of nanowire growth from both liquid or solid nanoparticles in a single growth experiment.

As our experience and confidence in additional seed metals increase, more versatile experiments can be performed to test and improve current nanowire growth models. A greater understanding of the role of the nanoparticle composition in PAG will in turn allow more complex nanowire designs. It is my hope that this will lead to a scenario where the nanoparticle composition is tailored according to the specifications of the nanowire.

References

(1)   Tavendale, A. J.; Pearton, S. J. *J. Phys. C Solid State Phys.* **1983**, *16* (9), 1665–1673.

(2)   Dick, K. A.; Caroff, P. *Nanoscale* **2014**, *6*, 3006–3021.

(3)   Boles, S. T.; Thompson, C. V.; Fitzgerald, E. A. *J. Cryst. Growth* **2009**, *311* (5), 1446–1450.

(4)   Vogel, A. T.; De Boor, J.; Becker, M.; Wittemann, J. V; Mensah, S. L.; Werner, P.; Schmidt, V. *Nanotechnology* **2011**, *22* (1), 015605.

(5)   Huang, K.; Zhang, Z.; Zhou, Q.; Liu, L.; Zhang, X.; Kang, M.; Zhao, F.; Lu, X.; Gao, X.; Junming, L. *Nanotechnology* **2015**, *26* (25), 255706.

(6)   Sarkar, K.; Palit, M.; Chattopadhyay, S.; Banerji, P. *J. Appl. Phys.* **2016**, *120* (8), 084309.

(7)   Lindberg, C.; Whiticar, A.; Dick, K. A.; Sköld, N.; Nygård, J.; Bolinsson, J. *Nano Lett.* **2016**, *16* (4), 2181–2188.

(8)   Bouravleuv, A. D.; Ilkiv, I. V; Reznik, R. R.; Shtrom, I. V; Khrebtov, A. I.; Samsonenko, Y. B.; Soshnikov, I. P.; Cirlin, G. E.; Lipsanen, H. *IOP Conf. Ser. J. Phys. Conf. Ser.* **2017**, No. 864, 012010.

(9)   Oliveira, D. S.; Zavarize, M.; Tizei, L. H. G.; Walls, M.; Ospina, C. A.; Iikawa, F.; Ugarte, D.; Cotta, M. A. *Nanotechnology* **2017**, *28* (50), 1–8.

(10)   Fanfair, D. D.; Korgel, B. A. *Cryst. Growth Des.* **2005**, *5* (5), 1971–1976.

(11)   Hillerich, K.; Messing, M. E.; Reine Wallenberg, L.; Deppert, K.; Dick, K. A. *J. Cryst. Growth* **2011**, *315* (1), 134–137.

(12)   Hillerich, K.; Dick, K. A.; Messing, M. E.; Deppert, K.; Johansson, J. *Nano Res.* **2012**, *5* (5), 297–306.

(13)   Hillerich, K.; Ghidini, D. S.; Dick, K. A.; Deppert, K.; Johansson, J. *Phys. Status Solidi - Rapid Res. Lett.* **2013**, *7* (10), 850–854.

(14)   Regolin, I.; Khorenko, V.; Prost, W.; Tegude, F. J.; Sudfeld, D.; Kästner, J.; Dumpich, G.; Hitzbleck, K.; Wiggers, H. *J. Appl. Phys.* **2007**, *101* (5), 1–5.

(15)   Martelli, F.; Rubini, S.; Piccin, M.; Bais, G.; Jabeen, F.; De Franceschi, S.; Grillo, V.; Carlino, E.; D'Acapito, F.; Boscherini, F.; Cabrini, S.; Lazzarino, M.; Businaro, L.; Romanato, F.; Franciosi, A. *Nano Lett.* **2006**, *6* (9), 2130–2134.

(16)   Jabeen, F.; Piccin, M.; Felisari, L.; Grillo, V.; Bais, G.; Rubini, S.; Martelli, F.; D'Acapito, F.; Rovezzi, M.; Boscherini, F. *J. Vac. Sci. Technol. B Microelectron. Nanom. Struct.* **2010**, *28* (3), 478.

(17) Wang, G. T.; Talin, A. A.; Werder, D. J.; Creighton, J. R.; Lai, E.; Anderson, R. J.; Arslan, I. *Nanotechnology* **2006**, *17* (23), 5773–5780.

(18) Chèze, C.; Geelhaar, L.; Brandt, O.; Weber, W. M.; Riechert, H.; Münch, S.; Rothemund, R.; Reitzenstein, S.; Forchel, A.; Kehagias, T.; Komninou, P.; Dimitrakopulos, G. P.; Karakostas, T. *Nano Res.* **2010**, *3* (7), 528–536.

(19) Heun, S.; Radha, B.; Ercolani, D.; Kulkarni, G. U.; Rossi, F.; Grillo, V.; Salviati, G.; Beltram, F.; Sorba, L. *Cryst. Growth Des.* **2010**, *10* (9), 4197–4202.

(20) Xu, W.; Choi, C.-H. *J. Heat Transfer* **2012**, *134* (5), 051022.

(21) Xu, H.; Guo, Y.; Liao, Z.; Sun, W. *Appl. Phys. Lett.* **2013**, *102* (203108), 1–5.

(22) Perumal, R.; Cui, Z.; Gille, P.; Harmand, J.-C.; Yoh, K. *Semicond. Sci. Technol.* **2014**, *29* (11), 115005.

(23) Han, N.; Wang, Y.; Yang, Z.; Yip, S.; Wang, Z.; Li, D.; Hung, T. F.; Wang, F.; Chen, Y.; Ho, J. C. *J. Mater. Chem. C* **2017**, *5* (18), 4393–4399.

(24) Sun, R.; Jacobsson, D.; Chen, I.-J.; Nilsson, M.; Thelander, C.; Lehmann, S.; Dick, K. A. *Nano Lett.* **2015**, *15* (6), 3757–3762.

(25) Sun, R.; Vainorius, N.; Jacobsson, D.; Pistol, M.-E.; Lehmann, S.; Dick, K. A. *Nanotechnology* **2016**, *27* (21), 215603.

(26) Tornberg, M.; Mårtensson, E. K.; Zamani, R. R.; Lehmann, S.; Dick, K. A.; Ghalamestani, S. G. *Nanotechnology* **2016**, *27* (17), 0.

(27) Lee, S.; Wen, W.; Cheek, Q.; Maldonado, S. *J. Cryst. Growth* **2018**, *482*, 36–43.

(28) Chou, Y. C.; Wen, C. Y.; Reuter, M. C.; Su, D.; Stach, E. A.; Ross, F. M. *ACS Nano* **2012**, *6* (7), 6407–6415.

(29) Srinivas, P. R.; Barker, P.; Srivastava, S. *Lab. Investig.* **2002**, *82* (5), 657–662.

(30) Panyam, J.; Labhasetwar, V. *Adv. Drug Deliv. Rev.* **2003**, *55* (3), 329–347.

(31) Allen, T. M.; Cullis, P. R. *Science (80-.).* **2004**, *303* (March), 1818–1823.

(32) Gao, X.; Cui, Y.; Levenson, R. M.; Chung, L. W. K.; Nie, S. *Nat. Biotechnol.* **2004**, *22* (8), 969–976.

(33) Pissuwan, D.; Niidome, T.; Cortie, M. B. *J. Control. Release* **2011**, *149* (1), 65–71.

(34) Rizvi, S. A. A.; Saleh, A. M. *Saudi Pharm. J.* **2017**, *26* (1), 64–70.

(35) Li, Q.; Mahendra, S.; Lyon, D. Y.; Brunet, L.; Liga, M. V.; Li, D.; Alvarez, P. J. J. *Water Res.* **2008**, *42* (18), 4591–4602.

(36) Hua, M.; Zhang, S.; Pan, B.; Zhang, W.; Lv, L.; Zhang, Q. *J. Hazard. Mater.* **2012**, *211–212*, 317–331.

(37) Poizot, P.; Laruelle, S.; Grugeon, S.; Dupont, L.; Tarascon, J.-M. *Nature* **2000**, *407* (28), 496–499.

(38) Liu, C.; Li, F.; Ma, L.-P.; Cheng, H.-M. *Adv. Mater.* **2010**, *22* (8), E28–E62.

(39) Jiang, J.; Li, Y.; Liu, J.; Huang, X.; Yuan, C.; Lou, X. W. *Adv. Mater.* **2012**, *24* (38), 5166–5180.

(40) Tian, B.; Zheng, X.; Kempa, T. J.; Fang, Y.; Yu, N.; Yu, G.; Huang, J.; Lieber, C. M. *Nature* **2007**, *449* (7164), 885–889.

(41) Cui, Y.; Zhong, Z.; Wang, D.; Wang, W. U.; Lieber, C. M. *Nano Lett.* **2003**, *3* (2), 149–152.

(42) Lin, J.; Chen, H.; Fei, T.; Zhang, J. *Colloids Surfaces A Physicochem. Eng. Asp.* **2013**, *421*, 51–62.

(43) Das, I.; Mishra, M. K.; Medda, S. K.; De, G. *RSC Adv.* **2014**, *4* (98), 54989–54997.

(44) Liang, Y.; Li, Y.; Wang, H.; Zhou, J.; Wang, J.; Regier, T.; Dai, H. *Nat. Mater.* **2011**, *10* (10), 780–786.

(45) Li, Y.; Wang, H.; Xie, L.; Liang, Y.; Hong, G.; Dai, H. *J. Am. Chem. Soc.* **2011**, *133* (19), 7296–7299.

(46) Marambio-Jones, C.; Hoek, E. M. V. *J. Nanoparticle Res.* **2010**, *12* (5), 1531–1551.

(47) Currall, S. C.; King, E. B.; Lane, N.; Madera, J.; Turner, S. *Nat. Nanotechnol.* **2006**, *1* (3), 153–155.

(48) Klaine, S. J.; Alvarez, P. J. J.; Batley, G. E.; Fernandes, T. F.; Handy, R. D.; Lyon, D. Y.; Mahendra, S.; McLaughlin, M. J.; Lead, J. R. *Environ. Toxicol. Chem.* **2008**, *27* (9), 1825–1851.

(49) Nazarenko, Y.; Han, T. W.; Lioy, P. J.; Mainelis, G. *J. Expo. Sci. Environ. Epidemiol.* **2011**, *21* (5), 515–528.

(50) Musee, N. *Hum. Exp. Toxicol.* **2011**, *30* (9), 1181–1195.

(51) Mulvaney, P. *MRS Bull.* **2001**, No. December, 1–6.

(52) Bensebaa, F. In *Interface Science and Technology*; Elsevier Ltd, 2013; Vol. 19, pp 1–84.

(53) Masala, O.; Seshadri, R. *Annu. Rev. Mater. Res.* **2004**, *34* (1), 41–81.

(54) De Castro, C. L.; Mitchell, B. S. *Synth. Funct. Surf. Treat. Nanoparticles* **2002**, 1–15.

(55) Scheibel, H. G.; Porstendörfer, J. *J. Aerosol Sci.* **1983**, *14* (2), 113–126.

(56) Ready, J. F. *Appl. Phys. Lett.* **1963**, *3* (11), 11–13.

(57) Berkowitz, A. E.; Walter, J. L.; Electric, G.; Introduction, I. *J. Mater. Res.* **1987**, *2* (2), 277–288.

(58) Del Alamo, J. A. *Nature* **2011**, *479* (7373), 317–323.

(59) Wernersson, L.-E. *Microelectron. Eng.* **2015**, *147*, 344–348.

(60) Wernersson, L.-E. *J. Appl. Phys.* **2015**, *117* (11), 112810.

(61) Fitzgerald, E. A. *Mater. Sci. Reports* **1991**, *7* (3), 87–140.

(62) Ertekin, E.; Greaney, P. A.; Chrzan, D. C.; Sands, T. D. *J. Appl. Phys.* **2005**, *97* (11).

(63) Glas, F. *Phys. Rev. B - Condens. Matter Mater. Phys.* **2006**, *74* (12), 2–5.

(64) Tomioka, K.; Motohisa, J.; Hara, S.; Fukui, T. *Nano Lett.* **2008**, *8* (10), 3475–3480.

(65) Yao, M.; Cong, S.; Arab, S.; Huang, N.; Povinelli, M. L.; Cronin, S. B.; Dapkus, P. D.; Zhou, C. *Nano Lett.* **2015**, *15* (11), 7217–7224.

(66) De La Mata, M.; Magén, C.; Caroff, P.; Arbiol, J. *Nano Lett.* **2014**, *14* (11), 6614–6620.

(67) Berg, A.; Mergenthaler, K.; Ek, M.; Pistol, M.-E.; Reine Wallenberg, L.; Borgström, M. T. *Nanotechnology* **2014**, *25* (50), 505601.

(68) Jacobsson, D.; Lehmann, S.; Dick, K. A. *Nanoscale* **2014**, *6* (14), 8257.

(69) Kim, S.; Hill, D. J.; Pinion, C. W.; Christesen, J. D.; McBride, J. R.; Cahoon, J. F. *ACS Nano* **2017**, *11* (5), 4453–4462.

(70) Wallentin, J.; Messing, M. E.; Trygg, E.; Samuelson, L.; Deppert, K.; Borgström, M. T. *J. Cryst. Growth* **2011**, *331* (1), 8–14.

(71) Kumakura, K.; Nakakoshi, K.; Kishida, M.; Motohisa, J.; Fukui, T.; Hasegawa, H. *J. Cryst. Growth* **1994**, *145* (1–4), 308–313.

(72) Noborisaka, J.; Motohisa, J.; Fukui, T. *Appl. Phys. Lett.* **2005**, *86* (21), 1–3.

(73) Tomioka, K.; Mohan, P.; Noborisaka, J.; Hara, S.; Motohisa, J.; Fukui, T. *J. Cryst. Growth* **2007**, *298* (SPEC. ISS), 644–647.

(74) Kanungo, P. Das; Schmid, H.; Björk, M. T.; Gignac, L. M.; Breslin, C.; Bruley, J.; Bessire, C. D.; Riel, H. *Nanotechnology* **2013**, *24* (22).

(75) Borg, M.; Schmid, H.; Moselund, K. E.; Cutaia, D.; Riel, H. *J. Appl. Phys.* **2015**, *117* (14).

(76) Green, M. A.; Hishikawa, Y.; Dunlop, E. D.; Levi, D. H.; Hohl-Ebinger, J.; Ho-Baillie, A. W. Y. *Prog. Photovoltaics Res. Appl.* **2018**, *26* (1), 3–12.

(77) Anttu, N.; Lehmann, S.; Storm, K.; Dick, K. A.; Samuelson, L.; Wu, P. M.; Pistol, M.-E. *Nano Lett.* **2014**, *14*, 5650–5655.

(78) Wallentin, J.; Anttu, N.; Asoli, D.; Huffman, M.; Aberg, I.; Magnusson, M. H.; Siefer, G.; Fuss-Kailuweit, P.; Dimroth, F.; Witzigmann, B.; Xu, H. Q.; Samuelson, L.; Deppert, K.; Borgström, M. T. *Science (80-.).* **2013**, *339* (6123), 1057–1060.

(79) Heurlin, M.; Magnusson, M. H.; Lindgren, D.; Ek, M.; Wallenberg, L. R.; Deppert, K.; Samuelson, L. *Nature* **2012**, *492* (7427), 90–94.

(80) Aberg, I.; Vescovi, G.; Asoli, D.; Naseem, U.; Gilboy, J. P.; Sundvall, C.; Dahlgren, A.; Svensson, K. E.; Anttu, N.; Bjork, M. T.; Samuelson, L. *IEEE J. Photovoltaics* **2015**, *6* (1), 185–190.

(81) Ito, T. *Japanese J. Appl. Physics, Part 2 Lett.* **1998**, *37* (10 SUPPL. B), 8–12.

(82) Williams, D. B.; Carter, C. B. *The Transmission Electron Microscope*; Springer, 2009.

(83) Shtrikman, H.; Popovitz-Biro, R.; Kretinin, A.; Houben, L.; Heiblum, M.; Bukala, M.; Galicka, M.; Buczko, R.; Kacman, P. *Nano Lett.* **2009**, *9* (4), 1506–1510.

(84) Joyce, H. J.; Wong-Leung, J.; Gao, Q.; Hoe Tan, H.; Jagadish, C. *Nano Lett.* **2010**, *10* (3), 908–915.

(85) Husanu, E.; Ercolani, D.; Gemmi, M.; Sorba, L. *Nanotechnology* **2014**, *25* (20).

(86) Kelrich, A.; Dubrovskii, V. G.; Calahorra, Y.; Cohen, S.; Ritter, D. *Nanotechnology* **2015**, *26* (8).

(87) Lehmann, S.; Jacobsson, D.; Dick, K. A. *Nanotechnology* **2015**, *26* (30), 301001.

(88) Pennycook, S. J.; Jesson, D. E. *Ultramicroscopy* **1991**, *37* (1–4), 14–38.

(89) Hinds, W. C. In *Aerosol Measurement: Principles, Techniques, and Applications: Third Edition*; 2011; pp 31–40.

(90) Givargizov, E. I. *J. Cryst. Growth* **1975**, *31* (C), 20–30.

(91) Dubrovskii, V. G.; Sibirev, N. V.; Cirlin, G. E.; Soshnikov, I. P.; Chen, W. H.; Larde, R.; Cadel, E.; Pareige, P.; Xu, T.; Grandidier, B.; Nys, J. P.; Stievenard, D.; Moewe, M.; Chuang, L. C.; Chang-Hasnain, C. *Phys. Rev. B - Condens. Matter Mater. Phys.* **2009**, *79* (20), 1–7.

(92) Johansson, J.; Dick, K. A.; Caroff, P.; Messing, M. E.; Bolinsson, J.; Deppert, K.; Samuelson, L. *J. Phys. Chem. C* **2010**, *114* (9), 3837–3842.

(93) Dayeh, S. A.; Picraux, S. T. *Nano Lett.* **2010**, *10* (10), 4032–4039.

(94) Buffat, P.; Borel, J. P. *Phys. Rev. A* **1976**, *13* (6), 2287–2298.

(95) Clouet, E. *ASM Handb.* **2009**, *22A*, 203–219.

(96) Sibirev, N. V.; Timofeeva, M. A.; Bol'shakov, A. D.; Nazarenko, M. V.; Dubrovskii, V. G. *Phys. Solid State* **2010**, *52* (7), 1531–1538.

(97) Kulkarni, P.; Willeke, K.; A. Baron, P. *Aerosol Measurement: Principles, Techniques, and Applications*; 2001.

(98) Tabrizi, N. S.; Ullmann, M.; Vons, V. A.; Lafont, U.; Schmidt-Ott, A. *J. Nanoparticle Res.* **2009**, *11* (2), 315–332.

(99) Schwyn, S.; Garwin, E.; Schmidt-Ott, A. *J. Aerosol Sci.* **1988**, *19* (5), 639–642.

(100) Helsper, C.; Mölter, W.; Löffler, F.; Wadenpohl, C.; Kaufmann, S.; Wenninger, G. *Atmos. Environ. Part A, Gen. Top.* **1993**, *27* (8), 1271–1275.

(101) Byeon, J. H.; Park, J. H.; Hwang, J. *J. Aerosol Sci.* **2008**, *39* (10), 888–896.

(102) Kala, S.; Theissmann, R.; Rouenhoff, M.; Kruis, F. E. *Nanotechnology* **2016**, *27* (12), 125604.

(103) Muntean, A.; Wagner, M.; Meyer, J.; Seipenbusch, M. *J. Nanoparticle Res.* **2016**, *18* (229), 9.

(104) Wagner, M.; Kohut, A.; Geretovszky, Z.; Seipenbusch, M.; Galbács, G. *J. Aerosol Sci.* **2016**, *93*, 16–20.

(105) Messing, M. E.; Svensson, C. R.; Pagels, J.; Meuller, B. O.; Deppert, K.; Rissler, J. *Nanotoxicology* **2013**, *7* (6), 1052–1063.

(106) Messing, M. E.; Westerström, R.; Meuller, B. O.; Blomberg, S.; Gustafson, J.; Andersen, J. N.; Lundgren, E.; Rijn, R. Van; Balmes, O.; Bluhm, H.; Deppert, K. *J. Phys. Chem. C* **2010**, *114* (20), 9257–9263.

(107) Meuller, B. O.; Messing, M. E.; Engberg, D. L. J.; Jansson, A. M.; Johansson, L. I. M.; Norlén, S. M.; Tureson, N.; Deppert, K. *Aerosol Sci. Technol.* **2012**, *46* (11), 1256–1270.

(108) Feng, J.; Hontañón, E.; Blanes, M.; Meyer, J.; Guo, X.; Santos, L.; Paltrinieri, L.; Ramlawi, N.; Smet, L. C. P. M. De; Nirschl, H.; Kruis, F. E.; Schmidt-Ott, A.; Biskos, G. *ACS Appl. Mater. Interfaces* **2016**, *8* (23), 14756–14765.

(109) Pai, D. Z. *J. Phys. D. Appl. Phys.* **2011**, *44* (17).

(110) Noh, S. R.; Lee, D.; Park, S. J.; Kim, D. S.; Choi, M. *Aerosol Sci. Technol.* **2017**, *51* (1), 116–122.

(111) Schmidt-ott, A.; Pfeiffer, T. V. WO 2013/115644 A1, 2013.

(112) Pfeiffer, T. V.; Feng, J.; Schmidt-Ott, a. *Adv. Powder Technol.* **2014**, *25* (1), 56–70.

(113) Barrigón, E.; Hultin, O.; Lindgren, D.; Yadegari, F.; Magnusson, M. H.; Samuelson, L.; Johansson, L. I. M.; Björk, M. T. *Nano Lett.* **2018**, acs.nanolett.7b04609.

(114) Hontañón, E.; Palomares, J. M.; Stein, M.; Guo, X.; Engeln, R.; Nirschl, H.; Kruis, F. E. *J. Nanoparticle Res.* **2013**, *15* (9), 1957.

(115) Kohut, A.; Ludvigsson, L.; Meuller, B. O.; Deppert, K.; Messing, M. E.; Galbács, G.; Geretovszky, Z. *Nanotechnology* **2017**, *28*.

(116) Friedlander, S. K. *Ann. N. Y. Acad. Sci.* **1983**, *404* (1), 354–364.

(117) Pratsinis, S. E. *Prog. energy Combust. Sci.* **1998**, *24* (97), 197–219.

(118) Ludvigsson, L.; Meuller, B. O.; Messing, M. E. *J. Phys. D. Appl. Phys.* **2015**, *48* (31), 314012.

(119) Feng, J.; Huang, L.; Ludvigsson, L.; Messing, M. E.; Maisser, A.; Biskos, G.; Schmidt-Ott, A. *J. Phys. Chem. C* **2016**, *120* (1), 621–630.

(120) Lehtinen, K. E. J.; Zachariah, M. R. *J. Aerosol Sci.* **2002**, *33* (2), 357–368.

(121) Willeke, K.; A. Baron, P. *Aerosol Measurement: Principles, Techniques, and Applications*; 2001.

(122) Weber, A. P.; Friedlander, S. K. *J. Aerosol Sci.* **1997**, *28* (97), S765–S766.

(123) Kuffel, E.; Zaengl, W. S.; Kuffel, J. *High Voltage Engineering - Fundamentals*; Newnes, Oxford, 2000.

(124) Palomares, J. M.; Kohut, A.; Galbács, G.; Engeln, R.; Geretovszky, Z. *J. Appl. Phys.* **2015**, *118* (23).

(125) Llewellyn, F.; Phil, M. A. *Br. J. Appl. Phys.* **1950**.

(126) Kohut, A.; Wagner, M.; Seipenbusch, M.; Geretovszky, Z.; Galbács, G. *J. Aerosol Sci.* **2018**, *119* (February), 51–61.

(127) Soldera, F.; Lasagni, A.; Mücklich, F.; Kaiser, T.; Hrastnik, K. *Comput. Mater. Sci.* **2005**, *32* (1), 123–139.

(128) Petr, R. A.; Burkes, T. R. *Appl. Phys. Lett.* **1980**, *36* (7), 536–537.

(129) Gray, E. W.; Pharney, J. R. *J. Appl. Phys.* **1974**, *45* (2), 667–671.

(130) Pfeiffer, T. V. Towards the Industrial Application of Spark Ablation for Nanostructured Functional Materials, Technische Universiteit Delft, 2014.

(131) Liu, B. Y. H.; Pui, D. Y. H. *J. Aerosol Sci.* **1974**, *5* (5), 465–472.

(132) Wiedensohler, A. *J. Aerosol Sci.* **1988**, *19* (3), 387–389.

(133) Wiedensohler, A.; Fissan, H. J. *Aerosol Sci. Technol.* **1991**, *14* (3), 358–364.

(134) Collins, D. R.; Cocker, D. R.; Flagan, R. C.; Seinfeld, J. H. *Aerosol Sci. Technol.* **2004**, *38* (8), 833–850.

(135) Knutson, E. O.; Whitby, K. T. *J. Aerosol Sci.* **1975**, *6* (6), 443–451.

(136) Wang, S. C.; Flagan, R. C. *Aerosol Sci. Technol.* **1990**, *13* (2), 230–240.

(137) Schmidt-Ott, A. *J. Aerosol Sci.* **1988**, *19* (5), 553–563.

(138) Nanda, K. K.; Maisels, A.; Kruis, F. E. *J. Phys. Chem. C* **2008**, *112* (35), 13488–13491.

(139) Askeland, D.; Pradeep, F.; Wright, W. *The Science and Engineering of Materials*, 6th ed.; Chapman and Hall: London, 2011.

(140) Yeh, H.-C.; Cheng, Y.-S. *Environ. Sci. Technol.* **1980**, *14* (6), 726–729.

(141) Nanda, K. K.; Maisels, A.; Kruis, F. E. *RSC Adv.* **2011**, *1* (4), 568–572.

(142) Karlsson, M. N. A.; Deppert, K.; Karlsson, L. S.; Magnusson, M. H.; Malm, J. O.; Srinivasan, N. S. *J. Nanoparticle Res.* **2005**, *7* (1), 43–49.

(143) Nanda, K. K.; Kruis, F. E.; Fissan, H. *Phys. Rev. Lett.* **2002**, *89* (25), 1–4.

(144) Nanda, K. K.; Kruis, F. E.; Fissan, H.; Acet, M. *J. Appl. Phys.* **2002**, *91* (3), 2315–2321.

(145) Davies, C. N. *Fundamentals of Aerosol Science*; D.T. Shaw, Ed.; JohnWiley and Sons: New York, 1978.

(146) Stull, D. *American Institute of Physics Handbook - Third Edition*; Gray, D. ., Ed.; McGraw Hill, New York, 1972.

(147) Deppert, K.; Schmidt, F.; Krinke, T.; Dixkens, J.; Fissan, H. *J. Aerosol Sci.* **1996**, *27*, 151-152.

(148) Dixkens, J.; Fissan, H. *Aerosol Sci. Technol.* **1999**, *30* (5), 438–453.

(149) Magnusson, M. H.; Deppert, K.; Malm, J.-O.; Bovin, J.-O.; Samuelson, L. *J. Nanoparticle Res.* **1999**, *1*, 243–251.

(150) Watters, R. L.; DeVoe, J. R.; Shen, F. H.; Small, J. A.; Marinenko, R. B. *Anal. Chem.* **1989**, *61* (17), 1826–1833.

(151) Roth, C.; Ferron, G. A.; Karg, E.; Lentner, B.; Schumann, G.; Takenaka, S.; Heyder, J. *Aerosol Sci. Technol.* **2004**, *38* (3), 228–235.

(152) Kala, S.; Theissmann, R.; Kruis, F. E. *J. Nanoparticle Res.* **2013**, *15* (9).

(153) Ludvigsson, L. Physical characterization of engineered aerosol particles, 2017.

(154) Vons, V. A.; Smet, L. C. P. M.; Munao, D.; Evirgen, A.; Kelder, E. M.; Schmidt-Ott, A. *J. Nanoparticle Res.* **2011**, *13* (10), 4867–4879.

(155) Kim, J.-T.; Chang, J.-S. *J. Electrostat.* **2005**, *63* (6–10), 911–916.

(156) Nilsson, P. T.; Eriksson, A. C.; Ludvigsson, L.; Messing, M. E.; Nordin, E. Z.; Gudmundsson, A.; Meuller, B. O.; Deppert, K.; Fortner, E. C.; Onasch, T. B.; Pagels, J. H. *Nano Res.* **2015**, *8* (12), 3780–3795.

(157) Seipenbusch, M.; Weber, A. P.; Schiel, A.; Kasper, G. *J. Aerosol Sci.* **2003**, *34* (12), 1699–1709.

(158) Luidold, S.; Antrekowitsch, H. *Jom* **2007**, *59* (10), 58–62.

(159) Luidold, S.; Antrekowitsch, H. *Jom* **2007**, *59* (6), 20–26.

(160) Atkins, P. W.; Jones, L. *Chemical principles : the quest for insight.*; New York : W.H. Freeman, cop. 2008, 2008.

(161) Evans, D. E.; Harrison, R. M.; Ayres, J. G. *Aerosol Sci. Technol.* **2003**, *37* (12), 975–987.

(162) Tabrizi, N. S.; Xu, Q.; Van Der Pers, N. M.; Schmidt-Ott, A. *J. Nanoparticle Res.* **2010**, *12* (1), 247–259.

(163) Weber, A. P.; Friedlander, S. K. *J. Aerosol Sci.* **1997**, *28* (2), 179–192.

(164) Wang, K. W.; Chung, S. R.; Perng, T. P. *J. Alloys Compd.* **2006**, *422* (1–2), 223–226.

(165) Givargizov, E. I. *Highly anisotropic crystals*; Materials science of minerals and rocks; Springer Netherlands, 1986.

(166) Kolasinski, K. W. *Curr. Opin. Solid State Mater. Sci.* **2006**, *10* (3–4), 182–191.

(167) Dick, K. A. *Prog. Cryst. Growth Charact. Mater.* **2008**, *54* (3–4), 138–173.

(168) Krogstrup, P.; Jørgensen, H. I.; Johnson, E.; Madsen, M. H.; Sørensen, C. B.; Morral, A. F. I.; Aagesen, M.; Nygård, J.; Glas, F. *J. Phys. D. Appl. Phys.* **2013**, *46* (31), 313001.

(169) Redwing, J. M.; Miao, X.; Li, X. *Vapor-Liquid-Solid Growth of Semiconductor Nanowires*, Second Edi.; Elsevier B.V., 2014; Vol. 3.

(170) Lensch-Falk, J.; Hemesath, E.; Perea, D. E.; Lauhon, L. J. *J. Mater. Chem.* **2009**, *19* (7), 849–857.

(171) Johansson, J.; Svensson, C. P. T.; Mårtensson, T.; Samuelson, L.; Seifert, W. *J. Phys. Chem. B* **2005**, *109* (28), 13567–13571.

(172) Wacaser, B. A.; Dick, K. A.; Johansson, J.; Borgström, M. T.; Deppert, K.; Samuelson, L. *Adv. Mater.* **2009**, *21* (2), 153–165.

(173) De Jong, E.; Lapierre, R. R.; Wen, J. Z. *Nanotechnology* **2010**, *21* (4).

(174) Glas, F.; Ramdani, M. R.; Patriarche, G.; Harmand, J. C. *Phys. Rev. B - Condens. Matter Mater. Phys.* **2013**, *88* (19), 1–14.

(175) Dubrovskii, V. G. *Appl. Phys. Lett.* **2014**, *104* (5), 053110.

(176) Dubrovskii, V. G. *Nucleation Theory and Growth of Nanostructures*; Berlin, Heidelberg : Springer Berlin Heidelberg : Imprint: Springer, 2014., 2014.

(177) Stringfellow, G. B. *Organometallic Vapor-Phase Epitaxy: Theory and Practice - 2nd edition*; New York, NY : Academic Press, 1999.

(178) Pohl, U. W. *Epitaxy of Semiconductors: Introduction to Physical Principles*; Berlin ; Heidelberg : Springer, cop. 2013, 2013.

(179) Larsen, C. A.; Li, S. H.; Buchan, N. I.; Stringfellow, G. B.; Brown, D. W. *J. Cryst. Growth* **1990**, *102* (1–2), 126–136.

(180) Larsen, C. A.; Buchan, N. I.; Li, S. H.; Stringfellow, G. B. *J. Cryst. Growth* **1990**, *102* (1–2), 117–125.

(181) Deppert, K.; Bovin, J.-O.; Malm, J.-O.; Samuelson, L. *J. Cryst. Growth* **1996**, *169* (1), 13–19.

(182) Buchan, N. I.; Larsen, C. A.; Stringfellow, G. B. *J. Cryst. Growth* **1988**, *92* (3–4), 605–615.

(183) DenBaars, S. P.; Maa, B. Y.; Dapkus, P. D.; Danner, A. D.; Lee, H. C. *J. Cryst. Growth* **1986**, *77* (1–3), 188–193.

(184) Verheijen, M. A.; Immink, G.; De Smet, T.; Borgström, M. T.; Bakkers, E. P. A. M. *J. Am. Chem. Soc.* **2006**, *128* (4), 1353–1359.

(185) Kodambaka, S.; Tersoff, J.; Reuter, M. C.; Ross, F. M. *Phys. Rev. Lett.* **2006**, *96* (9), 1–4.

(186) Borgström, M. T.; Immink, G.; Ketelaars, B.; Algra, R.; Bakkers, E. P. A. M. *Nat. Nanotechnol.* **2007**, *2* (9), 541–544.

(187) Wagner, R. S.; Ellis, W. C. *Appl. Phys. Lett.* **1964**, *4* (5), 89–90.

(188) Schubert, L.; Werner, P.; Zakharov, N. D.; Gerth, G.; Kolb, F. M.; Long, L.; Gösele, U.; Tan, T. Y. *Appl. Phys. Lett.* **2004**, *84* (24), 4968–4970.

(189) Jensen, L. E.; Björk, M. T.; Jeppesen, S.; Persson, A. I.; Ohlsson, B. J.; Samuelson, L. *Nano Lett.* **2004**, *4* (10), 1961–1964.

(190) Kolasinski, K. W. 2012; p 562.

(191) Smith, D. L. *Thin-film deposition : principles and practice.*; New York : McGraw-Hill, cop. 1995, 1995.

(192) Seifert, W.; Borgström, M.; Deppert, K.; Dick, K. A.; Johansson, J.; Larsson, M. W.; Mårtensson, T.; Sköld, N.; Svensson, C. P. T.; Wacaser, B. A.; Wallenberg, L. R.; Samuelson, L. *J. Cryst. Growth* **2004**, *272* (1–4 SPEC. ISS.), 211–220.

(193) Johansson, J. *Nat. Nanotechnol.* **2007**, *2* (9), 534–535.

(194) Borg, B. M.; Johansson, J.; Storm, K.; Deppert, K. *J. Cryst. Growth* **2013**, *366*, 15–19.

(195) Golovin, A. A.; Davis, S. H.; Voorhees, P. W. *J. Appl. Phys.* **2008**, *104* (7).

(196) Roper, S. M.; Davis, S. H.; Norris, S. A.; Golovin, A. A.; Voorhees, P. W.; Weiss, M. *J. Appl. Phys.* **2007**, *102* (3).

(197) Persson, A. I.; Larsson, M. W.; Stenström, S.; Ohlsson, B. J.; Samuelson, L.; Wallenberg, L. R. *Nat. Mater.* **2004**, *3* (10), 677–681.

(198) Cui, H.; Lü, Y. Y.; Yang, G. W.; Chen, Y. M.; Wang, C. X. *Nano Lett.* **2015**, *15* (5), 3640–3645.

(199) Hofmann, S.; Sharma, R.; Wirth, C. T.; Cervantes-Sodi, F.; Ducati, C.; Kasama, T.; Dunin-Borkowski, R. E.; Drucker, J.; Bennett, P.; Robertson, J. *Nat. Mater.* **2008**, *7* (5), 372–375.

(200) Wen, C. Y.; Reuter, M. C.; Bruley, J.; Tersoff, J.; Kodambaka, S.; Stach, E. A.; Ross, F. M. *Science (80-.).* **2009**, *326* (November), 1247–1250.

(201) Wen, C. Y.; Tersoff, J.; Reuter, M. C.; Stach, E. A.; Ross, F. M. *Phys. Rev. Lett.* **2010**, *105* (19), 1–4.

(202) Chou, Y.-C.; Panciera, F.; Reuter, M. C.; Stach, E. A.; Ross, F. M. *Chem. Commun.* **2016**, *52* (33), 5686–5689.

(203) Jacobsson, D.; Panciera, F.; Tersoff, J.; Reuter, M. C.; Lehmann, S.; Hofmann, S.; Dick, K. A.; Ross, F. M. *Nature* **2016**, *531* (7594), 317–322.

(204) Sear, R. P. *J. Phys. Condens. Matter* **2007**, *19* (3), 033101.

(205) Wen, C. Y.; Tersoff, J.; Hillerich, K.; Reuter, M. C.; Park, J. H.; Kodambaka, S.; Stach, E. A.; Ross, F. M. *Phys. Rev. Lett.* **2011**, *107* (2), 1–4.

(206) Oh, S. H.; Chisholm, M. F.; Kauffmann, Y.; Kaplan, W. D.; Luo, W.; Rühle, M.; Scheu, C. *Science (80-.).* **2010**, *330* (October), 1757–1762.

(207) Gamalski, A. D.; Ducati, C.; Hofmann, S. *J. Phys. Chem. C* **2011**, *115* (11), 4413–4417.

(208) Manasevit, H. M.; Simpson, W. I. *J. Electrochem. Soc.* **1969**, *116* (12), 1725–1732.

(209) Kuech, T. F.; Veuhoff, E. *J. Cryst. Growth* **1984**, *68* (1), 148–156.

(210) Messing, M. E.; Hillerich, K.; Bolinsson, J.; Storm, K.; Johansson, J.; Dick, K. A.; Deppert, K. *Nano Res.* **2010**, *3* (7), 506–519.

(211) Zakharov, A. A.; Mårsell, E.; Hilner, E.; Timm, R.; Andersen, J. N.; Lundgren, E.; Mikkelsen, A. *ACS Nano* **2015**, *9* (5), 5422–5431.

(212) Otnes, G.; Heurlin, M.; Graczyk, M.; Wallentin, J.; Jacobsson, D.; Berg, A.; Maximov, I.; Borgström, M. T. *Nano Res.* **2016**, *9* (10), 1–10.

(213) Whiticar, A. M.; Mårtensson, E. K.; Nygård, J.; Dick, K. A.; Bolinsson, J. *Nanotechnology* **2017**, *28* (111), 205702 (12pp).

(214) Curiotto, S.; Leroy, F.; Cheynis, F.; Müller, P. *Sci. Rep.* **2017**, *7* (1), 1–11.

(215) Heurlin, M.; Anttu, N.; Camus, C.; Samuelson, L.; Borgström, M. T. *Nano Lett.* **2015**, *15* (5), 3597–3602.

(216) Nattermann, L.; Maßmeyer, O.; Sterzer, E.; Derpmann, V.; Chung, H. Y.; Stolz, W.; Volz, K. *Sci. Rep.* **2018**, *8* (1), 1–7.

(217) Deppert, K.; Samuelson, L. *Appl. Phys. Lett.* **1996**, *68* (10), 1409–1411.

(218) Morales, A.M and Lieber, C. M. *Science* **1998**, *279* (5348), 208–211.

(219) Duan, X.; Lieber, C. M. *Adv. Mater.* **2000**, *12* (4), 298–302.

(220) Gudiksen, M. S.; Wang, J.; Lieber, C. M. *J. Phys. Chem. B* **2001**, *105* (19), 4062–4064.

(221) Heurlin, M. Aerotaxy - A Gas-Phase Nanowire Growth Technique, 2014.

(222) Yang, F.; Messing, M. E.; Mergenthaler, K.; Ghasemi, M.; Johansson, J.; Wallenberg, L. R.; Pistol, M.-E.; Deppert, K.; Samuelson, L.; Magnusson, M. H. *J. Cryst. Growth* **2015**, *414*, 181–186.

(223) Metaferia, W.; Persson, A. R.; Mergenthaler, K.; Yang, F.; Zhang, W.; Yartsev, A.; Wallenberg, R.; Pistol, M.-E.; Deppert, K.; Samuelson, L.; Magnusson, M. H. *Nano Lett.* **2016**, acs.nanolett.6b02367.

(224) Ghasemi, M.; Johansson, J. *J. Phys. D. Appl. Phys.* **2017**, *50* (134002), 8.

(225) Heun, S.; Radha, B.; Ercolani, D.; Kulkarni, G. U.; Rossi, F.; Grillo, V.; Salviati, G.; Beltram, F.; Sorba, L. *Small* **2010**, *6* (17), 1935–1941.

(226) Metaferia, W.; Sivakumar, S.; Persson, A. R.; Geijselaers, I.; Wallenberg, L. R.; Deppert, K.; Samuelson, L.; Magnusson, M. H. *Nanotechnology* **2018**, *29* (28).

(227) Borgström, M. T.; Magnusson, M. H.; DImroth, F.; Siefer, G.; Höhn, O.; Riel, H.; Schmid, H.; Wirths, S.; Björk, M.; Åberg, I.; Peijnenburg, W.; Vijver, M.; Tchernycheva, M.; Piazza, V.; Samuelson, L. *IEEE J. Photovoltaics* **2018**, *8* (3), 733–740.

(228) Morningstar May 9th 2018 https://www.morningstar.com (accessed May 9, 2018).

(229) Mårtensson, E. K.; Whiticar, A. M.; De La Mata, M.; Zamani, R. R.; Johansson, J.; Nygård, J.; Dick, K. A.; Bolinsson, J. *Under Rev.* **2018**, *x* (x), x.
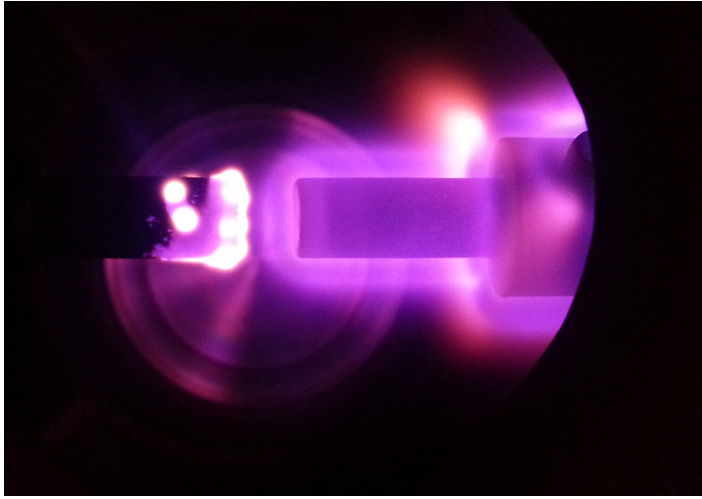
Faculty of Engineering
Department of Physics
Division of Solid State Physics

LUND
UNIVERSITY

9 789177 538424